

TRANSIENT BEHAVIOR OF LIQUID JETS
INJECTED NORMAL TO A HIGH VELOCITY GAS STREAM

by

David Matthew Less

Dissertation submitted to the Faculty of the
Virginia Polytechnic Institute and State University
in partial fulfillment of the requirements for the degree of

DOCTOR OF PHILOSOPHY

in

Aerospace Engineering

APPROVED:

J. A. Schetz, Chairman

C. H. Lewis

A. K. Jakubowski

M. Williams

J. F. Marchman

February, 1985
Blacksburg, Virginia

TRANSIENT BEHAVIOR OF LIQUID JETS
INJECTED NORMAL TO A HIGH VELOCITY GAS STREAM

by

David Matthew Less

(ABSTRACT)

The transient effects of the breakup and atomization of liquid jets in a crossflow on the size of droplets within the spray plume was experimentally determined. Water and water/methanol mixtures were injected normal to a high velocity air stream at Mach numbers of 0.48 and 3.0 with ambient stagnation temperature and respective stagnation pressures of 1.4 and 4.3 atm. The liquids were injected at liquid-to-gas momentum flux ratios ranging from 4 to 12. Droplet size distributions were obtained using a Fraunhofer diffraction technique at sampling rates of up to 9 kHz. Liquid mass flow rates were inferred from measurements of the extinction of a laser beam traversing the plume. The droplet sizes were found to fluctuate with frequencies of the order of 1 to 10 kHz. The fluctuations were characterized by a sudden and relatively brief increase in the mean diameter of the droplets caused by the passage of fractured clumps through the spray plume. Also evident in the droplet size distributions was the very small size of the droplets that had been sheared off the windward surfaces of the jet. The jet fracture

frequency was related to the frequency of waves propagating along the initial jet column. The column waves are postulated to have been caused by jet perturbations created by vortices in the air flow around the jet column.

TABLE OF CONTENTS

	Page
LIST OF FIGURES.....	vi
LIST OF TABLES.....	ix
NOMENCLATURE.....	xi
INTRODUCTION.....	1
II. DROPLET SIZE DISTRIBUTION TECHNIQUE.....	15
2.1 Theory of Fraunhofer Diffraction.....	15
2.2 Droplet Size Distribution Calculations.....	18
2.3 Droplet Sizing Errors.....	21
III. EXPERIMENTAL APPARATUS AND PROCEDURES.....	25
3.1 Test Facility.....	25
3.2 Injection System.....	26
3.3 Droplet Sizing System.....	27
3.3.1 Optical Arrangement.....	27
3.3.2 Electronics.....	28
3.3.3 Software.....	30
3.3.4 System Accuracy.....	31
3.4 Frequency Measurements.....	33
3.5 Photographic Setup.....	33
3.6 Experimental Procedures.....	34
IV. RESULTS.....	36
4.1 Description of Measurements.....	36
4.2 Injection into a Subsonic Air Stream.....	40
4.2.1 Droplet Sizes.....	41
4.2.2 Extinction Measurements.....	44
4.2.3 Photographic Results.....	45
4.3 Injection into a Supersonic Air Stream.....	47
4.3.1 Water/Methanol.....	47
4.3.2 Water, High \bar{q}	52
4.3.2.1 Droplet Sizes.....	52
4.3.2.2 Extinction Measurements.....	57
4.3.2.3 Photographic Results.....	60
4.3.2.4 CCD Penetration Results.....	61
4.3.3 Water, Low \bar{q}	63
4.3.3.1 Droplet Sizes.....	63
4.3.3.2 Extinction Measurements.....	66
4.3.3.3 Photographic Results.....	67

V. DISCUSSION.....	69
5.1 Physical Interpretations of the Observed Fluctuations in the Droplet Sizes.....	69
5.2 Frequency of the Observed Fluctuations in the Droplet Sizes.....	72
5.2.1 Supersonic Crossflow.....	72
5.2.2 Subsonic Crossflow.....	74
5.2.3 Jet Whipping.....	76
5.3 Development of the Jet Model.....	81
5.4 Droplet Size Distributions.....	97
5.4.1 Subsonic Crossflow.....	97
5.4.2 Supersonic Crossflow.....	100
5.5 Plume Dimensions.....	102
5.6 Other Time-Dependent Phenomena Within Plume.....	106
CONCLUSIONS.....	113
REFERENCES.....	117
APPENDIX.....	122
FIGURES.....	126
TABLES.....	178

LIST OF FIGURES

	Page
1 Schematic of liquid injection into supersonic crossflow...	126
2 Stop-action view of liquid jet in supersonic flow.....	127
3 High-speed movie of liquid jet in supersonic flow.....	128
4 Stop-action view of liquid jet in subsonic flow.....	129
5 Example of regime 1 jet.....	130
6 Schematic of air injection into an air crossflow.....	131
7 Schematic of flat plate model.....	132
8 Schematic of optical arrangement.....	133
9 Calibration reticle size distribution.....	134
10 Droplet size distributions for water jet in subsonic flow.	135
11 Droplet size distributions for various x/d	136
12 Distributions for various exposure times at $x/d=100$, $z/d=20$	137
13 Distributions for various exposure times at $x/d=50$, $z/d=10$	138
14 Variations in distribution at $x/d=100$, $z/d=20$	139
15 Plot of SMD for water jet in subsonic flow.....	140
16 Examples of extinction time traces.....	141
17 Frequency spectrum at $x/d=20$, $z/d=5$	142
18 Frequency spectrum at $x/d=100$, $z/d=25$	143
19 Frequency spectrum at $x/d=100$, $z/d=5$	144
20 Cross section of water jet at $x/d=100$	145
21 Schematic of cross section of jet.....	146
22 Breakup of water jet in subsonic flow.....	147
23 Locations of measurements within jet plume.....	148

24	Distributions at 25 msec exposure time.....	149
25	Distributions at 5 msec exposure time.....	150
26	Distributions at 2.5 msec exposure time.....	151
27	Distributions at 0.65 msec exposure time.....	152
28	Distributions at 0.225 msec exposure time.....	153
29	Distributions at various y/d	154
30	Distributions at various x/d for high \bar{q} jet.....	155
31	Distributions at various x/d for low \bar{q} jet.....	156
32	Stop-action view of a low \bar{q} jet.....	157
33	Examples of extinction data for water/methanol jet.....	158
34	Plot of SMD for high \bar{q} water jet on supersonic flow.....	159
35	Distributions at various x/d	160
36	Distributions at various z/d	161
37	Various distributions at 0.11 msec exposure time.....	162
38	Example of extinction data.....	163
39	Frequency spectrums close to injector.....	164
40	Frequency spectrums at various z/d	165
41	Schematic of cross section of jet.....	166
42	Cross section of water jet at $x/d=100$	167
43	Example of CCD penetration result.....	168
44	Plot of SMD for low \bar{q} water jet in supersonic flow.....	169
45	Variations in distributions at $x/d=20$, $z/d=6$	170
46	Distributions at various x/d	171
47	Distributions at various z/d	172

48	Examples of frequency spectrums.....	173
49	Cross section of water jet at $x/d=200$	174
50	Jet column wave propagation speed.....	175
51	Atomization of water jet in subsonic crossflow.....	176
52	Mass sampling survey of water jet.....	177

LIST OF TABLES

	Page
1 Time histories of SMD for water jet in subsonic flow.....	178
2 Frequency of the extinction pattern.....	179
3 Vertical locations of maximum transients.....	180
4 Plume dimensions of water jet in subsonic flow.....	181
5 Mean and standard deviation of SMD for various exposure times.....	182
6 Time histories of SMD for water/alcohol jet in supersonic flow.....	183
7 Mean and standard deviation of SMD for various z/d	184
8 Mean and standard deviation of SMD for various x/d for high \bar{q} water/alcohol jet.....	185
9 Mean and standard deviation of SMD for various x/d for low \bar{q} water/alcohol jet.....	186
10 Time histories of SMD for high \bar{q} water jet in supersonic flow.....	187
11 Variations in the populations of the three major size groups.....	189
12 Vertical locations of highest frequency transients.....	191
13 Vertical locations of maximum fluctuations in SMD.....	192
14 Mean transmission values.....	193
15 Plume dimensions of high \bar{q} water jet in supersonic flow...	194
16 Time histories of SMD for low \bar{q} water jet in supersonic flow.....	195
17 Maximum and minimum SMD at various x/d	196
18 Variations in the population of the three major size groups.....	197

19	Mean transmission values.....	198
20	Vertical locations of highest frequency transients.....	199
21	Vertical locations of maximum variations in SMD.....	200
22	Plume dimensions of low q water jet in supersonic flow....	201
23	Frequencies of jet column waves.....	202
24	Initial wavelengths of jet column waves.....	203
25	Fracture frequencies.....	204
26	SMD for various jets and free stream Mach numbers.....	205
27	Plume dimensions for water jets.....	206

NOMENCLATURE

a	area
c	constant
C_d	discharge coefficient for an injection
d,D	diameter
E	energy
f	focal length
FFT	Fast Fourier Transform
h,H	penetration height
HC	height of widest part of jet
I	intensity
J	matrix relating \vec{L} and \vec{V}
k	wave number, $2\pi/\lambda$
L	light energy falling within a ring
LL	height of liquid layer
LW	width of liquid layer
M	Mach number
n	Rosin-Rammler parameter related to spread of distribution
N	frequency
P	period of fluctuations
P_o	stagnation pressure
\bar{q}	momentum flux ratio, $\rho_j V_j^2 / \rho_g V_g^2$
r	radial distance
Re	Reynolds number, $\rho V d / \mu$

S	period of clump passage
SMD	Sauter mean diameter or $D_{3,2}$
T_o	stagnation temperature
u, v	spatial frequency
$U(r)$	light energy falling at radius r
U, V	velocity
V	volume fraction
w, W	width
WC	width of jet joining plume and liquid layer
We	Weber number, $\rho V^2 d / \sigma$
\bar{x}	Rosin-Rammler mean diameter
x, y, z	coordinates
$x/d, y/d, z/d$	plume coordinates non-dimensionalized by injector diameter
λ	wavelength
μ	viscosity
ρ	density
σ	surface tension

subscripts

F	fracture
g	gas
j	initial jet conditions
l	liquid
o	orifice
W	wave
∞	free stream
1	conditions immediately upstream of the liquid jet column

INTRODUCTION

The injection of a liquid jet into a high velocity gas crossflow occurs in many diverse engineering situations. The transverse injection of liquid fuels into the combustion chamber of ramjets and scramjets, cooling sprays for turbine blades, thrust vector control for rockets and the injection of fuel in afterburners all involve liquid jets in a gas stream. Additionally, the injection of liquids from projectile surfaces has been considered for several different intentions. Injection of a liquid fuel into the air stream surrounding a vehicle has been contemplated for increased control, maneuverability and drag reduction. Local cooling by means of a spray has been suggested to reduce the black-out period associated when an ionized layer develops around the communications antennae on re-entry vehicles. These are but a few of many examples.

In all of these situations, the behavior of the liquid jet is important. The atomization of the liquid into fine droplets and the transient behavior of the jet plume can greatly influence such processes as combustion and cooling. In most applications, the penetration and the lateral spread of the jet are of prime engineering concern. Due to the recent developments of hybrid fuels whose viscosity and surface tension can cover a wide range of values, the effect that these liquid properties exert on jet break up and atomization also needs to be investigated.

The earliest investigations of liquid injections into a gas medium concerned the stability of the initial jet column. A cross flow was not usually considered in these studies. Lord Rayleigh (1, 2) modeled the jet flow by balancing the surface tension forces with the pressures on a perturbed column of liquid. He determined that the perturbations would tend to produce bead-like swellings and contractions on the liquid surface. If the wavelength of the disturbance was greater than the circumference of the column then the disturbance would grow in amplitude and eventually would cause the jet to break up into drops.

Weber (3) extended Lord Rayleigh's work to include the effects of viscosity. He postulated that at higher jet velocities, Kelvin-Helmholtz instabilities would create symmetric and sinuous disturbances. Kelvin-Helmholtz instabilities occur at the interface between two fluids when there exists a relative velocity between the two bodies of liquid parallel to the interface. Tomotika (4) studied the injection of a viscous jet into another viscous fluid.

Analyzing the experimental work of previous investigators, Castleman (5, 6) noted the importance of wave-like disturbances on the jet. The disturbances when amplified would shed ligaments which in turn would be quickly atomized into drops. Dunn and Caseman (7) investigated liquid injection into supersonic flows. Their experiments revealed large symmetric waves and "breaks" in the jet. In a partly theoretical study, York, Stubbs and Tek (8) demonstrated that wave-like disturbances and instabilities at the interface of a

liquid sheet flowing parallel to a surrounding fluid were the major factors in the break up of the sheet into drops. Miesse (9) compiled a summary and correlation of experimental data of the disintegration of a liquid injected into a quiescent medium.

Yuen (10) and Nayfeh (11) extended the previous linear analyses by investigating the non-linear stability of a liquid jet. Nayfeh theoretically predicted that below a certain wave number jet disturbances would grow in time. Disturbances with larger wave numbers would be stable, but their frequency would be amplitude-dependent.

While these studies of a liquid injected into a quiescent medium were being conducted, a number of studies were being performed analyzing wind-generated waves on a liquid surface. Eventually the results of both types of studies would be combined for the study of a jet in a crossflow. Lord Kelvin (12) examined the generation of waves over a frictionless fluid. Jeffreys (13) extended Lord Kelvin's work by considering flow separation at the crest of the waves. His findings were later discredited by Lighthill (14, 15) who showed that in wave-fixed coordinates, the gas velocity at the surface is opposite to that of the free stream. The separation would then consequently occur on the windward face of the wave.

The stability of a liquid surface subjected to an acceleration normal to its planar interface was extensively discussed by Lamb (16) and by Taylor (18). The instability for such an interface is a special case of Rayleigh-Taylor instabilities which Taylor proved in

Ref. 17 could also occur at the interface between two fluids of different densities. Lewis (19) and Bellman and Pennington (20) also studied the stability of liquid surfaces normally accelerated. Considering both Rayleigh-Taylor and Kelvin-Helmholtz instabilities, Chang and Russell (66) performed a linear analysis of a liquid layer adjacent to subsonic and supersonic gas streams. Nayfeh and Saric (21) studied a similar problem using a non-linear analysis.

Chelko (22) and Foster and Ingebo (23) were among the first to examine a liquid injected into a crossflow. Foster and Ingebo used a microphotographic survey to measure the drop size distributions within the jet. They developed equations relating the mean droplet diameter (non-dimensionalized by the injector diameter) to the product of the Weber and Reynolds number. Weiss and Worsham (24) investigated the atomization of molten Acrawax-c jets in a high velocity air stream. They studied the effects of air density, relative velocity, mass flow rate and injector diameter on the droplet sizes and concluded that the relative velocity between the gas and the liquid exerted the most influence. They also noted that the droplets were almost uniformly spherical in shape. Bitron (25) measured droplet sizes using an impact collection method for a dibutyl phthalate jet.

Adelberg (26) theoretically estimated droplet sizes by a model which relied on ligament formation and shedding as the principal means of droplet formation. His analysis also included gravity-like waves acting on the jet surface arising from the downstream acceleration

created by the aerodynamic drag of the jet body. Some of Adelberg's assumptions have not been widely accepted.

Transverse jets in a low velocity crossflow were examined by Clark (27). His model involved the break up of a flattened liquid stream with energy input from shear. He also considered droplets and ligaments being torn from the edges. Based on simple Newtonian flow concepts Forde, Medler and Szpiro (28) constructed a model that predicted the path of the jet. The penetration heights predicted by their model were found to agree with a series of wind tunnel experiments they performed with a Mach 3 free stream. A range of injection angles, injector diameters and injectant total pressures were tested.

For water jets in a Mach 2.8 air stream Kolpin, Horn and Reichenbach (29) correlated the penetration height with the injection pressure ratio. Reichenbach and Horn (30) investigated the effects of vapor pressure, liquid viscosity and surface tension on jets in supersonic crossflows. They determined that as long as the vapor flashing time was greater than the aerodynamic breakup time the vapor pressure had little influence on the penetration. For the range of viscosities and surface tensions tested neither was seen to affect the penetration heights. Horn and Reichenbach (31) later determined that the lateral spreading and the penetration of the jet depended on the Mach number and upon the injection pressure ratio. Further penetration measurements for supersonic and hypersonic gas streams

were conducted by Catton, Hill and McRae (32) and by Edelman, Schmotelochs and Slutsky (33).

Sherman and Schetz (34) investigated the mechanism of liquid sheet and jet break up in a supersonic flow. Large amplitude waves were observed on the surface of the liquid. Gross fracture of the jet was attributed to be the mechanism by which the liquid jet was broken into droplets. Joshi and Schetz (35) examined different injector orifices. In their tests, water was injected into a Mach 3.0 air stream through circular and rectangular orifices at various injection pressure ratios. The penetration was found to depend on the pressure ratio and on the streamwise dimension of the orifice. For a given mass flow of liquid, a rectangular injector produced the highest penetration and the largest spread. Padye and Schetz (36) through a photographic survey correlated the non-dimensional penetration height (h/d_j) with the momentum flux ratio for water injected into a subsonic crossflow.

The previously mentioned reports generally measured penetration and droplet sizes through photographs. Shaikhutdinov and Klevanskii (37) measured the penetration by a temperature survey and compared the results obtained with those from a streak photographic method. The streak photographs yielded plume dimensions that were 25-30% smaller than those produced by the more reliable temperature survey. Direct mass sampling in the jet plume also has been only recently performed. Yang, Gu, Liu and Li (38) and Thomas and Schetz (39) conducted mass sampling tests in subsonic and supersonic free streams, respectively.

Photographic determination of the size of droplets suffer from several limitations: extremely narrow depth of field, resolution problems and the lack of a sufficient number of droplets in each photograph to constitute a representative statistical sample. To overcome these drawbacks, Gooderum, Bushnell and Huffman (40) used an optical technique devised by Dobbins, Crocco and Glassman (41) to measure the droplets created by water injection into a Mach 8 flow. The technique involved measuring the light scattered from a light beam traversing the spray. The mean droplet diameter was shown to be directly proportional to the injector diameter.

Nejad and Schetz (42) used the light diffraction technique to determine the mean droplet diameter for a variety of liquids injected transversely to a Mach 3 air flow. The mean droplet size was found to decrease with increasing downstream distance and was maximum near the middle of the plume. They also concluded that the droplet size increased with: 1) decreasing dynamic pressure ratios, 2) increasing surface tension for low pressure ratios, and 3) increasing liquid viscosity. The low surface tension liquid tested, a mixture of water and alcohol, atomized within a shorter distance than the other liquids and produced a more uniform spray.

The aforementioned light scattering technique provides information about only the Sauter Mean Diameter of the spray. Swithenbank, Beer, Taylor, Abbot and McCreath (43) developed a technique based on Fraunhofer diffraction which can calculate droplet size distributions. Ruscello and Hirleman (44) extended this

technique by using solid state detectors and developed calibration reticles for such systems.

In regards to the time variation of droplet sizes in sprays, only one previous investigation has tackled this problem. Using holography Ewan, Swithenbank and Sorousbay (45) measured transient droplet size distributions in the periodic spray produced by a diesel injector.

Several in-depth experiments have been conducted concerning the breakup mechanism of liquid jets injected transversely into a supersonic air stream. Kush and Schetz (46, 47) injected a variety of liquids under a range of test conditions. High speed movies (36000 frames per second), rotating mirror photographs (which produce a series of pictures taken a few microseconds apart) and a variety of streak and stop-action still photographs were taken. Many wavelength and wave speed measurements were made of the wave-like disturbances which propagate along the jet column. The jet was observed fracturing at troughs created by large, aerodynamically-induced high frequency waves. The frequency of the jet fracture was of the order of 10 kHz.

Nejad and Schetz (48, 49) extended the work of Kush and Schetz. Glycerine and alcohol water mixtures were injected into a Mach 3.0 air flow in order to quantify the effects of surface tension and viscosity on the waves propagating along the jet column. They determined that 1) increasing the viscosity of the injectant increased the speed of the column waves, and 2) increasing the surface tension decreased the wavelength and the wave amplitude. The surface tension appeared to have little influence on the wave speed. In a different series of

tests using the same liquids, the mean droplet diameter was deduced at various locations in the plume using a light diffraction technique.

In Figure 1 (taken from Ref. 39) a schematic of a liquid jet in a supersonic crossflow has been presented. The picture represents a synthesis of observations made over several different investigations, in particular those of Ref. 39 and Refs. 46-49.

The jet has been divided into three regions. The first region is the cohesive jet column. Capillary-looking waves develop along the column. As the waves propagate along the jet, their speed and amplitude generally grow. Further along the jet column, large aerodynamically-induced waves form; these waves appear responsible for the decomposition of the jet body. The amplitude of these waves are such that the gas boundary layer along the column and the shape of the bow shock become significantly altered. Figure 2, a stop-action photograph of a water jet, clearly illustrates these features.

Once the jet fractures, the liquid is shed into large clumps which are quickly broken down into large drops. The region where clumps are evident has been labeled the spray formation zone. The jet usually fractures shortly after the sonic point behind the curved bow shock. This region is followed by the atomization zone where the liquid is atomized to droplets. The mean diameter of the droplets usually drops below 20 microns in the atomization zone.

The main core of the jet assumes a kidney-shaped cross section as illustrated in Fig. 1. The kidney shape arises from the flattening of

the liquid jet by the cross stream. Droplets also have been observed being shed off the windward surfaces of the jet.

Along the wall or plate through which the liquid is injected, several phenomena have been observed. A small interaction shock occurs slightly upstream of the bow shock creating an oscillating separation region. Two layers of liquid along the wall surface have been identified. The primary surface layer, under certain conditions, extends upstream of the orifice into the separation region. The primary surface layer spreads out covering a wide angle. Below the plume itself is a wake surface layer which is partially created by droplets "falling" into it from the main jet plume. The wake layer is usually significantly thicker than the wider primary layer.

As the schematic indicates, the air velocity in the immediate wake of the plume is subsonic. The fracture, as has been previously mentioned, occurs in a region of supersonic flow. A substantial amount of mixing and atomization occurs in the outer core of supersonic flow.

The high speed movies (Fig. 3) taken in Ref. 46 illustrate the violent nature of a liquid jet in a supersonic crossflow. Kush and Schetz observed the jet "whip" clumps and fragments off itself during the fracture process. In comparison, the work performed by Padye and Schetz (36) in a subsonic air stream revealed no liquid layer close to the injector, and the fracturing process seemed more orderly and not as violent. Figure 4 attests to the regularity of break up in a subsonic air stream.

Researchers have classified liquid jets in supersonic flow into "regimes" according to \bar{q} , the dynamic pressure ratio. Regime 3 jets occur at high \bar{q} 's (greater than values of \bar{q} of 6 or 10, depending on the individual researcher). For a circular injector the jet column near the orifice is circular and without any deformations. Small ripple-like waves appear further along the jet column; these are succeeded by large aerodynamically-induced waves. Jets with a medium \bar{q} of about 5 are said to be in the second regime. Regime 2 jets penetrate less than Regime 3 jets. Kush and Schetz described Regime 2 jets as having a very irregular shape which seemed determined by the waves "which are no longer just perturbations." Compared with Regime 3 jets, these jets have a thicker liquid layer which also extends farther upstream. Regime 1 jets (\bar{q} near unity) have a very short jet column, and the liquid is almost immediately swept downstream. Kush and Schetz reported that very few waves had a chance to develop along the column. Ligaments of fluid were often visible in the plume near the injector. An example of a Regime 1 jet has been pictured in Fig. 5; note that it does not follow the schematic in Fig. 1 which was devised for jets in the other regimes.

The transient behavior of single phase jets, such as an air jet issuing into an air crossflow, have been more extensively studied than that for two phase flows. Rajaratnam (50) presented a review of studies concerning single phase circular jets in a crossflow. A survey of the experimental work performed on single phase flows can be

found in Crabb, Durao and Whitelain (51). A schematic of the flow field created by an air jet, presented in Fig. 6, illustrates the main features of the flow. The jet is deflected due to the pressure field imposed by the crossflow; the jet develops the familiar "kidney" cross section due to the differential bending of the different parts of the jet. A contrarotating vortex pair is formed within the jet close to the injector (as reported by Fearn and Weston (52)). After the region of maximum deflection, the flow field in the jet core becomes fully dominated by the vortex pair. Further penetration is caused by jet momentum and by the entrainment of free stream fluid. Even at great distances downstream, the vortex pair can be detected. Pratt and Baines (53) reported being able to detect the vorticity from the pair 1000 jet diameters downstream of the orifice. In addition to the bound vortex pair, vortices are alternately being shed off the jet column. Clearly, vortices dominate the flow field for single phase jets.

The shed vortices are similar to the ones reported by Roshko (54, 55) who studied the flow past solid cylinders. Moussa, Trischka and Eskinazi (56) performed extensive velocity and vorticity measurements in the near field of an air jet in a crossflow. Their experiments delineated the position of the vortex pairs, and they also concluded that the Strouhal number was 0.2 for the flows tested. The Strouhal number was designed to relate the frequency of vortex shedding to the free stream velocity and the cylinder diameter for the flow past rigid cylinders. The Strouhal number of 0.2 corresponded to the value given

for rigid cylinders at the same Reynolds numbers. McMahon, Hester and Palfrey (57), following an idea used by Roshko, placed a splitter plate in the wake of a transverse air jet. The thin metal plate was placed in the near wake and was aligned with the free stream. The plate inhibited the formation of the shed vortices. A frequency analysis of the energy in the wake confirmed that the splitter plate had reduced the observed amplitude of the shed vortices by 75%.

The present study was aimed at quantifying the transient behavior of a liquid jet injected transversely into a high speed air stream. Both subsonic and supersonic cross streams were tested. Two principal types of measurements were made. An instrument to size droplets using the Fraunhofer diffraction technique was designed and built. In order to obtain the time variation of the droplet size distributions, the instrument was centered around a high speed video camera. A Fraunhofer technique was chosen over a Laser Doppler system, since the latter would not have provided information on the transient character of the spray. Since a Doppler system measures droplets one at a time, it would have been difficult to distinguish the droplet-to-droplet variations from the larger scale fluctuations in the spray. The Fraunhofer technique sizes ensembles of droplets and, consequently, yields information on fluctuations in the spray. Since the size distributions were desired, the diffraction technique for mean droplet size developed by Dobbins, Crocco and Glassman was not used either. The system developed for this report can measure droplet size distributions at sampling rates of up to 9 kHz.

The second type of measurement involved the extinction of a laser beam traversing the plume. The extinction or the obscuration of the beam can be related to the number and to the size of droplets through which the beam had passed. A Fast Fourier Transform was performed on the extinction signal to identify the frequency of the observed fluctuations.

The tests were conducted at low and high \bar{q} for both water and water/methanol mixtures. Circular orifices of 0.508 and 0.91 mm diameters were used in the injectors. Crossflow Mach numbers of 0.48 and 3.0 were tested.

To analyze the results, the data will be presented in several forms. Droplet size distributions in both graphical and tabular form will be presented to show the various size groupings in which the droplets tended to be found. To quantify the fluctuations inherent in the distributions, the Sauter Mean Diameter and the standard deviation of the SMD will be calculated. The numerical rise and fall of the SMD will be demonstrated in tabulated time histories of that quantity. Since the fluctuation frequency could not be accurately determined from the droplet size measurements, frequency analyses of the extinction traces also will be presented. Data from this and previous investigations will then be discussed, and a physical model of the transient jet will be developed. In addition, the dimensions of the jet plume will be deduced from a series of cross sectional photographs of the jet.

II. DROPLET SIZE DISTRIBUTION TECHNIQUE

2.1 Theory of Fraunhofer Diffraction

When light passes through a grating, transparency, aperture or some other optical obstacle the light beam diffracts. For example, light passing through a small circular aperture diffracts forming the familiar Airy ring pattern. The resulting light field can be calculated by using the Huygens-Fresnel principle. Under certain circumstances, these equations can be greatly simplified. If the assumptions for Fraunhofer diffraction are satisfied, then the diffracted light energy distribution can be calculated by performing a Fourier transform on a mathematical description of the aperture. The phenomenon of Fraunhofer diffraction will be discussed in the following paragraphs. Goodman (58) is the chief reference for this discussion.

The opacity of an aperture can be described mathematically. A circular aperture, for instance, can be described by the circ function:

$$\text{circ}(\sqrt{x^2 + y^2}) = \begin{cases} 1 & \sqrt{x^2 + y^2} \leq d/2 \\ 0 & \text{otherwise} \end{cases} \quad (2.1)$$

If the function equals unity at a certain coordinate then the aperture is transparent there. An opaque point on the aperture is assigned a value of zero. When a Fourier transform is performed on the aperture

function, the variables of the transform are two spatial frequencies, u and v . To translate these variables into the physical coordinates (x and y) on the viewing screen, the following relations hold:

$$u = \frac{x}{\lambda z} \quad \text{and} \quad v = \frac{y}{\lambda z} \quad (2.2)$$

where z is the distance from the aperture to the screen and λ is the wavelength of the illuminating light.

Fraunhofer diffraction essentially decomposes the mathematical description of the aperture into a Fourier series. Each point of the diffraction pattern corresponds to one term in the sine or cosine series. The intensity of the light at a point is proportional to the coefficient of the sine or cosine term, while the coordinate of the point determines the frequency and the argument of the term. To satisfy the criterion for Fraunhofer diffraction one of the following conditions must be satisfied:

- 1) The viewing screen must be placed a great distance behind the aperture. For visible light the minimum distance is of the order of several thousands of meters.
- 2) The aperture must be illuminated by a spherical wave converging on the screen.
- 3) A converging lens must be positioned between the aperture and the screen. The viewing screen must be placed one focal length behind the lens.

For the last circumstance, the one most often encountered in the laboratory, the frequency-coordinate relations reduce to:

$$u = \frac{x}{\lambda f} \quad \text{and} \quad v = \frac{y}{\lambda f} \quad (2.3)$$

where f is the focal length of the converging lens.

In order for the resulting light field to be an exact Fourier transform (within a multiplicative constant), the aperture must be placed in the forward focal plane of the lens. If this last condition is not met, however, only the phase of the light is affected, and the intensity remains unchanged. For aperture or droplet sizing, the phase is not important; only the intensity as a function of radial distance needs to be measured and analyzed. In practice the lens is positioned as close as possible to the aperture. Due to the frequency-coordinate relation, the lens acts as a low pass filter. High frequency information, which is diffracted through relatively large angles, passes askew to the lens, and consequently does not contribute to the image formed on the viewing screen. By placing the lens close to the aperture high frequency diffracted light can be collected and transmitted by the lens.

In Fraunhofer diffraction theory, an opaque disk diffracts the same light energy as a circular aperture; the only difference lies in the intensity of the center spot (the undiffracted beam). Furthermore, as long as the aperture is completely illuminated, the position of the aperture has no effect on the diffraction pattern.

Consequently, this droplet sizing procedure is not sensitive to the location or the motion of the diffracting droplets.

2.2 Droplet Size Distribution Calculations

Under the Fraunhofer assumptions, a sphere diffracts the same light energy as a disk of the same diameter. In Fraunhofer diffraction, only the projected cross sectional area of the obstacle matters. When sizing droplets, the droplets are assumed to have a circular cross section and, consequently, they can be treated in the same fashion as an opaque disk or circular aperture. The Fourier transform of the circ function is the Bessel function, so the light energy on the viewing screen can be expressed as:

$$U(r) = e^{ikf} e^{ikr^2/2f} \sqrt{\frac{E}{A}} \frac{kd^2}{8i} \left[\frac{2J_1(kdr/2f)}{kdr/2f} \right] \quad (2.4)$$

where E is the light energy incident upon the aperture and A is the aperture area. A parallel beam of monochromatic light has been assumed to be the source of the illumination; the wave number associated with the light is $k=2\pi/\lambda$. The intensity at a point on the screen can then be written as:

$$I(r) = |U(r)|^2 = \frac{EA}{\lambda^2} \left[\frac{2J_1(kdr/2f)}{kdr/2f} \right]^2 \quad (2.5)$$

On the viewing screen, the fraction of light falling within a circle of radius r can be calculated by integrating the above expression:

$$L(r) = \frac{1}{E} \int_0^r \int_0^{2\pi} I(\rho) \quad (2.6)$$

The amount of light energy striking between two rings of radii r_1 and r_2 can be written as:

$$L(r_1, r_2) = E[J_0^2(kdr_1/2f) + J_1^2(kdr_1/2f) - J_0^2(kdr_2/2f) - J_1^2(kdr_2/2f)] \quad (2.7)$$

The above expression is valid for diffraction by a single droplet. Since the problem is linear, the resulting diffraction pattern created by an aggregation of droplets can be expressed as the sum of the diffraction patterns created by each droplet, individually. The energy constant E then becomes the amount of energy incident upon each droplet. This energy is proportional to the cross sectional area of the droplet. Furthermore, if there happens to be N droplets of diameter d , then multiplying the above expression by N yields the diffraction pattern caused by that set of droplets. It is customary in this type of work to calculate the size distributions in terms of

volume fractions. Consequently the number of droplets in a set, N , is replaced by $3V_i/4\pi(\frac{d}{2})^3$ where V_i is the volume of that particular droplet set.

$$L(r_1, r_2) = \frac{3E}{2} \sum_i \frac{V_i}{d_i} [J_0^2(kd_i r_1/2f) + J_1^2(kd_i r_1/2f) - J_0^2(kd_i r_2/2f) - J_1^2(kd_i r_2/2f)] \quad (2.8)$$

The summation above is over all sets of droplets. A series of these equations exist, since an equation exists for each ring examined on the screen. The set of equations can be expressed in matrix form. The intensity contained within each ring and the volume fraction for each set of droplets would be each represented by a vector, \vec{L} and \vec{V} , respectively.

Usually the droplets are arranged into bins. One bin, for example, may be comprised of droplets whose diameters fall within the range of 20 to 30 microns. A uniform distribution is assumed within each bin. Since the diffraction pattern from each bin has a definite maximum peak (technically, the first maximum), the light detecting rings are arranged such that a ring is centered over each of the peaks resulting from the various droplet bins. If the droplets are to be arranged into ten bins, then the light energy falling within ten rings needs to be measured. The entire process results in a size

distribution histogram with a bar representing the droplets in each bin.

Since the vector L is measured in the laboratory, the matrix equation must be inverted:

$$\vec{L} = [J]\vec{V} \quad \text{to} \quad \vec{V} = [J]^{-1}\vec{L} \quad (2.9)$$

The problem is ill-conditioned, since the matrix is nearly singular. A simple inversion scheme will not suffice. Phillips (59) and Twomey (60) studied the problem and developed a smoothing inversion routine. Their technique was implemented by Caroon and Borman (61) to successfully predict the diffraction pattern produced by a hypothetical droplet size distribution. This approach was used in the present work. In part, the sizing technique described above follows the method pioneered by Swithenbank, Beer, et al in Ref. 43.

2.3 Droplet Sizing Errors

Droplet sizing methods are plagued by a number of sources of possible error. One source of error has already been mentioned: low pass filtering by the lens. In the present work, the droplet diameters examined ranged from 7 to 100 microns. For the optical arrangement used, the first maximum of the diffraction produced by a 7 micron droplet should be collected by the lens without any significant filtering effects.

Another problem, beam steering, arises when gradients in the index of refraction occur in the gaseous medium within and surrounding the spray. As stated in Ref. 62 these gradients occur when the droplets evaporate or combust. Past experience has shown that the liquids used in this experiment do not show any appreciable evaporation since the residence time of the observed droplets is too short for the droplets to evaporate at the tested conditions.

The density gradients associated with shock flow may also steer the beam or, acting as a lens, may bring the diffraction pattern to focus in some plane other than the focal plane of the converging lens. In regards to the first effect, the position of the central, undiffracted beam along the video linear array was manually verified for each run. Within the resolution of the system (75 microns) the location of the central beam did not shift when the tunnel was started. Furthermore, for some of the tests, the linear array was rotated and still no deflection of the beam could be discerned. In conclusion, if the shock wave did steer the beam, then it presumably caused a negligible distortion in the diffraction pattern.

If the shock wave acted as a lens then the linear array would see an out-of-focus diffraction pattern. Unlike some other Fraunhofer systems, the present system does not need the intensity of light near the central beam. The system requires information at radial distances spanning from 1.4 to 24 mm from the central beam. Consequently, if the optics are out of focus and the central beam spot is smeared then the focussing error would have to be enormous in order for the central

beam to "spill" across the pattern and affect the results. Since the light energy is integrated along segments of the linear array, smearing of the rest of the diffraction pattern should exert only a minimal influence on the results. In either case, if the focussing problem was of such catastrophic proportions that the results would have been affected then the smearing of the undiffracted beam should have been evident on the oscilloscope display; no such focussing errors were ever detected.

Multiple scattering occurs when light which has been diffracted off one droplet becomes further diffracted by another droplet. Multiple scattering predominantly occurs when the spray is densely populated with droplets. Previous investigators have correlated the errors of multiple scattering in liquid sprays with the transmission of the illuminating beam. The transmission is defined as the percentage of the light which is neither diffracted nor absorbed while passing through the spray. Dobbins, Crocco and Glassman (41) recommended that the optical depth be kept below 1.5 in order to avoid serious errors. An optical depth of 1.5 corresponds to a transmission of 22%. In a subsequent investigation by Dodge (63), the errors accrued in the Sauter Mean Diameter (SMD) and in the Rosin-Rammler parameters for a variety of sprays from multiple scattering were measured. Multiple scattering errors were found to increase dramatically with decreasing transmission and with decreasing SMD. The transmission was greater than 60% for the vast majority of tests conducted in the present study. According to the plots presented by

Dodge, a transmission of 60% is indicative of a multiple scattering error of less than or equal to 5% in the SMD and the Rosin-Rammler parameter calculations for a spray whose SMD is 20.5 microns.

The transmission dropped below 60%, in this study, for measurements made near the injector. Close to the injector another problem arises: the jet has not atomized and the assumption that the liquid droplets have circular cross sections is of dubious merit. In the data presentation sections, those measurements whose accuracy is suspect will be pointed out.

III. EXPERIMENTAL APPARATUS AND PROCEDURES

3.1 Test Facility

Tests were conducted in the Virginia Tech 9 in x 9 in (23 cm x 23 cm) supersonic wind tunnel. The tunnel is of the blow-down variety and has interchangeable test sections which allow different Mach number flows to be tested. For the measurement of stagnation pressure, a Pitot probe was mounted in the settling chamber. The probe was connected to a Frederic Flader Engineering Physics Division transducer with a range of 0-100 psi. Two static pressure ports were installed in the wall of the subsonic test section upstream of the injector. These ports were connected to a MB Electronics 151-DBA-1 Transducer which had a range of 50 psi. The ratio of the static and stagnation pressures were used in the calculation of the Mach number in the subsonic test section. The output of the transducers were recorded on a Hewlett Packard Model 7100 Strip Chart.

The supersonic test section produced a Mach number of 3.0. Throughout this series of tests a stagnation pressure of 4.3 atm \pm 1.5% was maintained. For the subsonic tests, the Mach number was 0.48 and the stagnation pressure was 1.4 atm \pm 10%. For all of the tests the stagnation temperature was that of the ambient air ranging from 10 to 20° C.

3.2 Injection System

A nitrogen bottle pressurized the large reservoir tank containing the liquid to be injected. The pressure was regulated between 3 and 15 atm depending on the desired \bar{q} . A NUPRO Model B6TF2-60 filter with a 140 micron mesh was installed in the quarter inch tube which connected the tank to the injector model. The mass flow rate of the injected liquid was measured by a Micron Motion Model C25A-UL non-intrusive flow meter. The flow meter was calibrated in the laboratory for flow rates spanning its range of 0-100 gram/sec.

For the supersonic crossflow tests, the liquids were injected through a flat plate model. The dimensions of the plate were 10.0 x 15.25 x 0.8 cm. The model had a sharp leading edge and was attached to the test section floor by a 5.0 cm tall support as depicted in Fig. 7. The support had a diamond cross section and was centered in the test section. The injection orifice was located 8.0 cm downstream of the leading edge. The orifice had a 1/16 in (1.6 mm) straight run and a smooth conical entry passage. The diameter of the circular orifice was 1/50 in (0.508 mm).

An injector was mounted in the floor of the subsonic test section. The orifice had a 1/28 in (0.91 mm) diameter and a short straight run preceded by a conical entry passage.

Two liquids were injected: a methanol/water mixture and pure water. The mixture was 10% methanol by volume and was injected whenever the outside ambient air dropped in temperature in order to

prevent the formation of ice crystals in the spray plume and on the flat plate. The density of the mixture was 0.98 g/ml; the viscosity was 1.005 centipoises; and, the surface tension was 58 dyne/cm. The properties of the water were, respectively, 1.0 g/ml, 1.0 cp, and 73.5 dyne/cm.

3.3 Droplet Sizing System

An instrument to obtain the size distribution of droplets in a spray was designed and built in the laboratory. The system calculated the droplet sizes by use of the previously described Fraunhofer diffraction technique. To measure the diffraction pattern, a high speed video camera was used. The high data speed was needed to measure transients in the size distributions. Since the diffraction pattern was radially symmetric, the light energy distribution was calculated using the intensity detected along a radial line. A mini-computer equipped with a high-speed ADC board collected and reduced the data. Due to the relatively long calculation time required to reduce the data, the data was collected and stored on disk during the wind tunnel runs and reduced afterwards.

3.3.1 Optical Arrangement

A schematic of the optical system is shown in Fig. 8. All components were mounted on one of two optical benches located on either side of the test section. Both benches possessed two degrees

of freedom to allow for easy alignment. Thick cork sheets isolated the benches from vibrations prevalent in the floor.

The light source was a 5 milliwatt Helium-Neon laser, a Spectra Physics Model 120. A JODON Model BET-25 spatial filter assembly cleaned and expanded the beam to a diameter of about 1 mm. The beam passed through high quality windows installed in the side walls of the test section. A plano-convex lens, 5.2 cm in diameter and with a focal length of 50 cm, converged the beam onto the video camera.

A Charge Coupled Device (CCD) was used as the video camera. The solid state sensor consisted of a linear array composed of 2048 pixels or picture elements. Located on 13 micron centers, the pixels were 13 x 13 microns in size. The dynamic range of the device was 1000:1 relative to peak-to-peak noise and 5000:1 relative to RMS noise. The equivalent ASA of the device was slightly less than 100. A Fairchild CCD1500R Industrial Line Camera was chosen, since it could measure the light energy distribution along an inch long line segment and could make the measurement quickly, repeatedly and accurately. The necessary length of the linear array was dictated by the selected range of droplet sizes under investigation.

3.3.2 Electronics

For the operation of the CCD camera, two clock inputs were required. Each clock signal consisted of a train of pulses that triggered some action inside the camera. The data clock determined the rate at which information was transmitted out of the CCD. Each

datum was comprised of a voltage step. The voltage was proportional to the light energy which a single pixel had received during the previous exposure. The data from the row of pixels was transmitted in a serial fashion. The exposure time was controlled by the exposure clock. As the CCD received each exposure clock pulse, a new picture was taken, and the data from the previous exposure was transmitted.

A crystal-controlled oscillator based on an HEP C3805P chip produced the data clock signal. A variety of crystals ranging from 1 to 20 MHz were installed in the circuit. The exposure clock was an Electro-Pulse megacycle pulse generator. Both of the clock signals were fed through a T.I. uA9638 differential line driver chip for conditioning before being transmitted to the CCD.

The exposure clock pulses also triggered the data acquisition system. An Applescope D2 ADC board installed in a Franklin Ace 1000 mini-computer sampled the data with digitization rates of up to 3.5 MHz. The computer-based digital oscilloscope system had an absolute accuracy of $\pm 1\%$ and had a maximum slew rate of 4 V/microsec. To convert the output signal of the CCD to the proper levels for the data acquisition system, an offset amplifier was constructed using TL 081 high speed op amps.

The entire system was operated at data rates ranging from 1 to 20 MHz and with exposure times from 0.1 to 60 milliseconds. Data from 270 to 350 pixels were used to calculate each droplet size distribution. Since the ADC buffer memory could hold only 1024 data

points, at most only three size distributions could be obtained consecutively.

3.3.3 Software

The software was written for a 10 x 10 matrix which required the light intensity striking ten concentric rings. The input data consisted of the intensities received by each pixel positioned along a radial line. Each intensity was multiplied by the square of the radial distance from the pixel to the center of the diffraction pattern. Within a multiplicative constant these numbers represented the intensity striking a ring of differential width. A composite Newton-Cotes closed integration scheme was then used to calculate the intensity falling within each of the ten rings.

The data clock rate usually exceeded the digitization rate of the ADC. Consequently, the series of voltage steps were smeared by the data acquisition system into a smooth curve. Radial distances along the CCD sensor were computed using formulae that related the computer sampling time to the data clock rate and to the length of each pixel.

The laser beam had been positioned such that it struck the CCD near one end of the sensor. This arrangement allowed accurate knowledge of the location of the beam and permitted radial distances (from the beam center) to be known. To determine the location of the undiffracted beam on the CCD sensor, the sampled data was displayed by the computer on an oscilloscope-type screen. A cursor was manually positioned over the voltage peak corresponding to the beam and the

sample number recorded. The undiffracted beam location was determined for each test run.

Another parameter which the software required was the voltage that corresponded to total darkness. This parameter was obtained by daily calibration of the CCD sensor.

The same matrix was used for all of the tests. The matrix calculation only involved the diameters defining the droplet size bins and the radii of the light detecting rings, neither of which changed during the course of the experiment. A separate data reduction program, however, had to be devised for each data clock rate. Changing the data rate changed the relationship between sampling time and length along the linear array.

3.3.4 System Accuracy

The accuracy of the droplet sizing system was checked by using a Laser Electro-Optics RR-50-3.0-0.08-102-CF calibration reticle. The size distribution of the particles present on the reticle was known. The actual distribution and a calculated distribution are graphed in Fig. 9.

From the calculated size distributions the Rosin-Rammler parameters \bar{x} and n were calculated. Under exposure conditions similar to those found during wind tunnel testing, the parameters were consistently calculated within 6% of their true values. The calibration tests were conducted over a wide range of exposure times and digitization rates.

During wind tunnel testing, the system accuracy was further checked by computing the Sauter Mean Diameter (SMD or $D_{3,2}$) and comparing the calculated SMD with those obtained by previous investigators. Nejad and Schetz (42) measured the SMD for water injection into a Mach 3.0 air stream using the diffraction scheme developed by Dobbins, Crocco and Glassman (41). The mean droplet diameters calculated with the present system agreed with those of Nejad and Schetz as long as the SMD was greater than 16 microns. For smaller SMD distributions, two phenomena occurred:

- 1) Droplets shifted within the 7-15 micron bin. Since this shift was confined within a bin, the shift was not observable in the calculated distributions. This phenomenon produced sizable errors due to the large population of this bin for small SMD distributions.
- 2) A large percentage of droplets apparently had diameters less than 7 microns.

Although the latter effect would produce a misleading calculated distribution profile, these errors primarily affect the SMD calculations and not the distribution calculations. Nejad and Schetz also determined that the SMD dropped to around 16 microns only at a great distance (100 orifice diameters) downstream of the injector at these conditions.

In summary, between the reticle and wind tunnel injections, the accuracy of the system in calculating SMDs was verified for distributions with SMDs ranging from 17 to 40 microns. The accuracy

of the system in determining particle distributions was checked directly for a 40 micron SMD distribution. Presumably the calculated distributions are valid at lower values of SMD down to 17 microns.

3.4 Frequency Measurements

For this series of measurements, the lens and CCD camera were replaced by a RCA Model C7164R photomultiplier tube. The photomultiplier had a black face plate that had a 0.15 mm aperture drilled in its center. The output signal was fed into a Tektronix AM 502 differential offset amplifier before being analyzed by the data acquisition system. A Fast Fourier Transform program searched for high frequency oscillations in the signal.

The above setup measured fluctuations in the extinction of the laser beam. Since the liquids tested absorbed little light, the resulting fluctuations must arise principally from changes in the droplet sizes. In one test, the laser beam was focussed on the windward edge of the liquid jet column in order to measure the frequency of waves propagating along the column.

3.5 Photographic Setup

A variety of photographs were taken. In all cases, Polaroid Type 57, ASA 3000, film was used in a simple bellow box camera. Stop-action shots of the jet were taken with a Strobotac strobe flash. The duration of the flash was approximately 10 microseconds.

To photograph the cross section of the spray plume, the camera was used with a varying shutter speed. To illuminate the plume, the laser beam was expanded in one direction by a cylindrical lens. The resulting sheet of light was passed through the plume at an appropriate downstream location. To obtain the dimensions of the plume, a photograph of a grid was taken for each setup. The grid allowed for accurate measurements of the plume, since it compensated for the fact that the photographs had been taken at an angle.

3.6 Experimental Procedures

The lights in the laboratory were extinguished during testing. Each run lasted close to 15 seconds. Before the data acquisition system was triggered, the flow in the tunnel and the injection were allowed to stabilize. When the tunnel was shut down, the injection was stopped first to prevent the spray from reaching the windows. This procedure allowed for ten seconds of measurement time. Since the computer required about 3 seconds to transfer each set of data from the ADC buffer memory to a disk, only three sets of data could be taken during each wind tunnel run. Each set of data would later be reduced into one to three size distributions. The number of distributions was dependent on the data and exposure rates.

In order to achieve the proper laser intensity for the diffraction experiments, a combination of neutral density filters and a continuously variable polarizing filter was often positioned between the laser and the spatial filter. The wind tunnel was run with

injection in order to determine the proper combination of filters for the proper exposure. This procedure was performed for each test condition. The 0.11 msec exposure time, for the orifice sizes, liquids, and CCD used, necessitated the full strength of the laser; for these tests all of the neutral density and polarizing filters were removed.

IV. RESULTS

4.1 Description of Measurements

Most of the data presented in this report are results of the transient droplet size distribution measurements. Some of this data could be easily misinterpreted due to misconceptions about the measurement procedure, so the purpose of this section is to clarify the significance of the presented data.

The droplet size distributions were calculated from "video photographs" of the diffraction pattern. A certain exposure time was used in each sequential series of photographs. The time between sequential photographs was of the order of a few nanoseconds and can be ignored. Essentially, each distribution was a time-averaged one averaged over the exposure time. Whether or not the distribution can be considered to be a "stop-action portrait" or a "time-smeared view" of the jet activity depends on the relative magnitudes of the exposure time and the period of the event.

The shortest exposure time used in this work was 0.11 milliseconds, which corresponds to a frequency of 9 kHz. Since the dominant jet fluctuation was that of fracture which occurred at frequencies of several kHz for the jets in supersonic flow, there was "time-smearing" in the droplet size measurements. However, as will be demonstrated in a later section, the nature of the fluctuations permitted a considerable amount of information to be gathered about the transients in the jet. For injection into a subsonic crossflow,

the jet fractured at higher frequencies. In those tests, relatively little information was obtained on the effects of fracture on droplet sizes.

Partly to succinctly quantify the fluctuations, an average diameter was determined for each distribution. The average diameter calculated was the Sauter Mean Diameter (SMD or $D_{3,2}$). To obtain the SMD, each bin in the distribution was represented by the diameter corresponding to the arithmetic mean of its two defining diameters. For example, if 10% of the droplets by volume were in the 7-15 micron bin then it was assumed that 10% of the droplets had a diameter of 11 microns. This assumption, as has been previously stated, can lead to noticeable error, especially if a bin spanning a wide range of diameters had a significant population. The SMD was computed using the following relationships:

$$\text{SMD} \equiv \frac{\sum n_i d_i^3}{\sum n_i d_i^2} = \frac{1}{\sum \frac{1}{d_i^2} / \sum n_i d_i^2} = \frac{1}{\sum \frac{V_i}{d_i^2}} \quad (4.1)$$

$$\text{where } \frac{V_i}{d_i^2} = \frac{n_i d_i^3}{\sum n_i d_i^2} \quad (4.2)$$

To permit the subsequent calculation of other, differently defined mean diameters, a number of typical distributions have been tabulated in the Appendix.

The standard deviation in the SMD for each set of distributions was calculated also. For comparison purposes, the standard deviations presented have been non-dimensionalized by dividing by the mean diameter. These numbers should indicate the severity of the fluctuations in the droplet sizes. For a similar purpose, time histories of SMDs are presented also. These histories indicate the range of values the SMD attained and also indicate the speed with which the SMD fluctuated. In the tables, sequential SMD measurements are separated by a comma while sets of data are separated by a slash.

The goal of the laser beam transmission/extinction survey was to accurately measure the frequency of events within the plume. Due to the high frequencies involved, the droplet size measurements could not provide a definite frequency for the jet fracture. From examination of the data collected during the runs the extinction seemed to reflect the effects of jet fracture and break up.

The extinction survey provided other information. The rms value of the transmission was recorded for each test. The transmission value was expressed as the percentage of light that was neither diffracted or absorbed during its passage across the spray plume. Consequently, the transmission should be inversely proportional to the number of droplets through which the beam passed.

In order to input the voltage output of the photomultiplier into the data acquisition system, the photomultiplier signal had to be offset and amplified so that it would range from -1 to +1 V. The

amplification factor required also was noted; this factor should be inversely proportional to the relative amplitude of the fluctuations.

The droplet size and the extinction measurements were performed in a two-dimensional test grid; measurements were not made in the y-plane (across the breadth of the plume). To obtain some idea of the jet behavior in this third dimension, cross-sectional photographs were taken. In some of the photographs, the relatively steady core of the plume can be delineated from the fluctuating outer regions. The steadier regions of the plume appear brighter on the photographs. Visual observations of the jet during wind tunnel runs confirmed that these outer regions did appear to fluctuate, rapidly vanishing and re-appearing. Attempts to quantify these plume fluctuations by using the CCD camera failed due to the low intensity of the light reflected off the droplets.

The CCD, however, could be used to measure the time fluctuations of the penetration of the plume. In these tests, the laser was replaced by a mercury vapor lamp whose light was converged onto a concave mirror. This arrangement illuminated the plume with a large beam of parallel light. This is the traditional arrangement for the taking of penetration photographs. Instead of a still camera, however, the CCD camera was used aligned perpendicular to the free stream flow. Several investigators have reported that streak photographs underestimate the penetration height (Ref. 37 and 39). By using the CCD it was hoped to determine the plume fluctuations and to bypass some of the difficulties of the traditional techniques. Part

of the photographic method failure had been blamed on film contrast and gradation characteristics and on the difficulty of delineating the jet boundary on the streak photographs. The CCD, by accurately measuring the intensity of light passing through the plume, should be at least partially immune to both of these effects. The CCD would not be immune to error if the optics of the situation were to blame for the errors.

Besides measuring the penetration, the CCD method should provide information on the density of droplets in the plume. In essence, the CCD would have measured the extinction at 2048 points along the plume simultaneously. To verify the accuracy of this method the results were compared with the laser beam extinction survey and the mass sampling data reported by Thomas and Schetz (39). The extinction data correlated with the mass sampling results. A large mass flux was found to absorb and/or diffract a proportional amount of the beam's intensity.

In the data presentation to follow, all distances and lengths in the plume have been non-dimensionalized by the injector diameter.

4.2 Injection into a Subsonic Air Stream

In these tests, water was injected at a momentum flux ratio \bar{q} of 10. The Mach number of the free stream was 0.48. Measurements were made at a variety of downstream stations (x) and heights (z).

4.2.1 Droplet Sizes

Droplet size distributions were recorded at three different exposure times: 0.35, 3.5 and 60 milliseconds. In Fig. 10, distributions throughout the plume as observed at an exposure time of 0.35 msec have been plotted. The breakup and atomization of the jet can be readily identified in the plots. At the $x/d=10$ station, the droplets were predominantly in the 20-35 micron bins. At the $z/d=5$ location, below the main core of the jet, a significant population of the droplets also resided in the smaller bins. Farther downstream at the $x/d=100$, $z/d=10$ and the $x/d=50$, $z/d=5$ locations, the spray had been well atomized with a large percentage of the droplets being smaller than 20 microns. At the intermediate locations, the droplets were seen shifting gradually toward the smaller bins. The droplet size distribution curves roughly resembled a Gaussian curve. For the well atomized sprays, only the right half of a Gaussian profile was evident. Presumably, there were significant numbers of droplets with diameters less than 7 microns at these locations.

The same trends can be identified in Fig. 11. These distributions, recorded with a 3.5 msec exposure, were obtained at various x/d stations. In the z/d direction, these locations roughly followed the increasing penetration of the main jet core. The gradual atomization and the Gaussian profiles are as evident at this exposure time as they were in the 0.35 msec tests.

A comparison of how the size distributions differed at various exposure times is presented in Fig. 12. This data was recorded at $x/d=100$, $z/d=20$. The 0.35 msec samples, Fig. 12a, revealed a Gaussian profile centered around 25 microns, while the 3.5 msec samples in Fig. 11d exhibited relatively few droplets in this regime. The 60 msec sample appeared to be a composite of the distributions discovered at the two shorter exposure times. Figure 13 was recorded at $x/d=50$, $z/d=10$, and again the 60 msec results appeared to be a composite of the short exposure distribution profiles.

The three distributions in Fig. 14 were recorded at an exposure time of 0.35 msec, but they were taken at three second intervals. This comparison demonstrated that the shape of the distribution profiles did not change significantly over long time intervals for this test condition. The general trend found for the 0.35 and 3.5 msec trials was that, if the distributions did not change dramatically from one sample to the next, then they did not change over longer intervals. The 60 msec tests never showed any significant deviation from one sample to the next.

In Fig. 15 the SMD has been given as a function of x/d and y/d . The corresponding non-dimensionalized standard deviation and exposure time have been included. In each column of the plot (i.e. at each x/d station), the main core of the jet can be identified. Since the fractured clumps form the core, the SMDs were large and the deviations substantial. The standard deviations were also large along the jet boundary due to turbulent mixing in these regions. For a constant

z/d , the trend was that SMD decreased with increasing x/d . The variations of the standard deviation with x/d was unclear, though the largest values were obtained near the injector and along the jet boundary. The deviations at $x/d=100$ were smaller than the ones recorded at $x/d=50$, which in turn were smaller than those at $x/d=10$.

At each location, the lowest standard deviation was always obtained at the 60 msec exposure time. The SMD found at the 60 msec exposure was either between the diameters recorded at the two shorter exposure times or was less than both of them. The former situation is analogous to the 60 msec distributions being a composite of the other two. There was a trend that the standard deviations for the 0.35 msec trials were larger than those for the 3.5 msec ones at the $x/d=10$ and 30 stations and vice versa for larger x/d .

Table 1 lists the time histories of SMD for several locations for an exposure time of 0.35 msec. The SMD was observed to fluctuate over a considerable range, seemingly randomly. If the SMD is assumed to fluctuate with a constant period, these histories would indicate that the exposure lasted several periods. If the exposure had covered many cycles, then the fluctuations would have been averaged out. If the exposure time had been short compared with the period, then the SMD would have varied only slightly between sequential measurements while varying substantially between the sets of measurements. Alternatively, depending on the waveform of the fluctuation, the exposure time might have been of the order of or slightly less than the fluctuation period.

4.2.2 Extinction Measurements

Two extinction traces are shown in Fig. 16. The traces reflect the variation in the intensity of the part of the laser beam that was neither absorbed or diffracted in its passage through the plume. High speed oscillations are evident in the traces. To quantify these oscillations a Fast Fourier Transform (FFT) was performed on the extinction signals. Fast Fourier Transforms were performed at stations ranging from $x/d=20$ to 100. The results can be classified into two groups according to plume location and to the form that the frequency distribution assumed. The FFTs of the first group, exemplified by the FFT in Fig. 17 taken at $x/d=20$, $z/d=5$, exhibited much activity at frequencies of a few kHz. Fluctuations occurred at a lesser amplitude up to a frequency of about 20 kHz. The FFTs performed at $x/d=20$, $z/d=10$ and $x/d=50$, $z/d=10$ were similar. The frequency distributions of the second group roughly followed a Gaussian curve ranging from 5 to 120 kHz. Typical of the FFTs belonging to the second classification is the analysis performed at $x/d=100$, $z/d=25$, plotted in Fig. 18. The frequency curves obtained at the other $x/d=100$ locations as well as at $x/d=50$, $z/d=5$ and 20 and $x/d=40$, $z/d=5$ were similar. The FFTs performed at the $z/d=5$ and 10 heights, however, did not extend to quite so high a frequency. As shown in Fig. 19 for the $x/d=100$, $z/d=5$ location, the FFTs obtained at low z/d extended to only 60 kHz.

A close examination of Fig. 16 revealed that the signal followed a certain pattern. The symbols (V) on the figure denote the beginning

of each pattern - a gentle downward slope followed by a sharp dip and a tall peak. The pattern was not always consistent and was often disrupted by violent fluctuations in the signal. Considering the turbulent, violent nature of the jet breakup, the existence of even an occasionally evident pattern was surprising. The pattern was seen at several other locations as documented in Table 2. The pattern occurred at a frequency of 15 kHz, except at the $x/d=100$, $z/d=25$ location where the frequency was doubled. The $z/d=25$ location was closer to the jet boundary than the other locations listed in the table. These frequencies fall below those detected by the FFT analysis. The FFT routine searched for sinusoidal variations in the extinction signal; it would be oblivious to the pattern although it would detect and count each of the pulses of which the pattern is composed.

The largest amplitude extinction fluctuations were observed at $z/d=20$ in the surveys made at $x/d=50$ and 100. The locations which exhibited the highest frequencies have been listed in Table 3. The $z/d=5$ location consistently produced high frequency fluctuations as did locations near the jet boundary. In comparison, the largest deviations in the SMD (also tabulated) were found between $z/d=5$ and 10 at every x/d station as well as along the jet boundary.

4.2.3 Photographic Results

Figure 20 displays a cross sectional photographic view of the jet at $x/d=100$. A cross sectional slice of the spray plume has been

illuminated by a sheet of light. The plume has a basically circular cross section. Since the photograph was taken upstream of and above the injector, the plume cross section appears ovoid. The outer edge of the plume is not as bright as the central core; the reduced brightness can be attributed to the severe fluctuations the outer rim of the plume underwent during the exposure time. Also visible in the sheet of light is the liquid layer that develops along the flat plate. In the photograph, the liquid layer appears between the plume and its reflection on the flat plate. The jet upstream (to the left) of the illuminating sheet of light also is visible.

Measurements of the jet plume dimensions as obtained from the series of cross sectional photographs are presented in Table 4. A schematic of the jet showing the relevant dimensions is shown in Fig. 21. The table differentiates between the brighter inner core and the outer extent of the plume. The central core and the outer core grew at identical rates. Between $x/d=20$ and 100, the height and the width of both cores increased by a factor of 1.5. Over the same distance, the liquid layer nearly doubled its dimensions.

Figure 22, taken with a ten microsecond flash, demonstrates the breakup of a liquid jet in a subsonic crossflow. The breakup appears to be regular and periodic. This regularity is particularly visible on the leeward side of the plume. The same orderliness can be seen in the subsonic crossflow jet in Fig. 4. Close examination of the photographs from this investigation and from Ref. 36 shows that the

fractured clumps were large enough to contain between 2 and 6 of the wave crests detectable propagating along the jet column.

Since no previous data had been reported in the literature for the frequency of jet column waves for the subsonic crossflow case considered here, the extinction setup was used to determine their frequency. The laser beam was focussed by a series of lenses onto the windward edge of the jet column just before the point of breakup. The extinction traces were examined on a memory oscilloscope. Pulses in the range of 40 to 80 kHz were observed; the average frequency of the oscillations was 61 kHz.

4.3 Injection into a Supersonic Air Stream

4.3.1 Water/Methanol

Four series of droplet size measurements were conducted for the injection of the water/methanol mixture into a supersonic air stream. The location at which each series was performed is illustrated in Fig. 23. Series #1 was performed at a single location, $x/d=24$, $z/d=12$, with exposure times ranging from 0.225 to 25 msec. The exposure time of the other series was kept between 0.2 and 0.3 msec. Series #2 scanned the plume transversely at a distance of $x/d=40$ downstream of the injector. The last two series scanned the plume horizontally at a height of $z/d=10$. The momentum flux ratio, \bar{q} , of the first three series was 12; the last was performed at $\bar{q}=4$.

The first measurement series explored the effects of exposure time on the droplet size distributions. The size distributions from

three runs at an exposure time of 25.0 msec are plotted in Fig. 24. For such a long exposure, there were no significant time variations observed, and the distribution profiles overlapped each other. The droplets can be divided into three major size groups: 30% were in the range of 7-17 microns, 48% were in the 20-35 micron bins, and 17% were larger than 40 microns. A similar situation arose at an exposure of 5.0 msec as evidenced in Fig. 25.

Figure 26 shows the results from the 2.5 msec tests. This exposure time produced the largest fluctuations in the distribution profiles for this series. Three sets of size distributions are shown. The sets were taken three seconds apart, and the distributions within each set were recorded sequentially. At some instants, only 15% of the droplets were in the 7-15 micron bin, while 53% were in the 20-35 micron group and 25% were larger than 40 microns. At the opposite extreme, 41% were in the smallest bin, while 24% and 12% were present in the 20-35 and 40-100 micron groups, respectively. In some cases, the three groups were readily identifiable (Fig. 26a), but at other times, the divisions between the groups were blurred (Fig. 26b).

The 0.65 msec tests also produced sizable fluctuations as shown in Fig. 27. None of the profiles resembled those obtained at the longest exposure times. Instead, pieces of the long exposure profiles are evident in the various 0.65 msec distributions. The profile in Fig. 27a contains the peak in the smallest bins, while Figs. 27b and 27c exhibit distribution peaks in the intermediate size group. In the 0.65 msec trials, there were sometimes less than 1% in the smallest

group while 10% were in the 40-100 micron range, and the mid-sized group contained more than two-thirds of the droplets. Other times, the 7-15 micron and the 20-35 micron group each held a third of the droplets while only 5% were larger than 40 microns. In none of the eighteen trials performed at this exposure time, were more than 10% of the droplets counted in the largest group, although the long exposure tests always determined that 17% of the droplets fell within this range.

The 0.225 msec tests in Fig. 28 revealed very little time variation in the distribution profiles. In the six tests conducted at this exposure, all of the observed fluctuations remained within $\pm 2\%$ of the mean value. In the 7-15 micron group 31% of the droplets were found, 20-35 micron group had 46%, and the 40-100 micron group had 12%. Except for the deficiency in the largest group, these profiles resembled those obtained with the 25.0 and 5.0 msec exposure times. The SMD and standard deviation for this series can be found in Table 5. The SMD hovered around a value of 19 microns over the majority of the tests; the three exceptions exhibited SMD values of 22 to 24 microns and standard deviations in excess of 0.11. The deviations for the rest of the tests ranged from 0.001 to 0.10.

The time histories of the SMD also displayed the same trend. The typical histories in Table 6 hovered around a certain diameter with only minor fluctuations. Occasionally, the SMD jumped to a high value for a relatively short time. The $x/d=12$, $z/d=6$ tests at exposure times of 0.65 and 2.5 msec demonstrated this trend best. The former

test produced a history that jumped from 15-16 microns to 25-26 microns, while the latter jumped from 17-20 microns to over 27 microns.

The second series of tests were conducted at the $x/d=40$ station while z/d varied from 8 to 24. For the $\bar{q}=12$ condition the penetration height should be about $24d$ for $x/d=40$. The data from the $z/d=8$ location was not successfully reduced owing to the possible scarcity of droplets or the presence of ligaments. All of the tests were performed with a 0.225 msec exposure. Figure 29 shows typical distributions at the $z/d=12, 20$ and 24 locations. The SMD and the corresponding standard deviation can be found in Table 7. A discernible shift in the number of droplets from the 20 to 30 micron bins to the 7 to 20 bins along with a corresponding decrease in SMD can be seen in comparing the $z/d=12$ results with the data from the other two locations. The $z/d=24$ case produced the largest fluctuations as indicated by the standard deviation results. Droplets were observed as high as $z/d=32$, but their scarcity prevented the instrument from accurately sizing them.

The last two series were conducted at z/d ranging from 8 to 12 at a $\bar{q}=4$ and 12. Exposure times varied from 0.2 to 0.3 msec. Typical distributions from the $x/d=24, 60$ and 80 locations are displayed in Fig. 30 for the high \bar{q} case. There was a gradual shift in the distributions as the jet progressed downstream. The shifts occurred between the 40-100 micron bins into the 7-20 and the 30-40 micron

groups. The largest shifts were observed in the 15-20 and the 40-50 micron bins.

The averaged SMD and standard deviation values for this series have been tabulated in Table 8. The standard deviation was observed to increase from the $x/d=12$ to 40 station and then decrease farther downstream. From high speed movies taken during the course of the Kush and Schetz investigation (46), the spray formation zone, as delineated by the presence of clumps, was seen to stretch from around $x/d=9$ to 35 for liquid jets in a supersonic crossflow. Figure 3, a short clip from a high speed movie, shows the existence of clumps in this region.

Results from the last series performed at a low \bar{q} are shown in Fig. 31 and Table 9. Between the $x/d=24$ and the $x/d=40$ profiles, the discernible shifts were from the 20-40 bins into the 7-20 micron group and from the largest bin into the 40-60 bins. Between the last two profiles, there was a general shifting of droplets from the 40+ bins into the smaller bins. The deviation decreased steadily from the $x/d=24$ station to the $x/d=40$ location and then increased slightly at $x/d=60$. Figure 32, typical of a low \bar{q} injection into a supersonic stream (from Ref. 46), shows clumps in the $x/d=7-30$ region.

Due to the properties of the liquid and/or the mechanism of the jet break up, the extinction measurements at these conditions were not very conclusive. No definite peaks were found by the frequency analyses. Figure 33 presents a typical extinction time trace and corresponding FFT for the water/methanol jet. The test was conducted

at $x/d=24$, $z/d=12$. While there are no clear peaks, there was noticeable activity up to 20 kHz, particularly between 0.1 and 6.0 kHz. No other plume location was tested.

4.3.2 Water, High \bar{q}

For this series of tests water was injected through the flat plate model into a Mach 3.0 cross stream, and the momentum flux ratio (\bar{q}) was maintained at $10 \pm 2\%$.

4.3.2.1 Droplet Sizes

Droplet size measurements were made at the locations outlined in Fig. 34. In that figure, the SMD of the spray is shown as a function of location and exposure time, and the corresponding non-dimensionalized standard deviation is included enclosed by parenthesis.

At two locations the droplet size measurements are suspect. Based on observations made by Nejad and Schetz (48), the data at the $x/d=10$ to 12 stations are suspect, since the spray may not have fully atomized, and the droplets and clumps may not all have a circular cross section. The diameters calculated may reflect the size of droplets sheared off the windward surface of the jet column; these droplets may surround the jet core. The SMD figures agree well with those of Nejad and Schetz (48) for the stations $x/d=20$ to 60. Nejad and Schetz determined that the SMD dropped to 15-16 microns at $x/d=100$. Since the present system cannot accurately measure such a

well atomized spray, the SMD values presented at the $x/d=100$ and 160 stations are suspect. The standard deviation values derived at these locations should have some validity nevertheless since these values reflect the intensity of the fluctuations observed in the diffraction pattern.

At each x/d location for each exposure time, the largest recorded mean diameters occurred near the center of the plume. For $x/d < 100$ the largest standard deviations also occurred near the center. Measurements were not performed near the upper boundary of the plume, since the plume was extremely unsteady in the upper regions. Very often there was little or no spray in these regions which led the instruments to produce erratic results. The heights to which measurements could be successfully made in the plume at the $x/d=20, 30$ and 100 stations corresponded to the penetration heights reported by previous investigators who conducted photographic and mean droplet sizing surveys.

In the x/d direction, there are no recognizable trends in the SMD. The results suggest that the spray was well atomized even at the upstream stations. The trend in the standard deviation was that it increased between $x/d=10$ to 40 and then decreased at distances farther downstream. These trends are only noticeable when comparing data taken at the same exposure time. The deviation in the 25 msec trials was surprisingly not negligible; at such a long exposure time the transients in the spray are usually averaged out.

The time history of SMD at various plume locations is listed in Table 10. The mean diameters fluctuated over a considerable range. Of particular interest are the SMD histories at the following locations:

1) $x/d=10$, $z/d=6$

In the 0.11 msec history, the value of the SMD in microns fluctuated in the upper teens and occasionally peaked in the mid-twenties. In the 2.7 msec history, the SMD hovered around a mean value of 19.6 except for a single measurement at 26.2 microns.

2) $x/d=20$, $z/d=8$

In the 0.11 msec series, outside of the 20.1 micron reading, the SMD fluctuated about a mean of 16.2. The 2.7 msec history fluctuated between the same extremes.

3) $x/d=40$, $z/d=10$

Both histories varied between values of 16 and 27 microns. The values in the 2.7 msec tests tended to be found closer to the extremes than the values in the 0.11 msec trials.

In general, the 2.7 msec histories varied dramatically between the two extremes; the SMD was most often found near the smaller extreme. The values of SMD in the 0.11 msec histories fell between the same extremes, but the values fluctuated slower and more gradually. Therefore, the period of the SMD fluctuation must have been between 0.11 and 2.7 msec.

Distributions at three x/d stations taken at $z/d=10$ with a 2.7 msec exposure are plotted in Fig. 35. The atomization process can be identified in the figure. The smallest bins become gradually filled with increasing x/d with each of the first two bins growing by 10%. The process has been labelled as being gradual, since in the 7-15 micron bin, none of the $x/d=30$ trials produced a volumetric fraction greater than 0.3, while one did at $x/d=40$ and two did at $x/d=60$. Meanwhile, there was a definite emptying of the larger bins between $x/d=40$ and 60. The $x/d=40$ and 60 tests also produced larger fluctuations in the distributions than those at $x/d=30$.

Figure 36 shows the distributions at four z/d heights taken at $x/d=30$ with a 2.7 msec exposure. These distributions can be compared with the $x/d=30$, $z/d=10$ distributions presented in the previous figure. The distributions for $z/d \geq 14$ exhibited more small droplets. This trend was most evident in the 15-20 micron bin. Also, the populations of the 20-30 micron bins dropped by half between the lower heights and the higher ones. At the other extreme, the larger droplets tended to populate the $z/d=6$ and 10 locations. This trend was best shown by the 50-60 micron bin where the volumetric fraction fell from an average of 0.06 to 0.02 between the two lower locations and the three higher ones. These overall trends were partially obscured by the fluctuations present in the distributions. The existence of these fluctuations indicate that there were some jet phenomena occurring with periods close to the 2.7 msec exposure time. The measurements made at $z/d=6$, however, showed a surprisingly little

amount of fluctuation; the standard deviation for the series of three data sets taken at this location was only 0.008.

Four distributions taken at an exposure time of 0.11 msec are plotted in Fig. 37. The $x/d=30$, $z/d=14$ location exhibited an extremely large deviation, the non-dimensionalized standard deviation reaching 0.27 in one series of tests. The mean diameters for the two plotted distributions were 33.7 and 19.3 microns. For bins less than 30 microns, the 19.3 micron SMD distribution exhibited larger volumetric fractions and vice versa for the larger diameter bins. This was in contrast to the other distribution profiles in this and the two previous figures. In the other distributions, the "crossover" between small SMD and large SMD profiles occurred around 15-20 microns.

To quantify the shifting of droplets among the various bins, the populations of three major size groups were tabulated. The groups were 7-20, 20-60 and 60-100 microns. The volumetric fraction of droplets in these groups for various locations are listed in Table 11. The distributions listed for the shorter exposure times represent the spray at the extreme values of SMD observed. Several general observations can be made about the distribution of droplets among these three groups. The shorter exposure trials (2.7 msec and less) generally found the spray in a well atomized state for $x/d < 100$ as evidenced by the population in the 7-20 micron group. It should be stressed that the two tabulated states were not equally probable; the SMD of the spray was usually small. Between $x/d=10$ and 40 the gradual

atomization of the spray with increasing x/d was evident in the shifting of droplets from the larger bins to the smallest group. Beyond $x/d=40$, the populations in the various groups tended to fluctuate randomly until the $x/d=100$ station. The population of the smallest group dropped between the $x/d=60$ and 100 stations; perhaps the droplets that had been in the 7-20 micron group were atomized to droplets below the 7 micron limit of the droplet sizing instrument. A substantial number of droplets below 7 microns also would explain why the SMD did not drop to the levels reported by Nejad and Schetz at the $x/d=100$ station.

4.3.2.2 Extinction Measurements

The time variation of the laser beam extinction at $x/d=40$, $z/d=10$ has been traced in Fig. 38. An FFT performed on the signal, Fig. 38b, revealed that the main oscillations occurred at frequencies of less than 12 kHz, although some activity can be noted extending as high as 65 kHz. The vast majority of FFT data recorded at this flow condition were performed in the 0-25 kHz range as illustrated by the FFT in Fig. 38c. A number of FFTs were performed also at lower frequency ranges. The observed oscillations died off gradually with decreasing frequency. Due to 60 Hz noise in the system, the frequency analysis was not able to probe below 100 Hz. At 100 Hz there was still observable activity in the extinction traces, but the amplitude of that activity was drastically less than that observed in the kHz

range. The sharp peak at the left margin of some of the FFTs was apparently caused by an anomaly in the FFT software package.

Fast Fourier Transforms performed at $x/d=5$, $z/d=5$ and $x/d=10$, $z/d=15$ are plotted in Fig. 39. Of note is the lack of high frequency oscillations at the $x/d=5$, $z/d=5$ location, Figure 39a, although the frequency curve resembles that found at the the other location for frequencies of less than 1 kHz.

Figure 40 presents two FFTs performed at $x/d=100$. There was more activity at higher frequencies at the $z/d=40$ location than at the lower one. The penetration height was about $46d$ at this downstream station.

The frequency at which the FFTs reached its maximum amplitude for each of the thirty runs was determined, although the precise location of the peak was often difficult to determine. Overall, the peak frequency ranged from 1 to 8 kHz; the mean was 4.5 kHz. The peak frequency consistently dropped with increasing z/d . At $x/d=40$, this relationship was extremely noticeable as the peak frequency dropped steadily from 7 to 5 to 4.5 to 3 kHz at heights of $z/d=10$, 20, 24, and 28 respectively. Another vertical survey at $x/d=100$ revealed that the peak frequency fell from 3 to 1 kHz between $z/d=10$ and 40. At $x/d=100$, the peak frequency did not appear to vary with z/d in any recognizable pattern. Contrary to the pattern, the $z/d=5$ results usually revealed activity at very high frequencies; the frequency profiles resembled those recorded along the jet boundary. The highest frequencies (6-8 kHz) were observed at the $x/d=20$ and 30 stations and

at the $x/d=40$, $x/d=10$ location. Locations upstream of $x/d=20$ and locations downstream or above the $x/d=40$, $x/d=10$ spot had peak frequencies of less than 5 kHz.

The highest frequency at which a significant amount of activity was observed was noted also for each run. At each x/d station, the z/d location that yielded the highest frequency activity was noted; the z/d locations and the corresponding frequency are tabulated in Table 12. Several trends can be observed in this table. First, as the spray progressed downstream, there was continually less activity at the higher frequencies. Second, at all of the tested x/d stations, the highest frequency activity was found at a height that was approximately 80% of the plume penetration height. Except for the $x/d=100$ station, the largest amplitudes in the extinction signal for each x/d station was found at a height of $0.4h$. At the $x/d=100$ station, the largest amplitude was found at $z/d=16$.

Table 13 lists the z/d locations at which the maximum SMD deviations were noted at each x/d station. The maximum deviations, on the average, occurred slightly below the midpoint of the plume.

In Table 14, the rms value of the extinction signal at each location is given. this value corresponds to the transmission of the laser beam through the spray. The number is given as a percentage of the original laser beam intensity. A value of 99-100% indicates that there was no spray at that location. Consequently, the $x/d=40$, $z/d=26$ and the $x/d=100$, $z/d=40$ locations must have lay on the jet boundary.

The minimum readings, which may indicate the locations of maximum liquid mass flow, occurred between $z/d=10$ and 20 for $x/d \geq 20$.

4.3.2.3 Photographic Results

Figures 41 and 42 show a schematic of the cross section of the jet plume and a photograph of the plume taken at $x/d=100$. The photograph was taken with a one second shutter speed. The illuminating sheet of light can be discerned crossing the test section horizontally; the relatively light bars at either end of the sheet was created by the light diffusing through the test section windows. In the middle of the photograph, the circular cross section of the spray plume and the relatively flat liquid layer below the plume are readily identifiable. The reflections of the plume cross section also are visible (below the plume, on the surface of the flat plate). Vortices attached to the rear corners of the flat plate reflected some light. In the photograph, one of the vortices can be seen to the right of the liquid layer, it appears as two small discs. The vortices flashed during the wind tunnel runs, alternating between the upper and lower edge of the corners. The frequency of the flashing was of the order of 10 Hz.

The dimensions of the plume and liquid layer were measured from the photographs, and they are listed in Table 15. The $x/d=200$ station was located downstream of the aft edge of the flat plate. Beyond the flat plate, the liquid layer spread out into a double wing formation as will be shown in a later section. The penetration heights and

plume widths were substantially larger than those found by Nejad and Schetz (49) and by Kush and Schetz (46) for a similar jet using a conventional back lighted streak photographic method.

4.3.2.4 CCD Penetration Results

To circumvent the failures of traditional streak photography to measure plume dimensions and to obtain the time variation of the dimensions, the CCD was used as a video camera scanning the height of the plume. The CCD measured the intensity of light passing through a linear array of plume locations yielding not only plume dimensions but also information on the density of the plume (liquid mass flow). Figure 43 compares the result of a CCD penetration test with the results of a photomultiplier/extinction survey. The results of the latter were found to compare favorably with the data from a previous mass sampling survey (Ref. 39). Figure 43 was taken at $x/d=40$. The CCD results, the solid line, accurately measured the height of the plume shock (point D). Due to refraction of the light, the shock appears as a dark spot on the CCD trace. The location of maximum liquid mass flow (Point B), the penetration height (Point C) and the height of the liquid layer (Point A) were not well predicted; neither was the general shape of the curve. The dashed line and accented letters show the results of the photomultiplier survey and the photographic survey. This figure represents the closest agreement between the CCD penetration results with the other measurements. In

all cases, the liquid layer was overestimated and the main plume curve shifted to lower z/d by the CCD.

The principle difference between the extinction setup and the CCD setup was the size of the illuminating beam. The extinction measurements were made with a laser beam passing through a narrow cylindrical volume of the plume. For the CCD, the beam from the lamp was expanded such that it illuminated the entire plume. The CCD apparently detected not only the light which had passed through the plume directly in front of the detector but also light that had passed through other regions of the plume and then had been diffracted onto the CCD. Diffraction effects can readily explain the results depicted in Fig. 43. It is known that small droplets populate the jet boundary while larger droplets inhabit the central core of the plume. Small droplets diffract relatively little light and diffract that light through large angles. Larger droplets diffract more light but do so through relatively small angles. Consequently, these effects would lead the CCD and traditional photography to underestimate the extent of the plume and the location of maximum liquid flow (where the largest drops are presumably found). The liquid layer, meanwhile, apparently refracts the light or aids in the reflection of light off the brass flat plate model. The light passing through the liquid layer is angled upward leading to a gross overestimation of the layer.

The extinction measurements avoided these difficulties by illuminating only a small portion of the plume, the cylindrical volume under investigation. Cross sectional photographs also avoided the

problem by measuring the intensity of light reflecting off, and not passing through, droplets in the spray.

4.3.3 Water, Low \bar{q}

For the final flow case examined, water was injected with a momentum flux ratio of $\bar{q}=4 \pm 2\%$.

4.3.3.1 Droplet Sizes

Figure 44 shows the locations tested in the droplet sizing survey. The SMD and the standard deviation are shown at each plume location as a function of exposure time. Comparisons with SMD found by Nejad and Schetz (48) usually were in good agreement with one deficiency. Examining the 25 msec results which should match the time-averaged values obtained by Najad and Schetz, the present system slightly underestimated SMD from $x/d=10$ to 30 and slightly overpredicted it at $x/d=100$. The small deviations may be explained by the manner in which the mean diameter was calculated in the present work. In the calculations, each bin was represented by the mean of the diameters defining the bin. This arrangement ignored shifts in the droplet distributions within each bin. Since the 7-15 micron bin often had nearly half the volume of droplets, the observed errors could be attributed to shifts within this single bin. Nevertheless, the decrease in SMD with increasing x/d was clearly evident from $x/d=20$ to 100. The first two x/d stations were in the region of small beam transmission; consequently, the calculated droplet sizes are of

dubious validity. Furthermore, it is not known whether or not the droplets have a spherical cross section so near to the injector; the spray may consist of non-spherical clumps at these locations.

The largest standard deviations occurred at longer exposure times than they had for the high \bar{q} case. The 2.1 msec exposure trials resulted in the most frequent large deviations. Unexpectedly large deviations were recorded for the 25 msec trials.

Examining the effect of increasing x/d on the standard deviation, the results from the 2.1 msec series were inconclusive, since the deviation seemed to fluctuate randomly. There was also a good deal of randomness in the 25 msec trials, although there was a slight trend towards a decrease with increasing x/d along the higher measurement heights. The shorter exposure cases showed a definite trend. For $x/d=5$ to 20, the deviation ranged from 0.067 to 0.219, at $x/d=30$, the deviation ranged from 0.004 to 0.204, and for $x/d \geq 40$, the deviation dropped to 0.003 at $x/d=100$.

The time history of the SMD at various locations given in Table 16 documents the fluctuations in the jet plume. First, examining the histories taken at the 0.11 msec trials, the SMD can be seen fluctuating slightly around an average of 17-18 microns. The 0.35 msec data can be classified into "states" according to the degree of atomization. A "low state" corresponds to a diameter of approximately 18-19 microns while a "high state" is represented by SMDs in the mid-twenties. The 25 msec tests showed a good deal of variation, but the extremes in SMD never matched those of the shorter exposure trials.

The $x/d=30$, $z/d=6$ test at 0.11 msec was interesting, since it showed the degree of atomization in steps. The SMD varied between 16 and 22 microns as in the 0.35 msec tests, but the SMD was nearly constant between sequential readings. The inference to be made is that the SMD fluctuated with a period of several milliseconds, but that the atomization of the jet was most often in a "low state."

The minimum and maximum values of the SMD recorded at the 0.11 msec exposure time both decreased with increasing x/d . In Table 17 the minimum SMD is seen to decrease slightly while the maximum SMD decreased by 20% between the $x/d=10$ and 60 stations.

Figure 45 contains one distribution from each set of the 0.11 msec tests performed at $x/d=20$, $z/d=6$. The largest fluctuations were in the 7-35 micron size groups and significant variations occurred in the 40-60 micron ranges. The SMDs for the three distributions were 22, 18 and 15 microns respectively.

The plots in Fig. 46 demonstrate how the distributions varied with increasing x/d . The depicted distributions were typical of the profiles at those locations at the 0.35 msec exposure, and except for the $x/d=30$ profiles, they were taken sequentially. Since the SMD varied dramatically between the various sets taken at $x/d=30$, two profiles from different sets were plotted. The significant trends were:

- 1) A steady increase in the population of the 7-15 micron bin at each successive x/d station
- 2) A steady decrease in the 20-30 micron bins for $x/d=30$ to 50

- 3) Large decreases in the 40-50 micron bin between $x/d=40$ and 50 and in the largest bin between $x/d=30$ and 40.

The other bins seemed to follow no recognizable pattern beside the usual random fluctuations.

The same downstream variation was evident also in the extreme distributions of the three major size groups in Table 18. As x/d increased, at least one of the extreme populations in the 7-20 micron group increased while at least one of the 20-60 micron group decreased. The difference between the extreme populations of the two smaller groups was dramatic at small x/d and gradually decreased with increasing x/d in the 0.35 msec trials. The opposite trend can be observed in the 2.1 msec tests. Meanwhile, the population of the largest group seemed to experience only random fluctuations.

The vertical variations, at the $x/d=30$ station, did not show a consistent pattern. In the numerous samples taken, there was a tendency for an increase in the population of the smallest bin and a decrease in the largest bin with increasing z/d . Two examples are given in Fig. 47.

4.3.3.2 Extinction Measurements

Figure 48 contains typical FFTs of the extinction signal. High frequency activity, higher than 10 kHz, was observed in the extinction measurements made close to the injector and close to the jet boundary at the $x/d=100$ station, as in Fig. 48a. At these locations, significant oscillations were noted up to 20 kHz. The $x/d=100$, $z/d=5$

and 10 locations (Fig. 48b) showed no activity above 7 kHz; the main activity registered was below 4 kHz.

Along the jet boundary, the FFTs peaked around 6 kHz. The $x/d=40$ to 100 stations, below z/d of 15, had peaks around 3 kHz. The locations tested are listed in Table 19 which also lists the rms value of the extinction. The locations $x/d=40$, $z/d=20$ and $x/d=100$, $z/d=22$ apparently fell along the edge of the jet.

The z/d at which the highest frequencies were found and the z/d where the largest SMD deviations were found are presented in Tables 20 and 21, respectively. The maximum frequencies occurred on the average at a height corresponding to seven tenths of the penetration height. The maximum standard deviations were found at an average height of $0.4h$. Due to the low physical penetration of the low \bar{q} jet, relatively few locations could be tested along the z axis, hence these results have considerable uncertainty.

At the $x/d=40$ and 100 stations, the largest attenuation of the laser beam and the largest amplitudes in the extinction signal were noted at $z/d=5$ to 10.

4.3.3.3 Photographic Results

Figure 49 presents a cross sectional photograph of the spray plume at $x/d=200$. The photograph was taken from a position to the port of the flat plate; the air flow is from the left to the right on the photograph. The illuminating sheet of light passed downstream of the aft edge of the flat plate. The plume still has a circular cross

section (part of its reflection can be seen on the flat plate "below" the liquid layer) while the liquid layer has split. Part of the liquid layer continued on as if the plate was still below it while the majority of the liquid from the liquid layer had mixed with the air flow passing beneath the plate. Consequently, at this downstream station, the cross section of the liquid layer has a double wing appearance.

From the series of photographs taken at various x/d stations, the dimensions of the plume were determined and tabulated in Table 22. The plume cross section was basically circular, but slight elongated in the transverse direction. The liquid layer was somewhat thicker than its high \bar{q} counterpart at most x/d stations. At $x/d=10$, the penetration height matched that reported by Nejad and Schetz (49), but with increasing x/d , the heights listed in Table 22 grew at a more accelerated rate than those reported in Ref. 49. By $x/d=200$, the penetration height, as measured from the cross sectional photographs, was double that obtained by the traditional streak photography method.

V. DISCUSSION

5.1 Physical Interpretation of the Observed Fluctuations in the Droplet Sizes

At each location and flow condition tested, the droplets fluctuated between two extreme size distributions. The droplets were usually small but, periodically, the droplet size distribution would be perturbed briefly to a state of large SMD. This section will examine the evidence for such an interpretation of the fluctuations.

The clearest evidence was produced by the time histories for jets in a supersonic crossflow. In all of the short exposure tests (exposure time ≤ 0.35 msec) performed for the three cases, the SMD was found to be large 10 to 15% of the time. As the exposure time was increased, the probability that the spray would be caught in a high state (large SMD) increased. For the water/methanol jet with exposure time of 0.225, 0.65 and 2.5 msec, the SMD was large in 11%, 16% and 23% of the tests, respectively. For the high \bar{q} water tests, the SMD was large in 16% of the tests at 0.11 msec. When the exposure time was increased to 2.7 msec, this fraction increased to nearly 50%.

An estimation of the percentage of the time that the droplets were large can be made by a simple analysis. If the fluctuations are assumed to follow a square pulse variation of pulse width S and period P and if the exposure time is a multiple of S , namely $c \cdot S$, then the probability that the exposure will catch a part of the pulse is simply $(2 \cdot c + 1)/(S/P)$. The probability that the exposure will catch an

entire pulse is $(2 \cdot c - 1)/(S/P)$ assuming that the exposure time is less than P . From these relations the values of S and P can be estimated from data presented in the preceding paragraph. Assuming that the probability was $(2 \cdot c + 1)/(S/P)$, then the ratio of S/P was 0.11 for the high \bar{q} jets in a supersonic crossflow. Physically, this figure would mean that the SMD was large 11% of the time. For the various jets, the ratio ranged from 0.08 to 0.14. Alternatively, using the $(2 \cdot c - 1)/(S/P)$ model, the S/P ratio should be in the neighborhood of 0.2. In actuality, the SMD probably did not vary as a true square pulse. The two models, however, should form a pair of limits for the actual ratio.

The low \bar{q} water case also produced the small/large variations in SMD as noted for the high \bar{q} cases. The frequency of the fluctuations, as estimated in the following section, was the lowest of all the cases studied. The 0.11 msec tests, as a consequence, rarely found the spray to be in a high state. The 0.35 msec tests found a large SMD spray 33% of the time. The preceding analysis could not be performed on this data due to the lack of a statistically large number of samples.

The injection into a subsonic crossflow did not show this trend in the time histories. Due to the relatively high frequency of the fluctuations, even the shortest exposure times were several periods long.

The pulse-like nature of the droplet size perturbations also can be seen in the droplet size distribution data. The water/methanol results demonstrated this phenomenon well. The 25.0 and the 5.0 msec distributions at $x/d=24$, $z/d=12$ always indicated that 17% of the droplets were in the 40+ micron group. The shorter exposure trials rarely showed more than 10 or 12% in this group. Apparently the 0.225 msec distributions are representative of the condition of the spray for most of the time. The disturbances to which the spray was subjected to (indicated by the 2.5 and the 0.65 msec distributions) were caused, at least in part, by the relatively brief passage of large droplets. The longer exposures always caught several of these passages, thus explaining the abundance of 40+ micron droplets in the 5 and 25 msec distributions. The trend was obscured in the water tests in the supersonic flow by relatively low frequency jet oscillations. An explanation of the existence of these long period fluctuations will be presented in a later section.

Given the time history of the variations in SMD, the physical interpretation is obvious. When the main jet column fractures, a clump of liquid is dispersed downstream. The clump is broken into an ensemble of droplets by aerodynamic forces. These droplets are larger than those produced by the shearing of liquid off the sides of the plume due to the relative velocities between the liquid and the air. The passage of the clumps of large droplets creates the transient disturbances observed in the droplet size distributions. In the high speed movies from Ref. 46, it was found that a liquid jet in a

supersonic crossflow will fracture periodically with a notable time lag between successive fractures. The subsequent passage of the resulting ensemble of droplets through the plume also was evident in the movies.

5.2 Frequency of the Observed Fluctuations in the Droplet Sizes

5.2.1 Supersonic Crossflow

For the water/methanol jet, the period of oscillation in SMD was longer than the span of the successive 0.225 msec measurements, since some of the sets of time histories did not catch the spray in a perturbed state. Each set of these exposures spanned 0.45 msec; each set consisted of two exposures. For an opposite limit, the period must have been less than 5 msec, since the fluctuations appeared to have been partially time-averaged within that exposure time. Increasing the exposure time to 25 msec produced a very stable distribution. Presumably that exposure time was at least an order of magnitude larger than the fluctuation period.

Based on the above arguments, the fluctuation period must have been between 0.45 and 2.5 msec. Two tested exposure times lay in this regime. The 2.5 msec tests produced distributions which varied strongly without any recognizable pattern. These distributions must have been taken with an exposure time close to that of the fluctuation period. The 0.65 msec tests caught the jet during the course of these variations. The fluctuation frequency, therefore, must have been in the 0.5 to 1.0 kHz range. These figures tally with the FFT tests

which found the most activity in the 0.1 to 6.0 kHz range. The square pulse analysis produced frequencies of about 0.15 to 0.4 kHz for the $(2 \cdot c + 1)$ model and around 0.9 to 1.2 kHz for the $(2 \cdot c - 1)$ model. All three methods agree that the frequency was probably slightly less than 1 kHz. This agreement suggests that the laser beam extinction tests were sensitive to the passage of the ensemble of large droplets, which seems reasonable since the extinction depends on the diffraction and absorption of droplets passing through the beam.

The water injection cases underwent oscillations of two different frequencies. Besides the disturbances that were found in the water/methanol case, there was a lower frequency fluctuation that influenced the 25 msec results. This low frequency oscillation was very aperiodic as shown by the large variations in the standard deviation for the 25 msec trials. The frequency of this disturbance apparently changed significantly in time. If the frequency had been fairly constant, then it should have shown up as a peak on the FFTs instead of as a gentle slope that decays with decreasing frequency. The higher frequency fluctuations, on the other hand, can be defined more rigorously.

For the high \bar{q} water case, sometimes no perturbations were observed during the 0.22 msec span of the 0.11 msec trials. At the same time, however, the standard deviation in SMD at the 0.11 msec exposure time were consistent larger than those at 2.7 msec and were usually slightly larger than those taken at 0.35 msec. These observations place the period of oscillation between 0.22 and 2.7

msec; the period was probably closer to 0.22 msec than to 2.7 msec. The square pulse model yielded periods ranging from 0.19 to 0.7 msec. A period of 0.19 msec is equivalent to a frequency of 5 kHz and a 0.7 period to 1.4 kHz. The extinction tests produced frequency profiles that peaked between 1 and 8 kHz with a mean value of 4.5 kHz. Again, there was good agreement between the frequency as obtained from the SMD histories and the FFT results. Based on the above evidence, the best estimate for the perturbation frequency would be about 4 kHz. The FFT profiles suggest that there was some variation in time of the perturbation frequency.

According to the standard deviation measurements, the low \tilde{q} jet fluctuated at a lower frequency. The 0.35 and the 2.1 msec tests produced the largest deviations. Some of the 0.35 msec tests and many in the 0.11 msec series caught the jet in a low state throughout the span of two successive measurements. The FFTs in main jet core extended out to 3 kHz. Apparently, the frequency of the fluctuations was around 1 kHz.

5.2.2 Subsonic Crossflow

Injection into a subsonic crossflow produces a jet which behaves substantially differently from jet injection into a supersonic crossflow. The extinction measurements provide a good indication of the different behavior. The FFTs in the case of a supersonic crossflow showed activity extending from below 100 Hz to a few kHz. In the subsonic crossflow case, the frequency profile often assumed

the shape of a Gaussian profile which extended to much higher frequencies.

The extinction setup did not always detect the frequency of jet fracture as it had for the supersonic crossflow injections. At some locations the frequency curve was centered around 60 kHz. This frequency corresponds to the frequency of waves on the jet column. Photographs taken during the present investigation and from Ref. 36 show that the jet fractured in clumps several wavelengths long which necessitates that the fracture frequency be several times less than that of the column waves. Apparently, the extinction setup was able to detect the effects of wave formation on the jet column in the droplets in the spray. The mechanism of jet breakup in a subsonic crossflow must not smear or otherwise disguise the influence of waves as it does in a supersonic crossflow.

The time histories of even the shortest exposure time (0.35 msec) did not show the dramatic large/small SMD variations evident in the case of a supersonic crossflow. The period of the fluctuations were shorter than 0.35 msec. Based on the value of the standard deviation at this exposure time, the fluctuation period could not have been much less than the exposure time. The FFTs performed close to the injector and to the flat plate showed activity out to about 20 kHz. A small peak at 15 kHz is observable in Fig. 18. The effect of the waves would not be expected to be of a significant magnitude at these locations. These FFTs should be reflective of the breakup frequency. At other locations, the extinction traces revealed a pattern composed

of four pulses. The pulses, by a previous argument, correspond to wave phenomena, so the train of four pulses might represent a clump that has fractured off the jet column. The average frequency of the pattern was determined to be 15 kHz. Since waves on the jet column had an average frequency of 61 kHz, a train of four waves would have an effective frequency of 15 kHz. The inference is obvious. The jet fractured on the average at every fourth jet column waves leading to a fracture frequency of 15 kHz. The extinction measurements made along the main jet core were sensitive to the breakup phenomena, while measurements made at other locations detected the effect of the wave phenomena on the spray.

The photographs taken at this crossflow condition show that the size of the fractured clump was large enough to contain between 2 and 6 column waves. It was difficult to accurately gauge the dimensions of the clump, hence the uncertainty in the above figure. The average number of wavelengths per clump was four, thus supporting the assertion made in the preceding paragraph.

5.2.3 Jet Whipping

In the surveys for water injection into a supersonic crossflow, the FFTs produced frequency profiles which were dependent on plume location. An analogy can be made with the subsonic crossflow results. The locations that produced frequencies closest to the breakup frequency were the locations of maximum liquid mass as determined by the rms value of the extinction. The main fragments of the clumps

passed through these locations, hence the observed extinction frequency was that of the jet breakup. Toward the upper boundary of the jet, the FFTs produced frequencies approximately double those found at the lower locations. At these sites, the clumps have been further broken down by the effects of the crossflow, thus increasing the observed frequencies. There is also a slightly different interpretation of these results. In Ref. 46, relatively long wavelength disturbances were observed on the high \bar{q} water jets. These waves had a large amplitude and seemed to have been formed from several smaller waves. The extinction measurements may have detected the influence of these aerodynamically-induced waves on the spray in a similar fashion as the extinction had detected the effects of the regular jet column waves on the jet in a subsonic crossflow. Regardless of which interpretation is considered, the aerodynamic forces acting on the plume creates a noticeable fluctuation in the droplet sizes at a frequency several times that of fracture.

As the clumps accelerate downstream, their velocity must approach that of the air flow. The frequency of the clump passage at a given location cannot decrease, since this frequency must be at least that of fracture. Due to the breakup of the clumps, the observed clump frequency might increase, but there was no evidence of this at locations distant from the jet boundary. The droplets within the clumps might accelerate at different rates depending on the droplet inertia and due to gradients in the gas velocity in the plume wake. If the droplets accelerate at different rates, the clumps would have

spread out with the faster droplets preceding the slower ones. The increased length of the clumps would make the detection of the clumps at a given location more probable. The evidence for the effects of clump spreading was partly obscured by the effects of "jet whipping" as delineated in the following discussion.

Kush and Schetz (46) commented on the violent whipping of the jet associated with the fracturing process. The whipping would tend to distribute the liquid unevenly within the plume. At times, a substantial portion of the liquid would be "tossed" toward the upper jet boundary, and at other times, the liquid flow would be directed toward lower z/d . The effects of fracture would be observable at all plume locations, but the amplitude of the effects would not be uniformly spatially distributed. At some plume locations during certain times, the passage of a number of clumps may be easily detectable, while at other locations, the perturbations to the droplet size distributions may be small. The key point to this conjecture is the element of time. The postulation is that superimposed over the temporal transients induced by jet fracture there might be a spatially dependent transient of a longer period created by whipping of the jet.

The above model was conjectured from the results indicated in Table 18. That table lists the extreme distributions observed at various x/d stations for the low \bar{q} water case in a supersonic crossflow at two different exposure times - 0.35 and 2.1 msec. At small x/d , the 0.35 msec tests detected the spray to be in either a well atomized state (with a large 7-20 micron group population) or a

"clump" condition with a small 7-20 micron group population and a large 20-60 micron population. With increasing x/d , the dissimilarity between the extreme distributions decreased, i.e. the jet was usually found to be well atomized at large x/d . The 2.1 msec series followed the opposite trend. At small x/d , the extreme distributions were similar to one another. The effects of the time-averaging of several cycles were clearly evident, since the group populations were roughly the average of the two distributions at the corresponding 0.35 msec tests. With increasing x/d , the 2.1 msec distributions grew farther apart. The $x/d=100$ results resembled those found by the shorter exposure at $x/d=10$.

Two simple explanations can be put forward for the above phenomena - a decrease in the observed frequency and/or a decrease in the chances that a short exposure test would delete a clump. Without taking into account the whipping of the jet, neither explanation seemed physically possible. The frequency could not have decreased nor could have the probability of catching a clump have decreased just for the 0.35 msec exposure time. The whipping of the jet should not influence the data taken near the injector, nor did it appear to. The 0.35 msec tests caught the jet in either of the two states and the 2.1 msec exposures time-averaged out the fluctuations. At large values of x/d , the whipping may superimpose a relatively low frequency fluctuation on the transients observed at a given plume location, since the clumps may pass through or bypass a given location depending on the whipping of the jet. Consequently, for a given plume location

at a large x/d , the probability that a short exposure measurement will detect a clump passage is decreased. On the other hand, if the exposure time was approximately the period of the "whipping", then large deviations would be measured in the droplet size distributions. The effects of the whipping would thus disguise any effects of the spatial and temporal spreading of the clumps (as previously discussed) which would increase the chances that an arbitrary exposure would detect a clump passage. The jet whips at relatively high frequencies, at least as high as the fracture frequency. This discussion has postulated that the whipping follows a distinct pattern whose fluctuation period is of the order of several milliseconds. Without simultaneous measurements made at several z/d locations, this explanation can only be a conjecture.

The same trend can be observed in Table 11 for the high \bar{q} condition, but to a lesser extent. The trend was most noticeable in the 0.11 and 2.7 msec tests conducted from $x/d=10$ to 60. The $x/d=100$ entries did not follow the pattern. Presumably, the 7 micron limitation of the sizing instrument obscured the pattern at this station.

The jet whipping phenomenon may explain the low frequency oscillations noted in the droplet size distributions for the case of water injection into a supersonic crossflow. These oscillations perturbed the size distributions even at an exposure time of 25 msec. The frequency of the whipping pattern is of the right order of magnitude and it would be expected that the whipping would cause

fluctuations whose period could vary over a large range, which is another characteristic of the previously discussed fluctuations.

5.3 Development of the Jet Model

In order to identify the processes in the transient behavior of the jet, a simple model was inferred from available data. In this section empirical equations will be developed. The equations will not be rigorously defined or proven; they are not meant to be exact relations. The goal of this discussion and of the equations will be to conjecture what physical phenomena caused the fluctuations and the droplet distributions observed in this study.

The main component of the droplet size transients has already been identified with jet break up. Any discussion of break up must first be concerned with the waves on the jet column, since the jet fractures at the troughs created by these waves. In previous investigations the wave frequency was never measured directly as it was for the subsonic injection in the present study. In fact, previous investigators (Refs. 47 and 49) never calculated frequencies, only the wave speeds and wavelengths were measured and presented. Calculating frequency from wave speeds and wavelengths incurred several errors. Rarely were the speed and wavelength measured for a single wave. Usually, the speeds and wavelengths were obtained from different series of photographs. Furthermore, a statistical number of samples was never available for a given condition, and the samples that were given varied considerably. In other words, the calculated

frequencies were subject to significant error and at best could only reflect general trends.

Kush and Schetz (46) presented wave speed and wavelength data as a function of distance along the windward surface of the jet column. An examination of a hundred of these samples suggested that while the wave speed and wavelength both increased in magnitude along the jet column, the frequency remained constant. The frequencies calculated from the data in this reference were averaged along the jet column. Nejad and Schetz (48) tabulated only the average value of wave speed and wavelength along the jet column; they presented their data as a function of \bar{q} . They later concluded that the wave properties were independent of \bar{q} . The results of Kush and Schetz suggested that there was a weak influence of \bar{q} on wave frequency, but this influence was camouflaged by a significant amount of scatter in the Nejad and Schetz data. Despite this influence, the data from Ref. 48, which was obtained over a wide range of \bar{q} ($\bar{q}=1$ to 20), was averaged and will be presented as being the frequency at an average value of \bar{q} . The averaging was required in order to average out the random data scatter. The data was averaged within regimes, within small ranges of \bar{q} , whenever it was apparent that the frequency changed dramatically with \bar{q} .

The data from the Nejad and Schetz (48) report indicated that the viscosity and surface tension of the injected liquid exerted definite

influences on the wave properties. Increasing the viscosity decreased the wave speed, and decreasing the surface tension had a slight but observable positive influence on the wavelength. Within moderate ranges, the viscosity did not affect wavelengths nor did the surface tension influence the wave speed.

The frequencies of waves on the jet column from the present and previous studies are presented in Table 23. For each listing, the jet and crossflow conditions have been tabulated. To develop an equation to relate the wave frequency to the jet parameters, the following variables were used initially: the orifice diameter, the surface tension, the viscosity, and the velocity of the air striking the initial jet column (U_1). The latter was approximated by the free stream velocity for the subsonic case and by the velocity after a normal shock for the supersonic case. For the supersonic flow, this velocity seemed more relevant than either the free stream Mach number or the air velocity in front of the shock. Since the waves had been postulated to be at least partially aerodynamically induced, the velocity of the air striking the column seemed to be of the greatest importance. The velocity after a normal shock was considered to be a very good approximation to this since the shock does appear normal (but it is curved in the lateral direction) to the initial jet column. Other parameters were not considered initially, because either the parameter had been varied only slightly among the tests or its influence appeared relatively weak. Due to the uncertainties involved in the wave frequency, it was thought best to examine only these four

parameters first. Each exponent was determined from a set of data in which only that parameter had been varied.

The exponent of the surface tension term was calculated to be 0.34 using the available data. The exponent of the viscosity increased with increasing viscosity. The highly viscous jets, however, were reported in Ref. 48 to breakup quite differently than less viscous jets. The high viscosity jets were torn into ligaments. The viscosity exponent for low-to-moderate viscous jets averaged to -0.30. Both exponents were rounded to $\pm 1/3$. The exponents on the orifice diameter and U_1 were determined to be -1.16 and 1.0 respectively with notable scatter. After the diameter exponent had been rounded to the value of -1.0 the relationship became:

$$N_n = 0.028 \sqrt[3]{\frac{\sigma}{\mu}} \frac{U_1}{d} \quad (5.1)$$

which has been tabulated in Table 23. The relation was developed using cgs units, consequently, the constant has the units of $(\text{sec/cm})^{0.33}$. The term under the radical is obviously a balance between surface tension forces and frictional forces on the waves. Of particular interest is the other term - the air velocity divided by the orifice diameter. Since the diameter of the initial jet column was equal to the orifice diameter, this term resembles the Strouhal number. For the flow around solid cylinders, the Strouhal number relates the frequency of vortex shedding in the von Karman

vortex street with the cylinder diameter and free stream velocity. Since the Reynolds number for the cases studied in this report was 1×10^5 (using U_1 and the jet diameter), then a vortex street flow situation is likely. For this Reynolds number, Schlichting (65) gives a value of 0.2 to the Strouhal number, ND/U . The frequencies of vortex shedding as predicted by the relation above are listed in Table 23 as Equation #1. The predicted frequencies follow some of the same trends as the observed frequencies and are of the right order of magnitude. The fluid jet flow is obviously much more complicated than the flow past solid cylinders. The cylindrical jet deforms, and the deformation must affect the gas flow around the jet. An interaction process between the gas flow and the jet deformations is highly likely. The surface tension and the viscosity of the liquid must also influence the jet deformation.

Shedding vortices have been observed and measured for gas jets in a gaseous crossflow. From hot-wire measurements, Moussa, Trischka and Eskinazi (56) determined that the vortices were shed alternatively from either side of the jet column. Such behavior would induce a flow that would sweep back and forth across the windward surface of the jet column. For the case of liquid jets, each sweep could produce a trough for a wave and, consequently, the wave frequency should be double that of the vortices. Doubling the values predicted by Equation #1 in the table yields a better correlation with the data. The correlation is particularly striking for jets with a \bar{q} near a

value of 10. For these jets, the correlation is usually within 10%, with the major exceptions being the extremely viscous jets. The shedding vortices may carry the shed droplets with them, thus explaining the high frequencies noted in the extinction signal for the subsonic crossflow injections.

This simple model of the formation of waves on the jet column would not only determine the frequency of the waves, but also the wavelength of the disturbances. While the gas flow oscillates back and forth across the jet column surfaces as vortices are shed alternately from the sides, the liquid is being continually moved upward at the jet velocity. The wavelength, consequently, should equal the liquid jet velocity divided by the wave frequency. Table 24 lists the observed initial wavelengths and the ones predicted by this simple analysis. There is generally good agreement. When there is disagreement between the analysis and the observations, the predicted wavelengths are smaller than the observed ones. The disagreement usually occurs for the larger jet diameters.

As the waves progress along the jet column, their wavelength grows. The speed of the disturbances also grows; their acceleration can be noted in Figure 50 which was taken from Kush and Schetz (46). In the plot, the difference between the wave speed and the jet velocity is plotted. If the data is extended to the orifice, the relative speed tends to zero, that is, the wave speed tends toward the jet velocity. Nejad and Schetz (48) tabulated the speed of the waves shortly after the sonic point on the curved bow shock. For the water

and the water/alcohol jets, the wave speed at this location was about 370 m/sec. The gas velocity near this point should have a similar magnitude. This data would suggest that the wave speed "starts" at the jet velocity before accelerating towards the velocity of the air striking the jet column. Due to the curvature of the bow shock, the velocity of the air striking the column also increases along the liquid jet.

To improve the agreement between the previously derived wave frequency relation and the observed values, the other tabulated parameters were added to the expression by a trial and error technique. Equation 5.1 suffered mainly from the drawback that it had no parameter to allow for the effects of \bar{q} on the wave frequency. Also, there seemed to be a parameter linked with the Mach number that needed to be included as well. The high Mach number case ($M_\infty=4$) had been underpredicted and the low Mach number case ($M_\infty=0.48$) had been overpredicted. Both of these factors could be handled by a variety of different parameters. By trial and error, it was determined that the jet velocity and the free stream stagnation pressure provided the best correlation with the experimental data. The liquid density was also concluded, partly for dimensional reasoning and partly due to the data from the Fluorinert jet, the single case where the liquid density differed substantially from the others. The resulting relation, included in Table 23, was:

$$N_w = 0.00007 \sqrt[3]{\frac{\sigma}{\mu l} \frac{P_{\infty}}{\rho l}} \frac{V_1}{d} V_j^{0.2} \quad (5.2)$$

In cgs units, for which the constant was derived, the constant has the units of $(\text{sec/cm})^{1.2}$. There was considerable uncertainty in the exponents on these additional parameters. Based on the data from the Kush and Schetz report, the exponent on the velocity term should be 0.15. The Nejad and Schetz data suggested that the exponent should have a value near one. In either case, the trend was the same; the wave frequency increased with increasing jet velocity. Overall, Equation 5.2 predicted the wave frequency within 20%, except for the extreme \bar{q} cases taken from the Nejad and Schetz study. Due to the disparity in the exponent for the jet velocity term, and since the 0.15 exponent from the Kush and Schetz data was selected for use in the expression (that data was more consistent), this disagreement is to be expected.

From a certain standpoint, the additional terms have not added much to the accuracy of the predictions. However, the main thrust of this analysis was not the development of an exact relation, but rather the illustration of certain jet phenomena. In order to produce an exact relation, the various wind tunnel experiments would have to be redone, and a consistent method for determining wave frequency would have to be tested and implemented. Several different types of photographic methods were employed in the experiments listed in Table

23; the lack of a standardized technique led to inconsistencies in the data.

The formation of jet column waves is a very difficult flow phenomenon to analyze. An analysis of the phenomenon would have to include models for the flow past a cylindrical column, for the stability of the liquid column including surface tension and viscous forces, and the coupling between the gas flow and the liquid flow. The gas flow, in addition to creating the shed vortices, also deforms the liquid column. The surface tension forces of the liquid resists these deformations. The viscous forces of the liquid act to damp out the deformations. The momentum of the liquid also would resist the deformations. The deformations, in turn, affect the gas flow, thus coupling the gas flow with the motion of the liquid. The stability of a liquid jet column (no crossflow) has been analyzed by several investigators (Ref. 67); the stability of the column is highly dependent on the wavelength of the disturbance. The coupling with the gas flow may excite a certain mode of disturbance within the liquid column. In the analysis of the oscillations of a viscous liquid column in the absence of a crossflow, the frequency of the oscillations was deemed to be proportional to the surface tension divided by the product of the density and the viscosity. The empirical equation derived in this report (Equation 5.2) found a similar grouping of terms. The underlying physics involved in Equation 5.2 can be outlined using the preceding observations. The frequency of the jet column waves can be directly linked with the

frequency of the shed vortices in the gas flow (the U/d term). The liquid column, under the influence of the flow of gas around it, oscillates and deforms and, consequently, causes the gas flow to oscillate as well (the term beneath the radical). In addition, the velocity (or momentum) of the liquid also exerts an influence on the frequency of the jet column waves.

The next jet phenomenon to be examined is jet breakup. Only two previous investigations had reported measurements of breakup, and both reports consisted of observations made from high speed motion pictures. For the fracture data compiled in Table 25, the original footage from both studies was re-examined. In the case of the Kush and Schetz observations, this yielded significantly lower frequencies for fracture than the original authors. Kush and Schetz, in examining the footage which had been shot at 36000 frames per second, based the fracture frequency upon the occurrence of clumps in the wake of the jet. Clumps were observed in every other frame which led the authors to conclude that the fracture frequency had been about 18 kHz. In calculating the fracture frequency here, the behavior of the jet column was examined for signs of fracture and then traced the fractured clumps downstream. Figure 3, obtained from the footage shot by Kush and Schetz, demonstrates the passage of clumps along the superimposed lines. The "clumps", which the previous authors had based their calculations on, visible in the far right of every other frame, do not seem directly connected with jet fracture. Fracture and jet column wave frequencies for the available test cases are listed in

Table 25 along with the Mach number, \bar{q} , and the gas velocity at the sonic point on the shock. Since the jet had been reported to fracture a short distance beyond the sonic point, the sonic velocity was included to represent the velocity of the air striking the jet column at the point of fracture. Some of the wave frequencies have been calculated using a previous relationship (Equation 5.2), since no wave data had been available for these test cases.

From stop-action photographs it has been noted that the fractured clumps are several wavelengths long. Reference 46 listed the length of the clumps as being between 2 and 4 wavelengths long for water jets in a supersonic crossflow. For jets in a subsonic crossflow, the clumps have been reported here as being between 2 and 6 wavelengths long. The approximate number of waves on the fractured clump can be readily calculated using a simple model. After the jet fractures, the jet column has to "grow back" before it can fracture again. The speed with which it grows back can be equated to the jet velocity (the motion is still nearly vertical) and also to the fracture frequency multiplied by the length of the fractured clump. Expressed mathematically this relation becomes:

$$V_j = (n\lambda)N_F \quad (5.3)$$

where n is the number of wavelengths on the fractured clump. The wavelength is merely the wave speed divided by the wave frequency.

The wave speed can be crudely approximated by the air velocity striking the fracture point. Consequently,

$$n = \frac{V_j}{\lambda N_F} = \frac{N_w V_j}{N_F V_w} \simeq \frac{N_w V_j}{N_F V_{g,F}} \quad (5.4)$$

Table 25 lists the calculated values of n . For the supersonic crossflows, the air velocity has been approximated by the velocity after the sonic point on the shock. Note that the values obtained for the high \bar{q} water jets agree well with the experimental observations, 3.5-4.0 as compared with 2-4.

Within a jet regime, it is unclear what effects \bar{q} exerts on the fracture frequency. The fracture frequency, however, definitely varies inversely with both the surface tension and the liquid viscosity. From the examination of the terms in Equation 5.4, it was determined that the effects of surface tension and viscosity on jet fracture go beyond merely affecting the speed and length of the waves along the jet column; the liquid properties must directly affect the fracture process. High viscosity, for example, not only retards the development of waves, but also directly retards the fracturing process.

Regime 1 jets do not break up in the same manner as higher \bar{q} jets. The jet column is extremely short, and virtually no waves can be identified along its surface. For inclusion in Table 25, the wave

frequencies for low \bar{q} jets were calculated under the assumption that the wave frequency equations were valid for even low \bar{q} jets (a dubious assumption since waves rarely form). Nonetheless, the analysis proved interesting, since it predicted that the Regime 1 jets would break up within a single wavelength. This prediction agrees with the visual observations made by Kush and Schetz, where in the rare event that a wave did not develop on a Regime 1 jet, the jet was reported to have immediately broken up at the trough of the wave.

For the subsonic crossflow case, n was determined from the pattern in the extinction traces. The preceding analysis was not valid for this crossflow condition, since the jet behaved differently. Instead of continually fracturing and "growing back", jets in a subsonic crossflow appear to spread out and break smoothly as indicated in Fig. 4.

It is significant that the four high \bar{q} water jets ($\bar{q}=10$ to 14) yielded values of n within the small range of 3.6 to 4.0. These tests had been conducted over a wide range of Mach numbers (0.48 to 4.0) and orifice diameters (0.051 to 0.091 cm). Apparently, n depends only on the regime of the jet flow and on the liquid properties. The regime of the jet flow, or \bar{q} , determines the mode of breakup, while the liquid properties influence the stability of the jet column. Weber (as outlined in Ref. 68) examined the stability of the liquid jet column in the absence of a crossflow and determined that there was a certain wavelength of disturbance for which the stability of the

column was minimized. This wavelength was dependent on the viscosity and the surface tension of the liquid.

Once the jet column has fractured, aerodynamic forces atomize the liquid. Ingebo and Foster (23) studied the formation of drops in a liquid jet subjected to a gaseous crossflow. Through dimensional reasoning and the examination of experimental data, they concluded that the drop sizes could be related to the product of the Weber number and the liquid film Reynolds number. The Weber number expresses the balance between the surface tension forces within the liquid with the turbulent momentum transfer forces of the airstream. The atomization, they found, also was affected by the liquid film resistance of the clumps and droplets to the formation of waves along their surfaces. Ingebo and Foster devised the following relationships from their experiments.

$$\frac{SMD}{d_o} = 4.68(We \cdot Re)^{-0.25} \quad (5.5)$$

$$\frac{D_{max}}{d_o} = 22.3(We \cdot Re)^{-0.29} \quad (5.6)$$

$$\text{where } We \cdot Re = \frac{\rho_g \rho_l d_o^2 V_g^3}{\mu_l \sigma} \quad (5.7)$$

They also considered the effects of jet velocity and concluded that it exerted no significant influence on the droplet sizes.

From the droplet sizes obtained in this investigation and in Ref. 42 (listed in Table 26) the following relationship was developed:

$$\text{SMD (in microns)} = 3500 \left(\frac{\mu \sigma}{U g v_j} \right)^{0.2} \left(\frac{1}{\rho_l} \right)^{1.4} \text{ (in cgs units)} \quad (5.8)$$

The droplet sizes tabulated are the atomized droplet sizes observed at $x/d=60$ and 100 . The effects of the orifice diameter appeared to be negligible, in contrast to the results of Ingebo and Foster. In the table, the results from various orifice diameters have been combined. Since the $We \cdot Re$ number depends on the orifice diameter, a range of $We \cdot Re$ values are given for these entries. The air density was not varied, so it does not appear in the relation above. The exponents should be considered to be a first approximation only, since each was derived from only a few test cases, and there was notable scatter. There was considerable deviation in the calculated exponent for the jet velocity.

Comparing the two relations above, the exponents for the liquid properties are close, especially considering the statistical errors in the equation developed from the data in Table 26. The discrepancy in the velocity terms can be partially explained by considering the \bar{q} range tested. The minimum \bar{q} that Ingebo and Foster tried was 15 while the \bar{q} ranged from 4 to 12 in Table 26. As was evident in the visual

observations and in the preceding discussions, \bar{q} (including the regime of the jet flow) has a decisive influence on how the jet breaks up. The jet velocity term in the above expression partially reflects the differences between Regime 2 and Regime 3 jets. All of Ingebo and Foster's data were obtained from Regime 3 jets. Presumably, the jet velocity does not play as important a role at higher \bar{q} as it does for values of \bar{q} between 4 and 12. Table 26 lists the predicted values of SMD as obtained from both the Ingebo and Foster equation and the one developed in this report. Both reflect the trends in the data, but the equation from Ref. 23 drastically overpredicts the droplet sizes (perhaps this equation is not valid for low \bar{q}).

The listed D_{\max} values were obtained from the droplet size distributions and denotes the diameter below which 90% of the droplets in the distribution lay. In the available data, the value of D_{\max} was consistently 2.8 times that of the measured SMD; the ratio dropped slightly to a value of 2.5 for the subsonic crossflow condition.

Both relations dramatically overestimated the droplet sizes for the injection into a subsonic crossflow. Examination of the velocity data from single phase jets (Ref. 56) revealed that, in those flows, the velocity accelerated to double the free stream value (similar to the acceleration around a blunt body) near the jet body. Doubling the free stream velocity produced predicted droplet sizes that nearly matched those found experimentally.

The atomization of the droplets seems dependent on the forces mentioned by Ingebo and Foster: surface tension, turbulent momentum transfer and liquid film resistance. In addition, the regime of the jet flow has a definite influence. Since the orifice diameter does not directly affect any of these forces or factors, it is not surprising that the droplet sizes appear to be independent of that variable. Perhaps the droplet diameter would be a better non-dimensionalizing length for the Weber and Reynolds number than the orifice diameter as used by Ingebo and Foster in their relations.

5.4 Droplet Size Distributions

5.4.1 Subsonic Crossflow

Due to the relative smoothness of the jet behavior (breakup, etc.), the groupings of droplets tended to have Gaussian size distribution profiles. Two distinct groups can be identified. Figure 51 contains the distributions taken at four x/d stations with a 0.35 msec exposure (these plots are also contained in Fig. 11). In the $x/d=10$ profile, the droplets are mostly in a group centered around 25 microns, and there is some evidence of a very disperse group of extremely large droplets. By the $x/d=30$ station, the larger group is more prominent, extending down to a diameter of 75 microns. The smaller group has shifted down to the 10-15 micron range. By the $x/d=50$ station, the smallest group seems to be centered around the smallest bin; the larger group is centered around 50 microns. The $x/d=50$, $z/d=20$ profile in Fig. 11 shows a group in the largest bins.

In Fig. 51 the $x/d=100$ distribution seems to show the three groups; the smallest group would appear to be centered around 7 microns, another group around 25-30 microns, and the third group around 40-60 microns. The $x/d=100$, $z/d=20$ profile in Fig. 11 does not show the smallest group (which has evidently been atomized below 7 microns) but shows the other groups centered around 20-25 microns and 80-100 microns.

The smallest group of droplets was probably created by the shedding of droplets off the sides of the jet plume. Until the droplets "disappear" below 7 microns, these droplets are always apparent in the profiles. The larger groups "appear" and "disappear" both temporally and spatially, suggesting that these groups are the remnants of the fractured clumps. It is uncertain whether the two larger groups represent the same clump (which had split into two sub-clumps) or if they represent two different clumps with different droplet sizes. The profiles showing three groups simultaneously ($x/d=100$, $z/d=10$) can be interpreted in various ways - as three groups or as two groups or even as a single group. The "groups" are not very distinctly separated. Since the largest group is usually visible only at larger z/d , this fact would suggest that the clump(s) can be classified into two size groups. The smaller clumps of droplets have a mean diameter of around 50 microns at $x/d=50$ and are most visible around $z/d=10$. The other type of droplet clump is atomized down to the 80-100 micron range by $x/d=100$ and is "thrown" by the jet to higher z/d .

With the sources of the droplets tentatively identified, the three-dimensional distribution of droplet sizes can be conjectured. The small size droplet shedding which occurs along the sides of the jet should form an outer core around the plume boundaries. The population of droplets should remain relatively constant in this region, since droplets should be shed continually. Even at small x/d the droplets in the outer core are small; at $x/d=10$ the majority of these droplets are less than 30 microns in diameter. The inner core of the plume is dominated by the passage of the clumps. Photographs show that the clumps progress downstream at heights ranging from about $z/d=10$ to 30. The droplets in these clumps are relatively large. Apparently, the larger droplets are "thrown" to larger z/d than the smaller ones. Due to momentum considerations, larger (more massive) droplets would tend to penetrate higher than smaller droplets. Perhaps, the two divisions of the large droplets were created by the same clumps; the clump splitting into two sub-clumps due to differing inertia.

Interestingly, the noted arrangement of large droplets (the more massive droplets penetrating farther) would be partially hidden from SMD measurements. From the center of the plume upward (toward larger z/d) the laser beam would pass through a larger thickness of the outer core as compared with the central core. Eventually, the beam would entirely "miss" the central core. Consequently, as the beam moves upward into the region of larger and larger droplets in the central core, the beam would be passing through a larger and larger percentage

of small droplets in the outer core; the two effects would tend to cancel each other. This simple analysis assumes that the thickness of the outer core is constant around the plume at a given x/d .

5.4.2 Supersonic Crossflow

The profiles for injection into a supersonic air stream are more complicated than those for injection into a subsonic stream. The data trends are not as clear, and the profiles rarely resemble Gaussian curves.

The atomization of the water/methanol jet are shown in Fig. 31. The largest groups of droplets (70-100 microns) are shifted into the 40-60 micron bins, while the smaller droplets (20-30 microns) are shifted into the smallest bin as the jet progresses from $x/d=24$ to 80. Figure 30 suggests that the outer core of droplets are in the 7-20 micron range at $x/d=40$, since moving from the center of the plume toward to the jet boundary induces a shift from the 20-30 bins into the 7-20 micron bins. This conjecture is supported also by the atomized sizes listed in Table 26. Presumably, the droplets shed off the sides of the plume are "atomized" droplets, since they exist in near free stream conditions. Experiment and the two analyses in Table 26 attribute a diameter in the range of 10-20 microns to atomized water/alcohol droplets in a Mach 3.0 free stream.

Figure 35 demonstrates the atomization of two droplet size groups for the case of high \bar{q} water injection. At $x/d=30$, the two groups are centered around 30 microns and 60 microns, respectively. The 7-15

micron bin populations probably denote the droplets shed off the plume. The $x/d=40$ profiles show a great deal of fluctuation. One profile (the solid line case) shows only the shed droplets. In the other two, the droplet groups are centered around 25-30 microns and 40-60 microns. At $x/d=60$ the groups have shifted to the ranges of 20-30 and 40-50 microns. By $x/d=100$, the smaller group has evidently shifted into the smallest bin (and possibly below causing the noted errors in the SMD). The largest group appears in the 20-40 micron range.

Figure 36 taken at $x/d=30$ also suggests that the shed droplets are represented by the smallest bin. Comparing the $z/d=10$ (Fig. 35c) and 18 (Fig. 36d) profiles, the population in the 7-15 micron bin increases by a factor of 1.5, while the larger group population is cut by half in going from $x/d=10$ to 18. Furthermore, the observed atomization size for this high \bar{q} water condition was 13-14 microns. It is curious that the smaller of the two clump droplet size groups was evident in the 20-30 micron bins for x/d up to 60. The Ingebo and Foster analysis yielded a SMD value of 25-36 microns for this test condition. Similarly, the largest group was evident in the 40-60 micron for $x/d=30$ and 40. The Ingebo and Foster relation for D_{max} yielded values in the 58-79 micron range. For this jet, the Ingebo and Foster analysis yielded fairly accurate results.

The trends for the lower \bar{q} jet were not as definite. Progressing from $z/d=20$ to 50 in Fig. 46, the shifting of the two groups can be

discerned. The smaller group begins centered around 25 microns and shifts into the smallest bin. Starting around 50 microns, the larger group becomes atomized to 25 microns. Shed droplets populate the smallest bin. The trends are partly disguised by the dramatic fluctuations (as in Fig. 45) in the distributions. This low \bar{q} is classified as a Regime 2 jet, an intermediary step between the other two regimes. Kush and Schetz (46) describe a Regime 2 jet as being extremely irregular, much more so than a Regime 3 jet.

The previous discussion highlights another difference between injection into supersonic and subsonic crossflows - the location of the various droplet sizes associated with jet fracture. In the subsonic case, the average size of the large diameter droplet groups were seen to increase with increasing z/d ; in the supersonic case both groups often were found at the same location at the same instant. The violent whipping of the supersonic jets (observed in Ref. 46 and others) might explain how the various droplet sizes are evident at all of the plume locations. The whipping has dispersed the various clumps throughout the plume.

5.5 Plume Dimensions

Several previous investigators have derived empirical equations for the penetration height and width for water jets in a supersonic crossflow. The earlier researchers measured the jet dimensions by means of streak photographs, a practice disdained by later investigators who used temperature and mass sampling surveys. The

cross sectional photographs taken in the course of this investigation seem immune to the faults of the previous photographic methods. This section will examine the empirical equations derived in previous reports and compare them with the data from the cross sectional photograph. This discussion is basically an extension of the one in Thomas and Schetz (39). The previous report was limited to a single \bar{q} and a single downstream station.

Using streak photography, Yates and Rice (64) developed the following equation for the transverse injection of a water jet into a Mach 3 air flow:

$$h/d = 1.15 \bar{q}^{1/2} \ln(1+6x/d) \quad (5.9)$$

Joshi and Schetz (35) developed an expression for the plume width at $x/d=25$ using streak photography. An insignificant pressure term has been omitted here from the expression. For a circular injector, $C_d=1.0$ and

$$w/d = 11.2(\bar{q}C_d)^{0.19} \quad (5.10)$$

Shaikhutdinov and Klevanskii (37) with a temperature survey devised the following relations:

$$h/d = 3.75 \bar{q}^{.414} (x/d)^{0.239} \quad (5.11)$$

$$w/d = 13.8 \bar{q}^{-0.25} \quad \text{at } x/d=30 \quad (5.12)$$

Thomas and Schetz (39) performed a mass sampling survey and concluded that the equation from Ref. 37 yielded an accurate value. The equations from the other two references were discovered to dramatically underestimate the plume dimensions.

The penetration heights as calculated from the cross sectional photographs and the preceding relations can be found in Table 27. Of prime interest was the differing forms of the equations, i.e. the dependence of \bar{q} and x/d . To this end, the equation from Ref. 64 was multiplied by a compensation factor of 1.44. This factor compensated for the underestimation of the plume dimensions caused by the use of the streak photography method used in Ref. 64. The compensation factor allows the accuracy of the form of the equations to be directly compared. The relation developed in Ref. 37 obviously yielded better agreement with the observed h/d than the uncompensated relation from Ref. 64. The latter equation, however, followed the trends in changing \bar{q} and x/d slightly better than the former. With the compensation factor, the latter equation yielded reasonably good results. Assuming that the dependence of x/d was a simple power relation, the following equation was developed directly from the data and tabulated:

$$h/d = 2.2 \bar{q}^{1/2} (x/d)^{0.4} \quad (5.13)$$

From Table 27 it is evident that the penetration height grows at an increasing rate beyond $x/d=60$; in order to obtain a reasonably accurate value at $x/d=100$ the heights at the previous stations had to be overestimated in general.

The equation from Ref. 35 predicts a jet width of 20 and 24 for water jets at $\bar{q}=4$ and 10, respectively after the addition of a multiplicative factor of 1.4 to Equation 5.10. Again, this factor compensates for the deficiencies of the streak photography method. The equation from Ref. 37 predicts widths of 20 and 25 which match the observed jet widths at $x/d=30$. Since the equation from Ref. 35 was designed for $x/d=25$, it is not immediately clear which equation has the best form. From examination of the present jet width data at several x/d stations, the \bar{q} dependence was determined to be $\bar{q}^{-0.19}$ which matches the form suggested by Joshi and Schetz (35).

No equation relating the penetration height to x/d was found in the literature for the subsonic case. The following relation was developed here and tabulated in Table 27:

$$h/d = 10.3(x/d)^{0.28} \quad (5.14)$$

Note that a simple power relation yields good results even to a $x/d=100$ unlike the supersonic counterpart.

Due to the regularity of the break up, the main core of the jet in a subsonic stream could be discerned in the cross sectional

photographs. The main core (the bright center of the plume) penetrated 70% as far as the rest of the plume. Something akin to this steady main core must have been the object measured in the streak photographic surveys since $1/0.7=1.4$, the factor by which the earlier investigators consistently underestimated the plume dimensions.

5.6 Other Time-Dependent Phenomena Within Plume

The division of the jet plume into the spray formation zone and the atomization zone as depicted schematically in Fig. 1 can be accomplished by examining the standard deviation of the SMD. In general, the standard deviation is large throughout the spray formation zone. The large deviations are indicative of the unsteadiness and the dynamic behavior of the breakup process. In the atomization zone, the standard deviation decreases as the droplets tend toward a uniform, well atomized state.

This trend was observable in the two high \bar{q} tests in the supersonic crossflow (the water and the water/methanol jets). The standard deviation increases from the $x/d=10-20$ stations to the $x/d=30-40$ stations and then decreases further downstream. From a study of numerous photographs and motion pictures, a $\bar{q}=10$ jet exhibits clumps in the $x/d=9$ to 35 range, indicative of the spray formation zone. In the atomization zone, not only did the standard deviation decrease, but so did the amplitude of the extinction fluctuations. Between the $x/d=10$ and 100 stations, for the water jet, the amplitude dropped by a factor of five. Obviously it would be more difficult to

detect the effects of breakup in the atomization zone than in the spray formation zone; the atomization process seems to dampen the fluctuations in the spray caused by jet fracture.

In the low \bar{q} water tests in a supersonic crossflow, both the standard deviation trends and the photographic evidence suggest that the spray formation zones extends to $30d$ downstream of the injector. The increase in the standard deviation in the spray formation zone was not discernible at this flow condition, only the decrease through the atomization zone. A low \bar{q} jet atomizes within a shorter distance than its high \bar{q} counterpart. The low \bar{q} jet also produces larger droplets. This difference in the droplet sizes is best illustrated by results of Ref. 48 where this relationship was consistently observed in tests involving three different liquids and two orifice sizes. It seems probable that the shorter spray formation zone was partly responsible for the increased droplet sizes. Possibly the increase in the standard deviation in the low \bar{q} test around the $x/d=100$ station was due to the effects of the turbulent mixing of the droplets with the cross stream.

The standard deviation also increased with increasing z/d for all cases, indicating the turbulent nature of the upper reaches of the main jet core. For the injection into a subsonic crossflow, only this last trend was observable. In the subsonic case, the deviation in SMD did decrease slightly with increasing downstream distance, but the trend was not very consistent.

Another transient phenomenon which followed a definite pattern was the vertical location of the largest observed standard deviation and extinction amplitude as a function of x/d . With some scatter created by the relatively wide spacing of the test grid, both quantities peaked at a z/d corresponding to 40% of the penetration height. It was initially considered that these locations might correspond to the locations of maximum liquid flow where large fluctuations might be expected due to the nature of the jet fracture. Based on the extinction values (Tables 14 and 19), however, the maximum liquid flow seemed to occur around $z/d=10-20$ and $z/d=5-10$ for the high and low \bar{q} water jets, respectively. The height of the maximum liquid flow increased at a significantly lower rate than either the penetration or the maximum fluctuations. This result was confirmed by examination of the photographs in which the fractured clumps tended to move almost parallel with the free stream and also by the cross section photographs where the jet core was definable. Thomas and Schetz (39) measured the mass flow directly by a mass sampling probe. For water injected at $\bar{q}=6$ into a Mach 3.0 air stream, the maximum liquid flow was found at $z/d=10$, a result which confirms the ability of the extinction setup to measure the relative mass (liquid) flow.

The mass sampling survey from Ref. 39 suggested a possible explanation as to why the deviations peaked at 0.4h. The results of the survey, Fig. 52, show the mass flow and the percent fluctuations found in the mass samples at each location in the plume cross section.

The location of the "kidney" core has been outlined on the figure. Thomas and Schetz located the "kidney" by noting at which z/d values the mass sampling was maximum at each y/d . The "kidney" can also usually be identified by the relatively low fluctuations within the "kidney" except at the $z/d=8$ location. Not only was the fluctuation large at this location, but it also was a local maximum. Based on a penetration height of $19d$, this location corresponds to a height of $0.42h$, the same height at which large deviations were noted in this study. A total pressure survey conducted in Ref. 39 also indicated large pressure fluctuations in the same vicinity. The fluctuations observed in the mass flow and the total pressure in the main jet core were distinct from the fluctuations observed along the jet boundaries.

From numerous single phase jet experiments (air jet into air flow, etc.) the location of the bound vortices, contained within the "kidney", has been well documented. Comparing the results of Ref. 56 (an air jet) with the "kidney" drawn in Fig. 52 the bound vortex should be centered near the $z/d=8$ site. Perhaps the large fluctuations observed in the water jets were created by bound vortices within the jet core.

Extending the analogy between single phase and double phase jet flows, the shed vortices should be located beneath the bound vortices at approximately half the height of the bound ones. In the mass sampling survey, the $z/d=4$, $y/d=8$ location has a usually large fluctuation, especially considering the amount of mass collected there. Even for being close to the jet boundary the fluctuations at

this location are significant. The pressure survey also showed relatively large fluctuations in this region. Similarly, the extinction measurements showed relatively large fluctuations at 0.2h; these fluctuations, while not being as large as the ones at 0.4h, were larger than any noted in the top half of the jet core. Since only a small amount of liquid (mostly shed droplets) should have been entrained in the shed vortices, these vortices would be expected to influence the extinction to a lesser extent than the bound vortices.

It should be mentioned that in the mass sampling tests of Ref. 39 the reported fluctuations were noted in samples each taken during a 5 second sampling time. In other words, the reported fluctuations must be of a low frequency and cannot be directly correlated with the high frequency oscillations observed in this study. The low \bar{q} jet in a supersonic crossflow in the present study also showed significant low frequency oscillations. Based on the standard deviation at long exposure times, the low \bar{q} jet exhibited the strongest low frequency fluctuations of any jet studied for this report.

The low frequency oscillations may be correlated with the liquid layer upstream of and surrounding the injector orifice. Kush and Schetz (46) among others commented on the considerable amount of liquid upstream of the injector in the liquid layer for Regime 2 (such as $\bar{q}=4$) water jets in a supersonic crossflow. Correspondingly, this jet condition produced the largest standard deviations at long exposure times (greater than 20 msec) in the SMD measurements in the

present study. Regime 3 jets contain significantly less liquid in this region; the deviation in SMD for the high \bar{q} water jet in the supersonic crossflow was significantly lower than that observed for the $\bar{q}=4$ case. The present study, as well as Ref. 36, observed no liquid layer near the injector for water injection into a subsonic crossflow. Accordingly, the deviation in SMD was lower for this test condition than for the supersonic crossflow water injections. No observations were made of the liquid layer for the water/methanol injection which had the lowest SMD deviation of any jet tested here. In the laboratory it was observed that the presence of liquid around the injector orifice has a definite influence on the jet. For injection into ambient air, the liquid emerges in a fairly steady column before breaking up due to Rayleigh instabilities. If a globule or layer of liquid surrounds the orifice, the jet column wavers noticeably in an aperiodic oscillation. The presence of an upstream liquid layer, which would "cover" the orifice, may induce considerable instabilities in the jet column; these instabilities may be the cause of the observed low frequency oscillations. It is uncertain, however, whether the upstream liquid layer is a cause or is a symptom of some other jet phenomenon. Most likely, the processes are interactive - the crossflow and injection conditions allow an upstream liquid layer to form, the liquid surrounding the orifice induces these low frequency oscillations which feeds more liquid into the layer, and so on. It should be mentioned that Thomas and Schetz (39) observed that

the separation zone at the intersection of the liquid layer with the bow shock oscillated.

Another transient problem is the difference between injection into supersonic versus subsonic crossflows. One possible explanation for the violent whipping associated with supersonic injection can be based on the shock waves that form on the windward faces of the fractured clumps. The fracture occurs in a region of supersonic flow (beyond the sonic point on the bow shock created by the jet plume). Shock waves are evident emanating from the clumps at the time of fracture in the photographs. From the motion pictures, the clumps appear to have been sheared off the jet column and swept downstream. This shearing is in stark contrast to the behavior of subsonic crossflow injection wherein the liquid spreads out and breaks periodically. Apparently the supersonic and shock flow allow the jet column to penetrate to a certain height, at which point, due to the aerodynamic forces acting upon it, the jet is unstable and is forced to fracture. Furthermore, if bound vortices do exist within the liquid jet, then they would also be sheared off by the crossflow. The severed vortex filament could then include the violent whipping and lashing associated with jet fracture in a supersonic crossflow.

CONCLUSIONS

When a liquid is injected into a gaseous crossflow through a simple orifice, the emanating jet column is not stable. The stability of the column is partly dependent on the conditions immediately upstream of the injector. Oscillations in the supersonic upstream separation region and/or the existence of an upstream liquid layer can induce relatively low frequency fluctuations in the jet. Since the jet column is unstable, perturbations can grow into wave-like disturbances that will propagate along the jet body. Vortices shed off the sides of the column also may provide the perturbations that create the observed wave phenomena. The Strouhal numbers for the liquid columns are slightly different than those for rigid cylinders due to the deformation of the liquid column. The properties of the liquid and the injection conditions influence how the column deforms and, consequently, affect the frequencies of the shed vortices and the waves.

Once the waves form, they accelerate along the jet column. There is some evidence that indicates that aerodynamic forces aid in the acceleration and that the wave speed accelerates to the velocity of the air striking the jet column. For Regime 3 (high \bar{q}) water jets, the aerodynamic forces appear to amplify every fourth column wave, and these large aerodynamically-induced waves eventually lead to the fracture of the column. The number of column waves per a fractured

clump seems dependent on the liquid properties and on the regime classification (\bar{q} range) of the injection.

The droplets in the spray plume can be classified into two groups: the small droplets shed off the windward surface of the jet and the large droplets contained within the fractured clumps. In the immediate wake of the jet, the clumps were observed 11% of the time. The passage of the clump momentarily raises the SMD of the spray from the 15-19 micron range to the 20-30 micron range for the test conditions studied here. The droplets within the clumps become increasingly atomized as they progress downstream. The aerodynamic forces caused by the relative velocity between the drops and the gas flow, along with the surface tension and the liquid film resistance of the drops, determine the size of the atomized drops. The droplets within each clump can be classified into several size groups. For injection into a subsonic crossflow, the larger droplets are observable at larger heights than the smaller droplets. Due to the whipping of the jet in a supersonic crossflow, the different size groups can be found at most plume locations at those conditions.

Further work needs to be performed concerning the relatively low frequency oscillations and their cause. Also, the existence and the effects of the shed vortices need to be confirmed and quantified. The splitter plate experiments performed with single phase jets could be extended to two-phase jets to observe the effects that these vortices exert on the jet behavior.

In future studies of liquid jet transients, the laser beam extinction tests would be an advisable preliminary step. The extinction measurements can easily and quickly identify the frequencies of the major jet transients. The knowledge of these frequencies would be invaluable, since it would be difficult otherwise to know a priori what measurement rates would be best for that particular experiment and flow condition.

The very useful, new droplet sizing instrument developed here was found to have some drawbacks. The arrangement of the small diameter bins along with the 7 micron limitation proved to be a poor choice for sprays of SMD less than 17 microns. The size of the high speed buffer memory which limited the number of sequential measurements to three was also a serious limitation. Tripling the memory size would be most beneficial; ten sequential measurements could then be made. This number would allow the system to scan one fluctuation period, guaranteed that at least one clump passage would be detected (since the clumps are observable slightly more than 10% of the time). Alternatively, the ten measurements could scan a single clump passage, and the temporal distribution of droplets within the clump could be obtained.

Other jet transient phenomena can be measured. The jet dimensions could be measured by a high speed video camera. To avoid the optical problems encountered in the CCD penetration attempt and in the traditional (streak) optical setups, the plume could be illuminated by a plane of light such as was done for the cross

sectional photographs presented here. A high speed camera focussed on this plume "slice" could record the fluctuations of the plume dimensions. Such a setup, however, would require either a higher ASA rated camera or a more powerful laser than those used in this report (note the high ASA rating and the long exposure times of the cross sectional photographs). A camera that could be operated at higher frame rates also would be beneficial for future experiments.

REFERENCES

1. Rayleigh, Lord, "On the Instability of Jets," Proc. of London Math Soc., X, 4, 1878.
2. Rayleigh, Lord, "On the Instability of Cylindrical Fluid Surfaces," Phil. Mag., XXXIV, 59, 1892.
3. Weber, C., "Zum Zerfall eines Flüssigkeitsstrahles," Ztschr. f. angew Math. und. Mech., Vol. 2, 1931.
4. Tomotika, S., "On the Instability of a Cylindrical Thread of a Liquid Surrounded by Another Viscous Fluid," Proc. of Royal Soc. of London, A, 150, 322, 1935.
5. Castleman, R., "The Mechanism of Atomization of Liquids," J. of Research of the Bureau of Standards, 6, 369, 1931.
6. Castleman, R., "The Mechanism of Atomization Accompanying Solid Injection," NACA Report 440, 1932.
7. Dunne, B. and Cassen, C., "Some Phenomena Associated with Supersonic Liquid Jets," J. of Appl. Physics, 25, 5, 1954.
8. York, J., Stubbs, H. and Tek, M., ASME Trans., pp. 1279-1286, October 1953.
9. Miesse, C., "Correlation of Experimental Data on the Disintegration of Liquid Jets," Industrial Eng. Chem., 47, 9, 1955.
10. Yuen, M., Jour. Fluid Mech., 33, 151, 1968.
11. Nayfeh, A., "Nonlinear Stability of a Liquid Jet," Phys. of Fluids, 13, 841, 1970.
12. Kelvin, Lord, "Influence of Wind and Capillarity on Waves in Water Supposed Frictionless," Mathematical and Physical Papers, Cambridge U. Press, 1910, iv.
13. Jeffreys, H., "On the Formation of Water Waves by Wind," Proc. of Royal Soc. of London, 107, 189, 1925.
14. Lighthill, M., "Physical Interpretation of the Mathematical Theory of Wave Generation by Wind," Jour. Fluid Mech., 14, 385, 1962.
15. Lighthill, M., Comm. Pure Appl. Math, XX, 1967.
16. Lamb, H., Hydrodynamics, Dover Pub., Sixth Ed., 1945.

17. Taylor, G., "Effect of Variation in Density on the Stability of Superposed Streams of Fluid," Proc. Royal Soc., A, 132, 399, 1931.
18. Taylor, G., "The Instability of Liquid Surfaces when Accelerated in a Direction Perpendicular to Their Planes I," Proc. Royal Soc. of London, A, 201, 192, 1950.
19. Lewis, D., "The Instability of Liquid Surfaces when Accelerated in a Direction Perpendicular to Their Planes II," Proc. Royal Soc. of London, A, 202, 81, 1950.
20. Bellman, R. and Pennington, R., "Effects of Surface Tension and Viscosity on Taylor Instability," Quart. Jour. Appl. Math., 12, 151, 1954.
21. Nayfeh, A. and Saric, W., "Non-linear Kelvin-Helmholtz Instability," Jour. Fluid Mech., 46, 209, 1971.
22. Chelko, L., NACA RM E50F21, 1950.
23. Ingebo, R. and Foster, H., "Drop Size Distribution for Cross-Current Breakup of Liquid Jets in Airstream," NACA TN 4087, 1957.
24. Weiss, C. and Worsham, C., "Atomization in High Velocity Air Stream," ARS Journal, 29, 4, 252, 1959.
25. Bitron, M., "Atomization of Liquids by Supersonic Air Jets," Ind. and Eng. Chem., 47, 23, Jan. 1955.
26. Adelberg, M., "Breakup Rate and Penetration of a Liquid Jet in a Gas Stream," AIAA J., 5, 1408, 1967.
27. Clark, B., "Breakup of a Liquid Jet in a Transverse Flow of Gas," NASA TN D-2424, 1964.
28. Forde, J., Molder, S. and Szpiro, E., "Secondary Liquid Injection Into a Supersonic Airstream," J. of Spacecraft and Rockets, 3, 8, 1172, 1966.
29. Kolpin, M., Horn, K. and Reichenbach, R., "Study of Penetration of a Liquid Injectant into a Supersonic Flow," AIAA J., 6, 5, 853, 1968.
30. Reichenbach, R. and Horn, K., "Investigation of Injectant Properties on Jet Penetration in a Supersonic Stream," AIAA J., 9, 3, 469, 1971.
31. Horn, K. and Reichenbach, R., "Further Experiments on Spreading of Liquids Injected into a Supersonic Flow," AIAA J., 7, 2, 358.

32. Catton, I., Hill, D. and McRae, R., "Study of Liquid Jet Penetration in a Hypersonic Stream," AIAA J., 6, 11, 2084, 1968.
33. Edelman, R., Schmotolocha, S. and Slutsky, S., "Combustion of Liquid Hydrocarbons in a High Speed Airstream," AIAA Paper 70-88.
34. Sherman, A. and Schetz, J., "Breakup of Liquid Sheets and Jets in a Supersonic Gas Stream," AIAA J., 9, 4, 666, 1971.
35. Joshi, P. and Schetz, J., "Effects of Injector Shape on Penetration and Spread of Liquid Jets," AIAA J., 13, 9, 1137, 1975.
36. Padhye, A. and Schetz, J., "Penetration and Break-up of Liquid Fuel Jets in High Subsonic Speed Air Streams," AIAA Paper 77-201.
37. Shaikhuldinov, Z. and Klevanskii, V., "Penetration and Mixing of Liquid Injected into Supersonic Transverse Gas Stream," Izvestiya vuz, Aviatsionnaya Tekhnika, 19, 1, 99, 1976.
38. Yang, M., Gu, S., Liu, G. and Li, X., "Trajectory with Diffusion Method for Predicting the Fuel Distribution in a Transverse Stream," AIAA Paper 83-0336.
39. Thomas, R., "Distributions Across the Plume of Transverse Liquid and Slurry Jets in Supersonic Airflow," Master's Thesis, VPI&SU, 1984.
40. Gooderum, P. and Bushnell, D., "Atomization, Dropsizes, and Penetration for Cross-stream Water Injection at High Altitude Reentry Conditions with Application to RAMC-1 and C-III Flights," NASA TN D-6747, 1972.
41. Dobbins, R., Crocco, L. and Glassman, I., "Measurements of Mean Particle Sizes of Sprays from Diffractively Scattered Light," AIAA J., 1, 8, 1882, 1963.
42. Nejad, A. and Schetz, J., "Effects of Physical Properties and Location in the Plume on Mean Droplet Diameter for Transverse Liquid Injection in a Supersonic Air Stream," AIAA Paper 81-0188.
43. Swithenbank, J., Beer, J., Taylor, D., Abbot, D. and McCreath, G., "A Laser Diagnostic Technique for the Measurement of Droplet and Particle Size Distribution," AIAA Paper 76-69.
44. Ruscello, L. and Hirleman, E., "Measurement of Droplet Size Distributions Using a Photodiode Array," Paper 81-19, 1981 Fall Meeting, Western States Section, Combustion Institute.

45. Ewan, B., Swithenbank, J. and Sorousbay, C., "Measurement of Transient Spray Size Distributions," *Optical Eng.*, 23, 5, 620, 1984.
46. Kush, E. and Schetz, J., "Decomposition of a Liquid Jet Injected Normal to a Supersonic Airstream," Ph.D. Thesis, VPI&SU, 1972.
47. Kush, E. and Schetz, J., "Liquid Jet Injection into a Supersonic Flow," AIAA Paper 72-1180.
48. Nejad, A. and Schetz, J., "The Effects of Viscosity and Surface Tension of Liquid Injectants on the Structural Characteristics of the Plume in a Supersonic Airstream," AIAA Paper 82-0253.
49. Nejad, A., "Effect of Physical Properties on Break-up and Atomization of Liquid Jets in a Supersonic Crossflow," Ph.D. Thesis, VPI&SU, 1982.
50. Rajaratnam, N., "Theory of Turbulent Jets," Handbook of Fluids in Motion, ed. Chermisinoff, N. and Gupta, R., Ann Arbor Science, 1983, pp. 251-279.
51. Crabb, E., Durao, D. and Whitelaw, J., "A Round Jet Normal to a Cross-flow," ASME 80-Wa/Fe-10.
52. Fearn, R. and Weston, R., "Vorticity Associated with a Jet in a Cross Flow," AIAA J., 12, 12, 1666, 1974.
53. Pratte, B. and Baines, W., "Profiles of the Round Turbulent Jet in a Cross Flow," *Jour. of Hydraulics Div.*, Proc. of ASCE, 92, No. HY6, 53, 1967.
54. Roshko, A., "Experiments on the Flow Past a Circular Cylinder at Very High Reynolds Number," *Jour. Fluid Mech.*, 10, 345, 1961.
55. Roshko, A., "On the Development of Turbulent Wakes from Vortex Streets," NACA Report 1191, 1954.
56. Moussa, Z., Trischka, J. and Eskinazi, S., "The Near Field in the Mixing of a Round Jet with a Cross-stream," *Jour. Fluid Mech.*, 80, 49, 1977.
57. McMahon, H., Hester, D. and Palfrey, J., "Vortex Shedding from a Turbulent Jet in a Crosswind," *Jour. Fluid Mech.*, 48, 73, 1971.
58. Goodman, J., Introduction to Fourier Optics, McGraw-Hill, San Francisco, 1968.
59. Phillips, D., "A Technique for the Numerical Solution of Certain Integral Equations of the First Kind," *J. ACM*, 9, 84, 1962.

60. Twomey, S., "On the Numerical Solution of Fredholm Integral Equations of the First Kind by the Inversion of the Linear System Produced by Quadrature," J. ACM, 10, 97, 1963.
61. Caroon, T. and Borman, G., "Comments on Utilizing the Fraunhofer Diffraction Method for Droplet Size Distribution Measurement," Combustion Science and Technology, 19, 255, 1979.
62. Tishkoff, J., "Spray Characterization: Practices and Requirements," Optical Eng., 23, 5, 557, 1984.
63. Dodge, L., "Change of Calibration of Diffraction-Based Particle Sizers," Optical Eng., 23, 5, 626, 1984.
64. Yates, C. and Rice, J., "Liquid Jet Penetration," Research and Development Programs Quart. Report, U-RQR/69-2, APL, 1969.
65. Schlichting, H., Boundary-Layer Theory, McGraw Hill, New York, Seventh Edition, 1979.
66. Chang, I. and Russell, D., "Stability of a Liquid Layer Adjacent to a High-Speed Gas Stream," Phys. of Fluids, 8, 1018, 1965.
67. Anno, J., The Mechanics of Liquid Jets, Lexington Books, Lexington, MA, 1977.
68. Lefebvre, A., Gas Turbine Combustion, Hemisphere Pub., Washington, 1983.

APPENDIX

From the droplet size distributions a number of variously defined mean diameters can be calculated. In this report the Sauter Mean Diameter was calculated. The Mass Mean Diameter and the Rosin-Rammler parameter \bar{x} are two other diameters that are often used in analyzing the performance of atomizers. In order to allow readers to calculate mean diameters other than the SMD a few distributions which represent the typical states of the atomization will be numerically tabulated in this section. The distributions will be taken from the plotted distributions in this report.

Diameters (microns)	Mean Bin Diameter (microns)	Volumetric Distributions			
		Fig. 11c solid line	Fig. 11d solid line	Fig. 13a solid line	Fig. 24 dashed line
7-15	11	0.059	0.230	0.367	0.299
15-20	17.5	0.103	0.157	0.228	0.029
20-25	22.5	0.144	0.105	0.229	0.152
25-30	27.5	0.169	0.087	0.058	0.198
30-35	32.5	0.172	0.093	0.041	0.132
35-40	37.5	0.148	0.103	0.046	0.022
40-50	45	0.101	0.100	0.057	0.068
50-60	55	0.043	0.071	0.047	0.065
60-75	67.5	0.034	0.024	0.020	0.024
75-100	87.5	0.021	0.027	0.013	0.019
SMD(microns)		27.2	20.9	17.0	19.8

Diameters	Fig. 26c dashed line	Fig. 27a dotted line	Fig. 28b solid line	Fig. 35a solid line	Fig. 35b dashed line	Fig. 35c dotted line
7-15	0.011	0.337	0.320	0.296	0.055	0.468
15-20	0.158	0.251	0.051	0.037	0.158	0.179
20-25	0.243	0.171	0.134	0.144	0.178	0.027
25-30	0.205	0.103	0.191	0.202	0.092	0.105
30-35	0.084	0.055	0.138	0.154	0.047	0.076
35-40	0.044	0.028	0.039	0.056	0.151	0.0001
40-50	0.105	0.017	0.040	0.027	0.160	0.057
50-60	0.069	0.010	0.052	0.048	0.069	0.055
60-75	0.009	0.004	0.019	0.023	0.026	0.019
75-100	0.072	0.024	0.017	0.012	0.064	0.013
SMD	27.3	16.8	19.1	19.6	27.3	15.9

Diameters	Volumetric Distributions				
	Fig. 37a solid line	Fig. 37d dotted line	Fig. 45 dashed line	Fig. 46c dotted line	Fig. 47a solid line
7-15	0.004	0.336	0.479	0.369	0.044
15-20	0.044	0.070	0.222	0.100	0.163
20-25	0.102	0.116	0.026	0.092	0.232
25-30	0.162	0.107	0.074	0.162	0.222
30-35	0.200	0.132	0.082	0.126	0.148
35-40	0.192	0.037	0.035	0.040	0.053
40-50	0.129	0.040	0.018	0.033	0.014
50-60	0.030	0.053	0.037	0.048	0.020
60-75	0.052	0.023	0.021	0.022	0.023
75-100	0.086	0.015	0.007	0.009	0.080
SMD	33.7	18.7	15.4	17.8	25.2

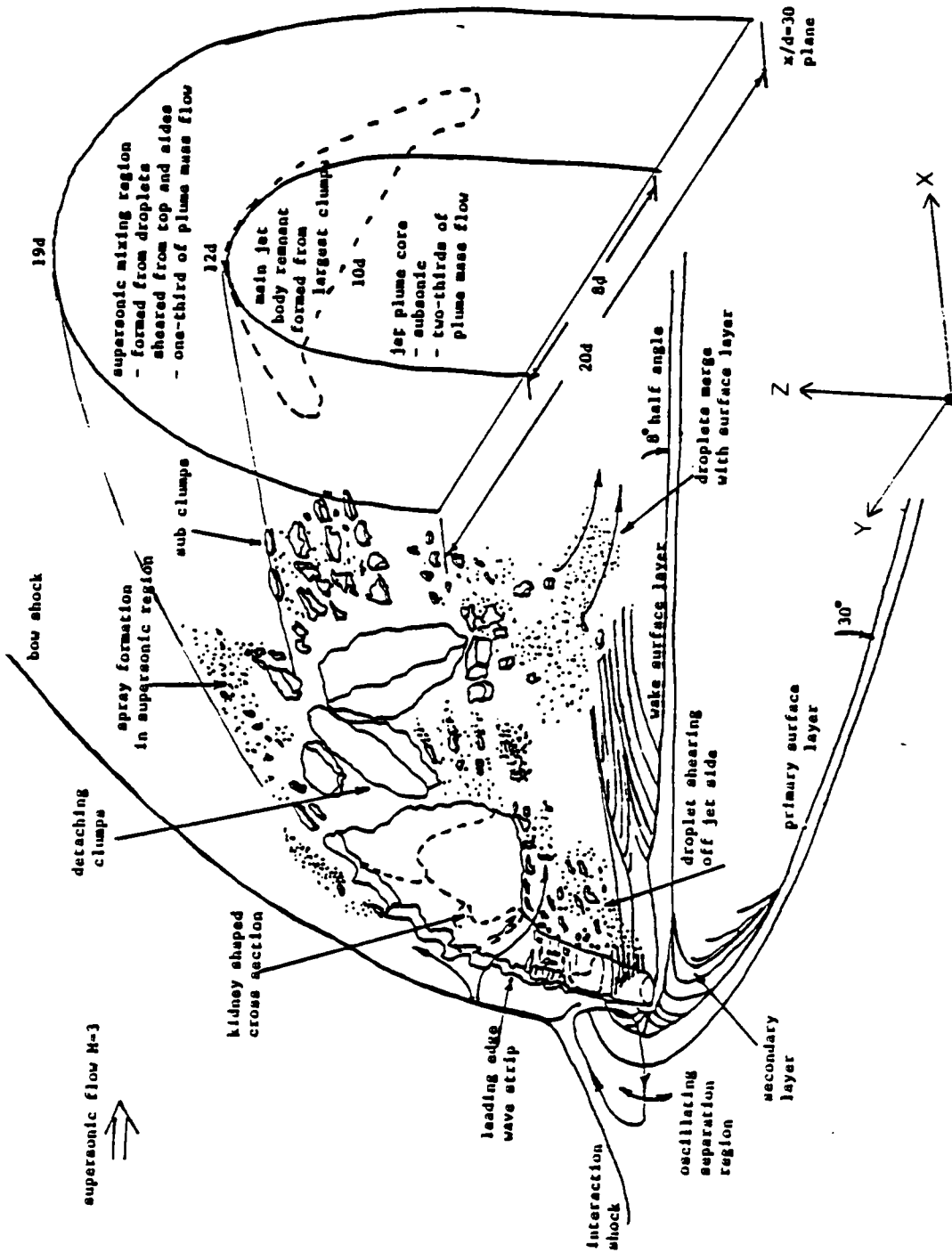


FIGURE 1

SCHMATIC OF LIQUID INJECTION INTO SUPERSONIC CROSSFLOW
(from Thomas Ref. 39)

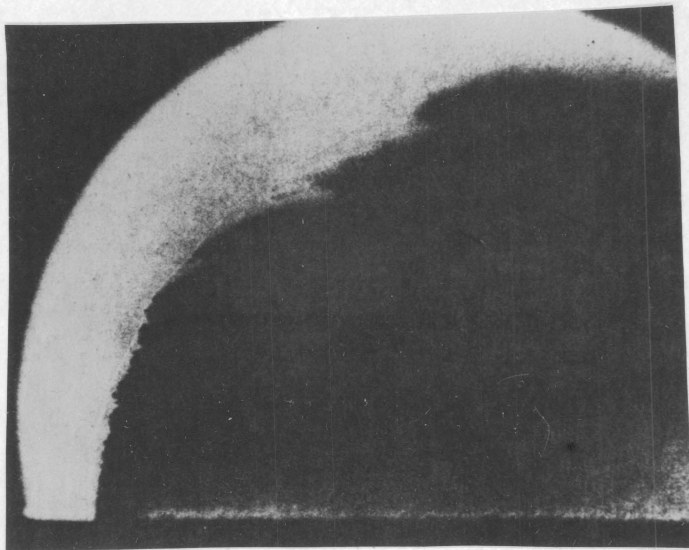


FIGURE 2
STOP-ACTION VIEW OF LIQUID JET IN SUPERSONIC FLOW
(from Nejad Ref 49)

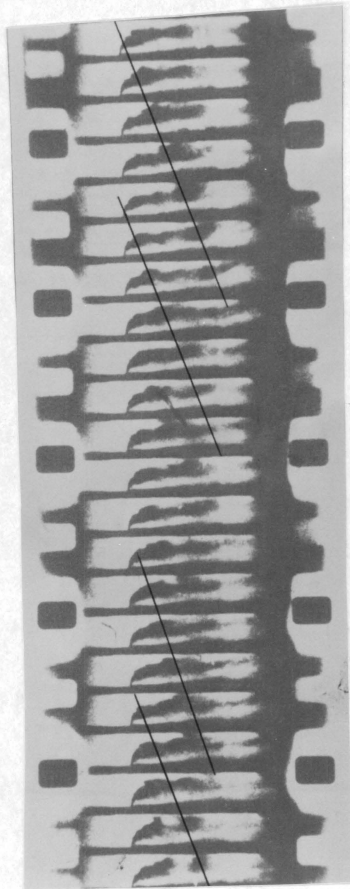


FIGURE 3
HIGH-SPEED MOVIE OF LIQUID JET IN SUPERSONIC FLOW
Water; $q=14.0$; $M_\infty=4$; 36000 frames per second
(from Kush and Schetz Ref. 46)

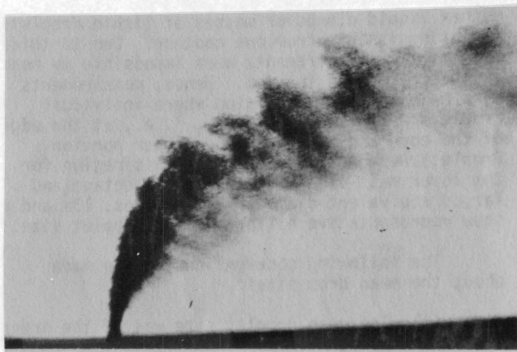


FIGURE 4

STOP-ACTION VIEW OF LIQUID JET IN SUBSONIC FLOW
(from Padye and Schetz Ref. 36)

Water; $q=2.06$; $M=0.45$; 0.8 microsecond flash

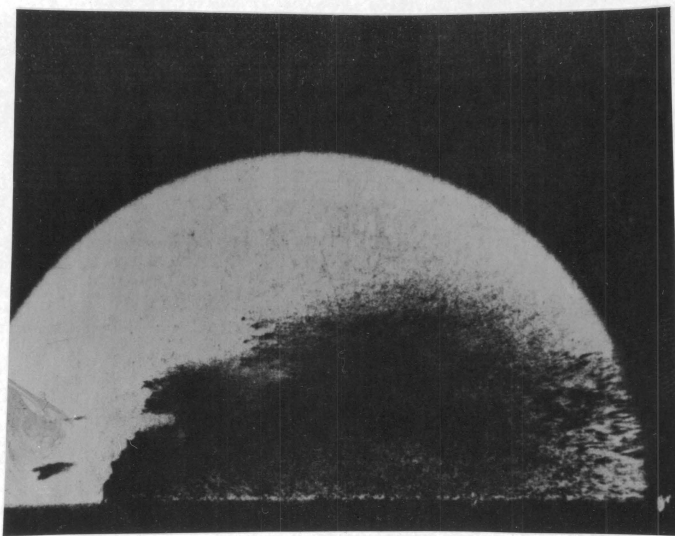


FIGURE 5
EXAMPLE OF REGIME 1 JET
Water/Glycerine; $\bar{q}=2$; $M_w=3.0$
(from Nejad Ref. 49)

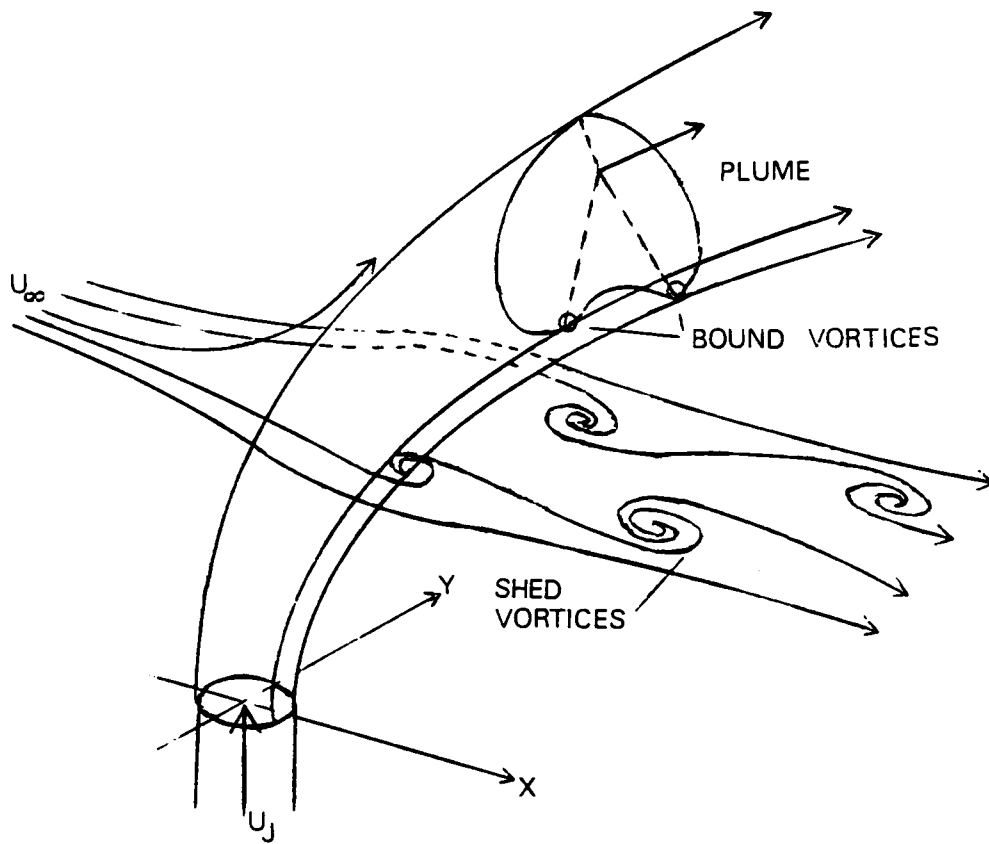


FIGURE 6
SCHEMATIC OF AIR INJECTION INTO AN AIR CROSSFLOW

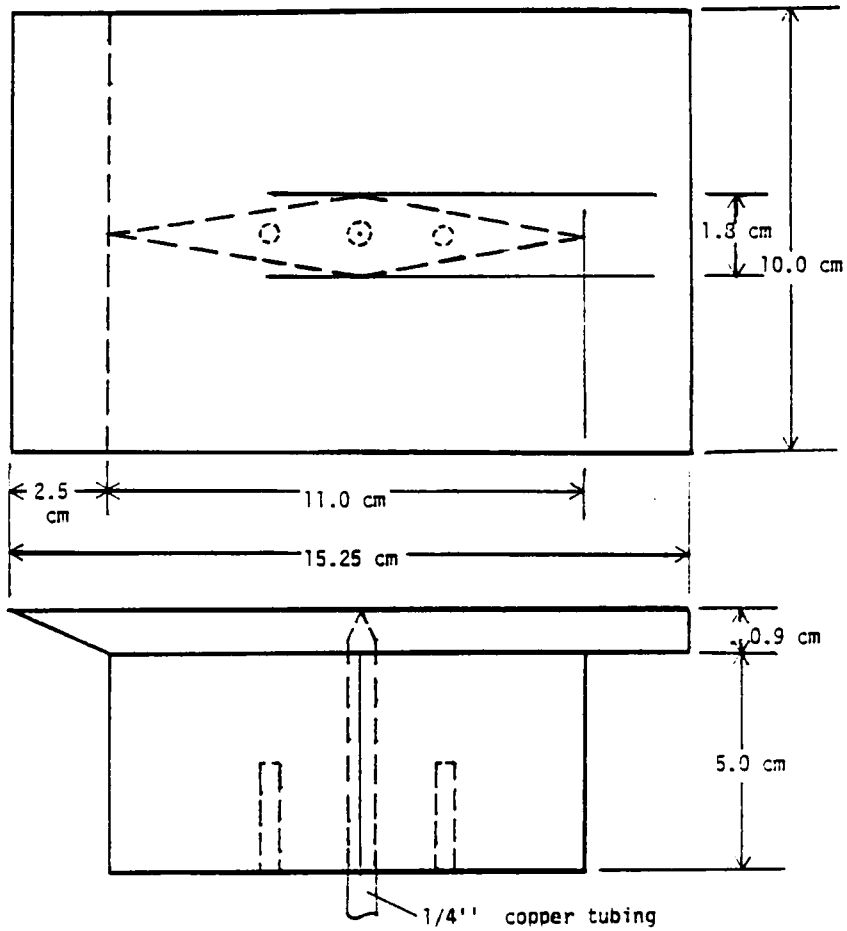


FIGURE 7
SCHEMATIC OF FLAT PLATE MODEL

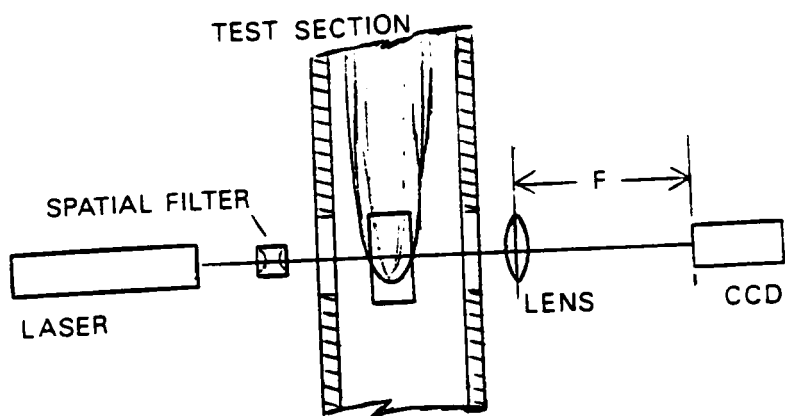


FIGURE 8
SCHEMATIC OF OPTICAL ARRANGEMENT

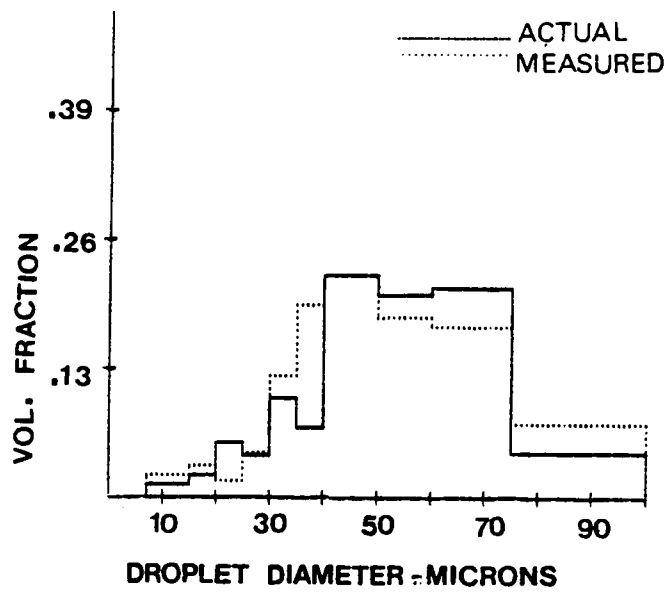


FIGURE 9
CALIBRATION RETICLE SIZE DISTRIBUTION

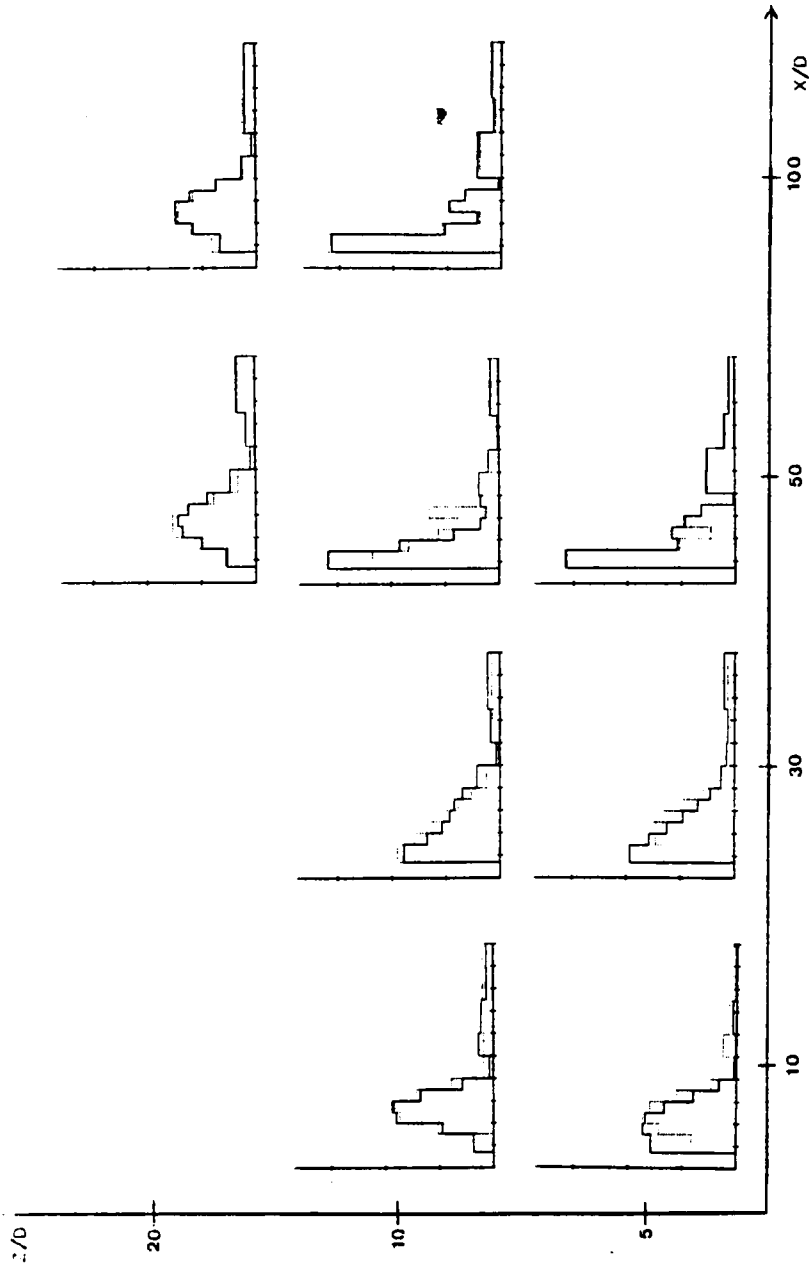


FIGURE 10

DROPLET SIZE DISTRIBUTIONS FOR WATER JET IN SUPersonic FLOW

Water; $q=10$; $M_\infty=0.48$; 0.35 msec Exposure Time

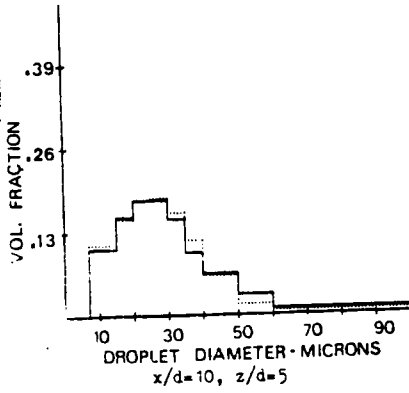


Figure 11a

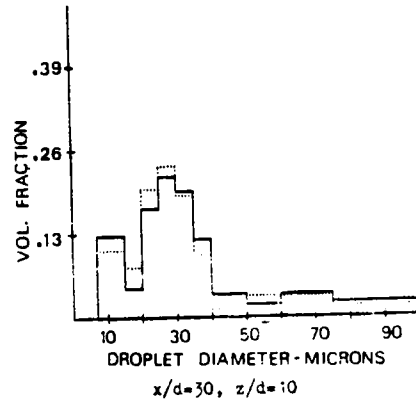


Figure 11b

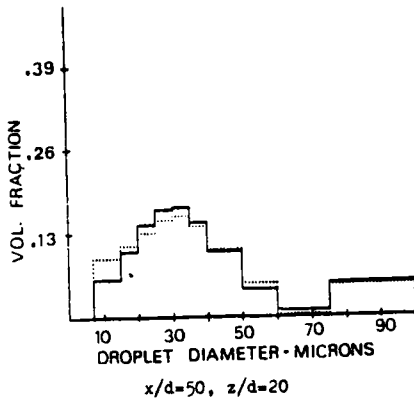


Figure 11c

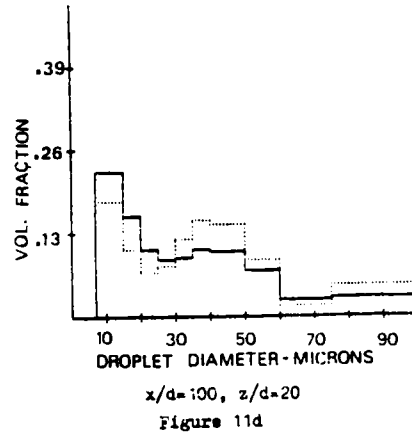


Figure 11d

FIGURE 11
DROPLET SIZE DISTRIBUTIONS FOR VARIOUS x/d
Water; $\bar{q}=10$; $M_{\infty}=0.48$; 3.5 msec Exposure

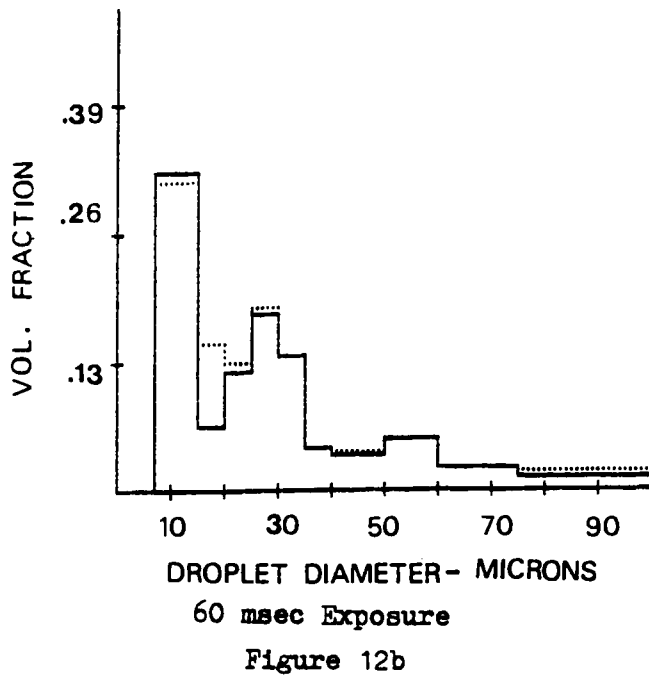
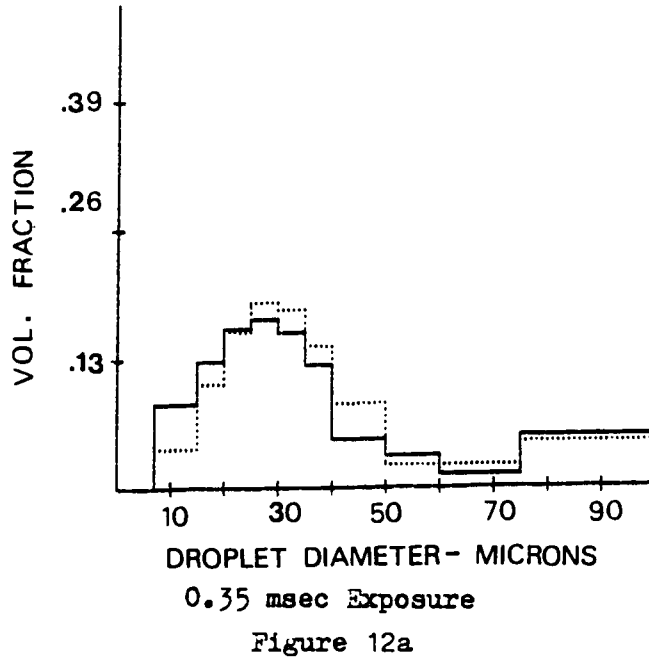


FIGURE 12
 DISTRIBUTIONS FOR VARIOUS EXPOSURE TIMES AT $x/d=100$, $z/d=20$
 Water; $\bar{q}=10$; $M_{\infty}=0.48$

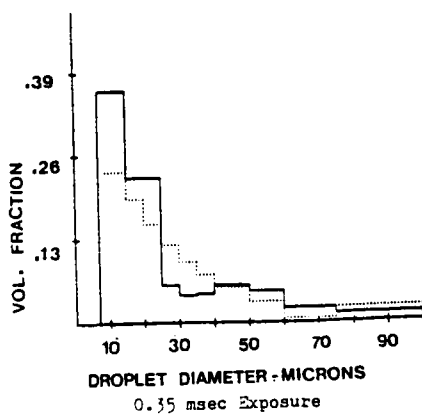


Figure 13a

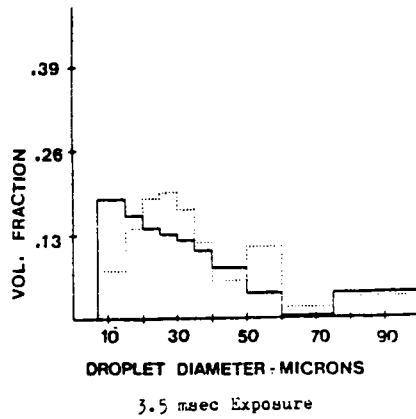


Figure 13b

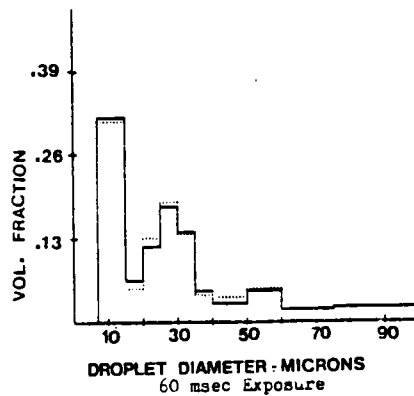


Figure 13c

FIGURE 13
 DISTRIBUTIONS AT VARIOUS EXPOSURE TIMES AT $x/d=50$, $z/d=10$
 Water; $\bar{q}=10$; $M_{\infty}=0.48$;

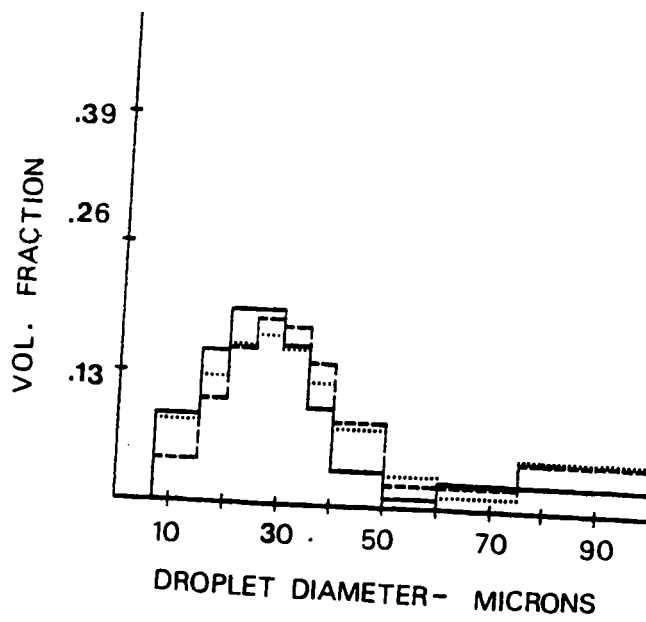


FIGURE 14
 VARIATIONS IN DISTRIBUTIONS AT $x/d=100$, $z/d=20$
 Water; $q=10$; $M=0.48$; 0.35 msec Exposure

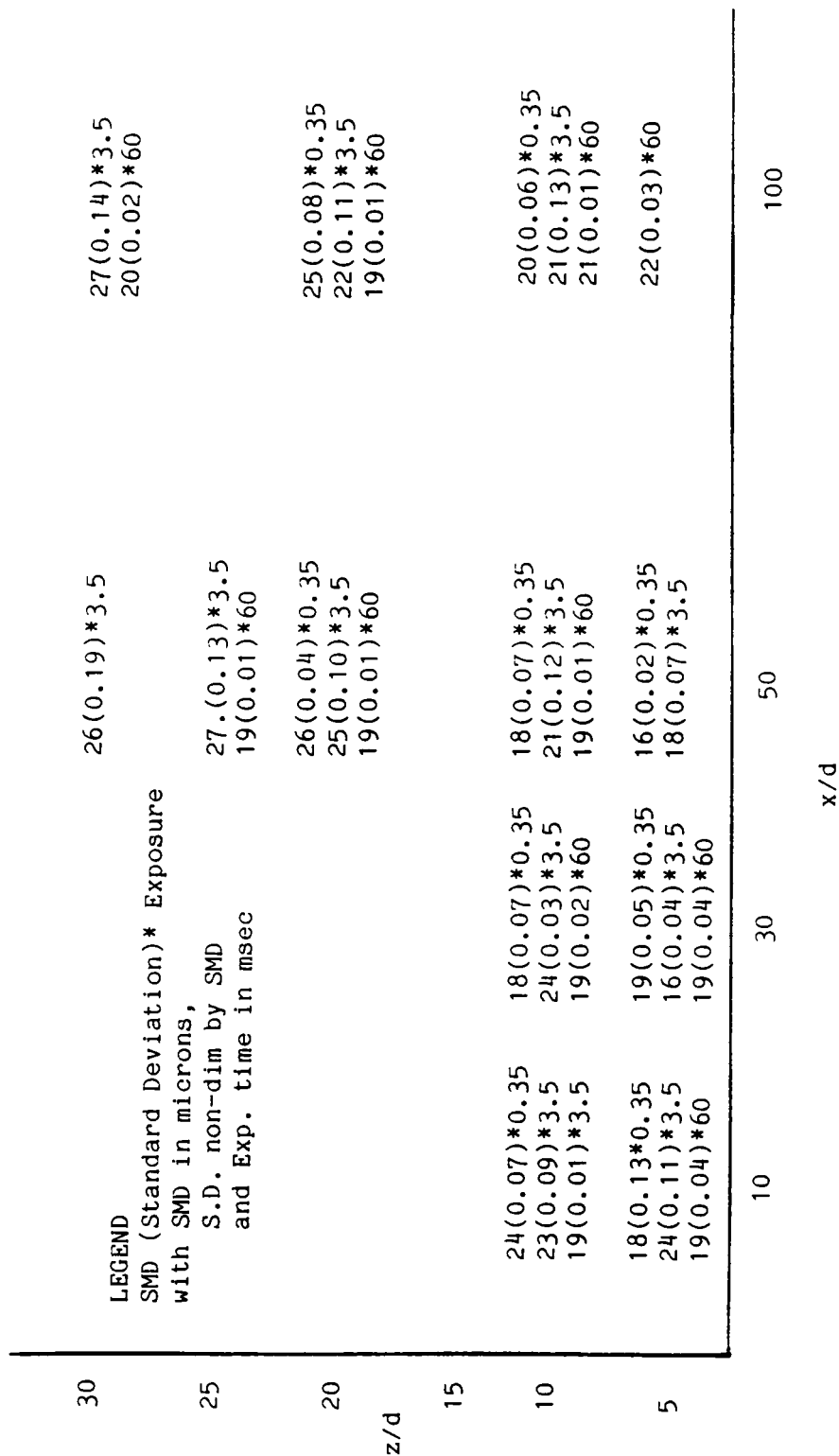


FIGURE 15

PLOT OF SMD FOR WATER JET IN SUBSONIC FLOW

Water; $\bar{q}=10$; $M_\infty=0.48$

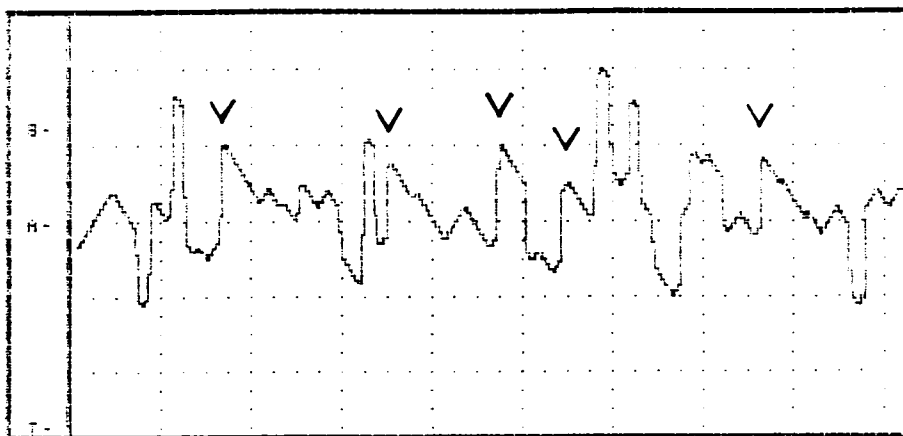


Figure 16a

$x/d=40$, $z/d=5$ 0.032 msec per division

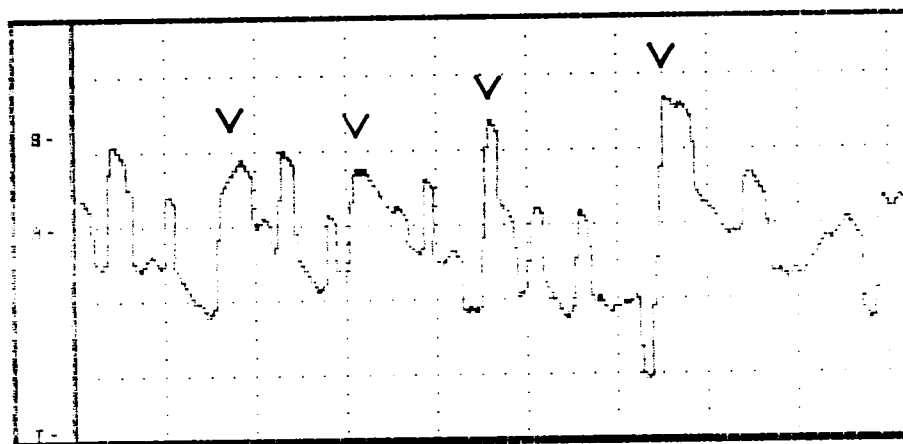


Figure 16b

$x/d=100$, $z/d=20$ 0.032 msec per division

FIGURE 16

EXAMPLES OF EXTINCTION TIME TRACES

Water; $\bar{q}=10$; $M_\infty=0.48$

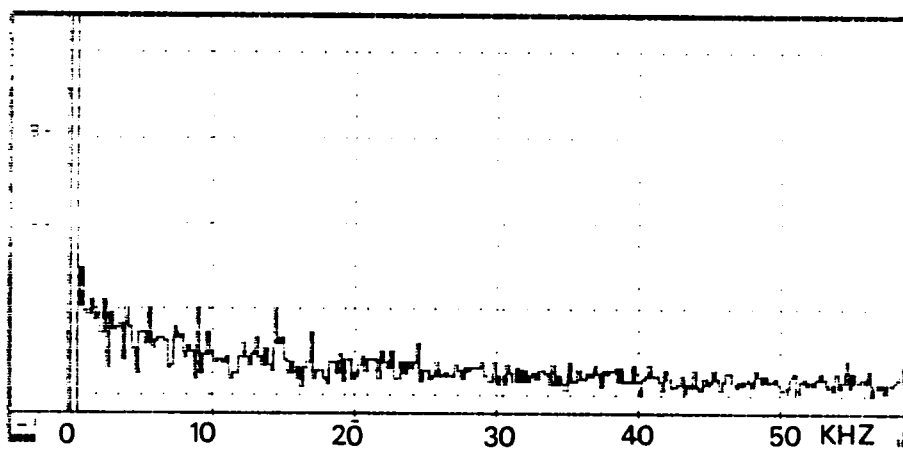


FIGURE 17
FREQUENCY SPECTRUM AT $x/d=20$, $z/d=5$
Water; $\bar{q}=10$; $M_\infty=0.48$

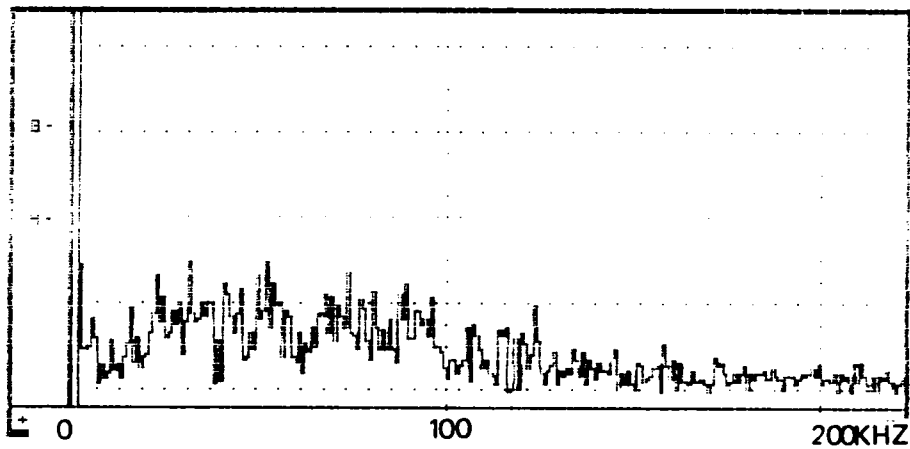


FIGURE 18
FREQUENCY SPECTRUM AT $x/d=100$, $z/d=25$
Water; $\bar{q}=10$; $M_{\infty}=0.48$

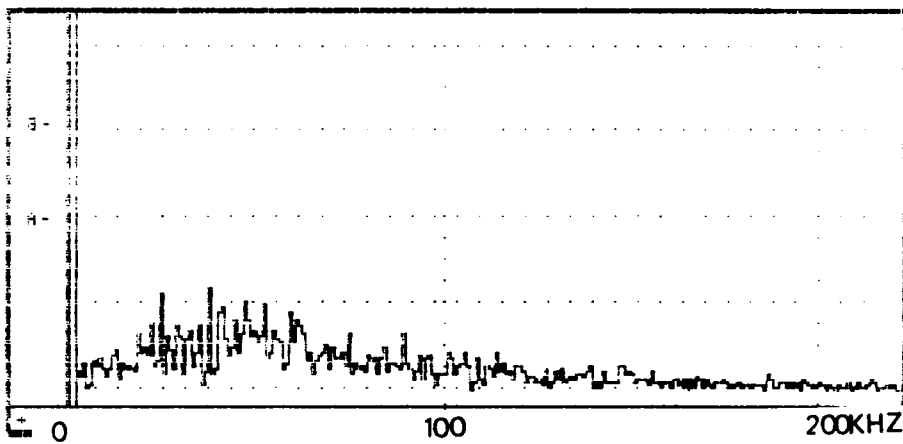


FIGURE 19
FREQUENCY SPECTRUM AT $x/d=100$, $z/d=5$
Water; $\bar{q}=10$; $M_o=0.48$



FIGURE 20

CROSS SECTION OF WATER JET AT $x/d=100$ Water; $\bar{q}=10$; $M_\infty=0.48$; 1/50 second shutter

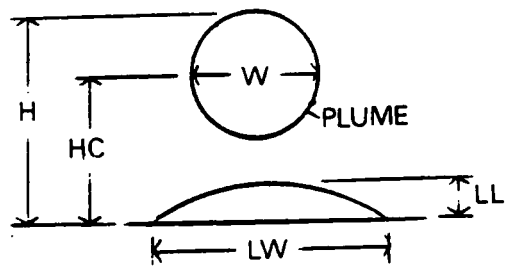


FIGURE 21
SCHEMATIC OF CROSS SECTION OF JET

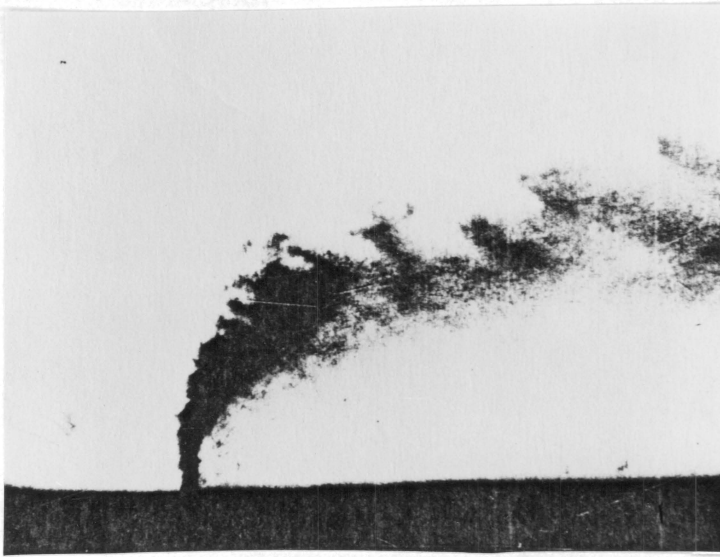


FIGURE 22
BREAKUP OF WATER JET IN SUBSONIC FLOW
(from Padye and Schetz Ref 36)

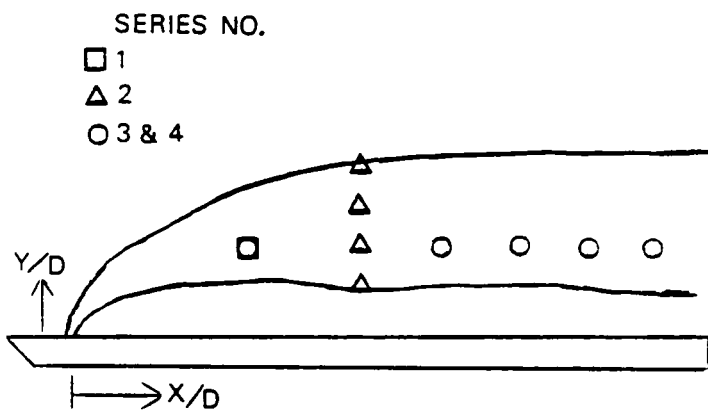


FIGURE 23
LOCATIONS OF MEASUREMENTS WITHIN JET PLUME
Water/Methanol Jet

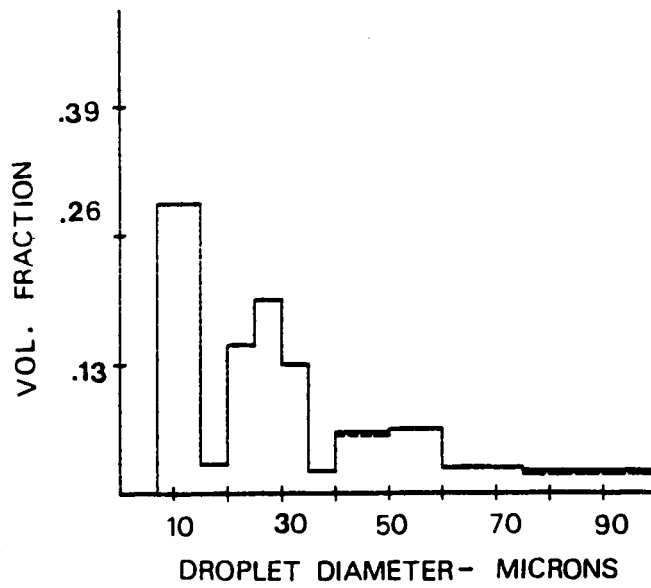


FIGURE 24
DISTRIBUTIONS AT 25 MSEC EXPOSURE TIME
Water/Methanol; $\bar{q}=12$; $M_{\infty}=3$

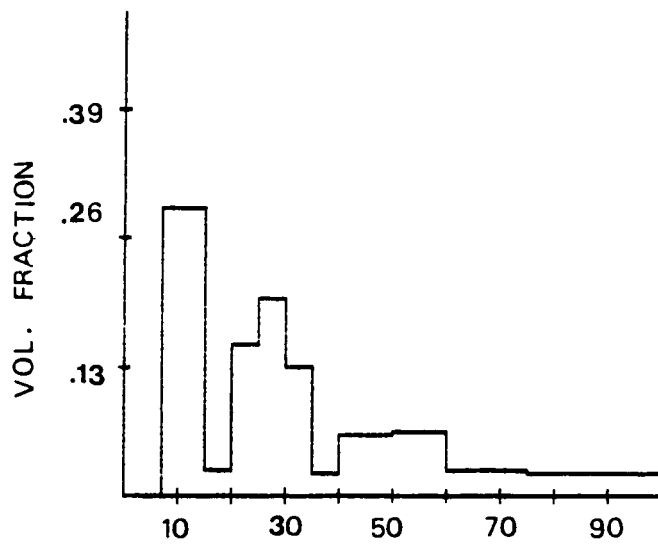


FIGURE 25

DISTRIBUTIONS AT 5 MSEC EXPOSURE TIME

Water/Methanol; $\bar{q}=12$; $M_{\infty}=3$

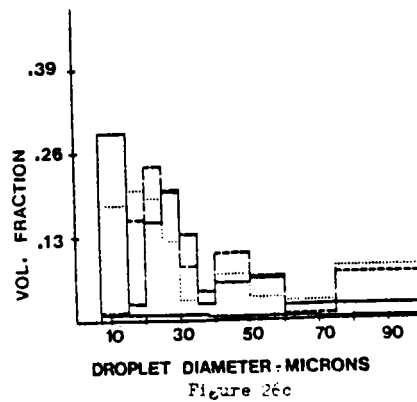
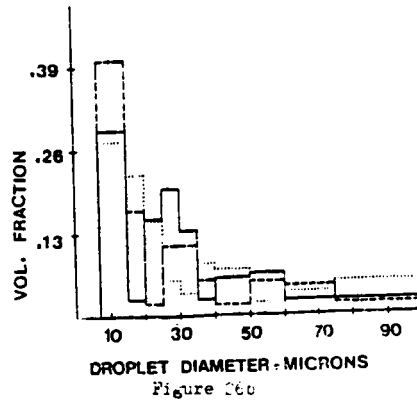
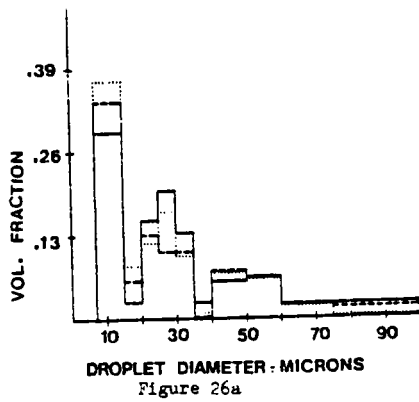


FIGURE 26
DISTRIBUTIONS AT 2.5 MSEC EXPOSURE TIME
Water/Methanol; $\bar{q}=12$; $M_{\infty}=3$

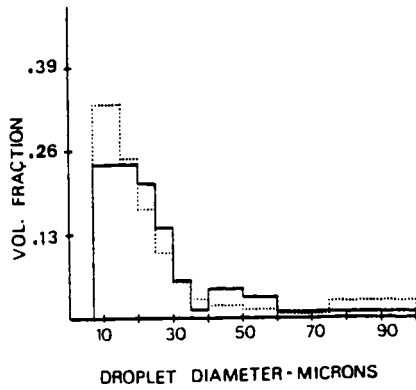


Figure 27a

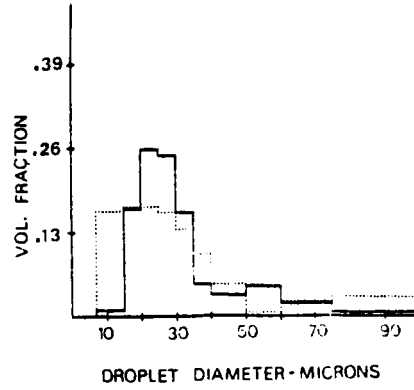


Figure 27b

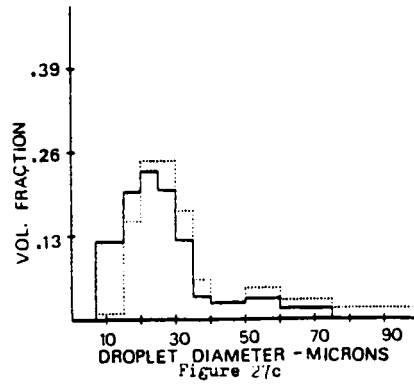


Figure 27c

FIGURE 27
DISTRIBUTIONS AT 0.65 MSEC EXPOSURE TIME
Water/Methanol; $\bar{q}=12$; $M=3$

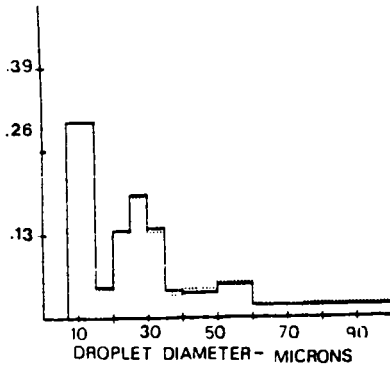


Figure 28a

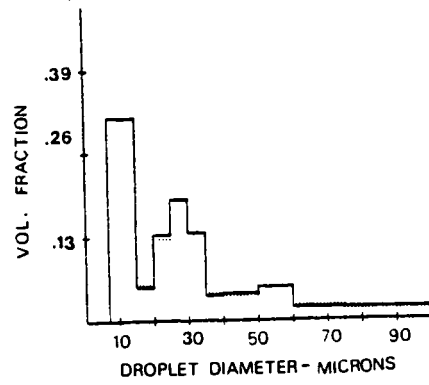


Figure 28b

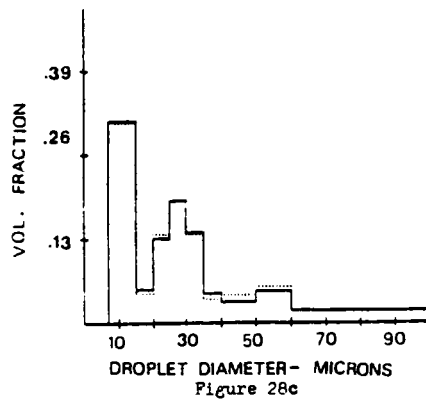


Figure 28c

FIGURE 28
DISTRIBUTIONS AT 0.225 MSEC EXPOSURE TIME
Water/Methanol; $\bar{q}=12$; $M_{\infty}=3$

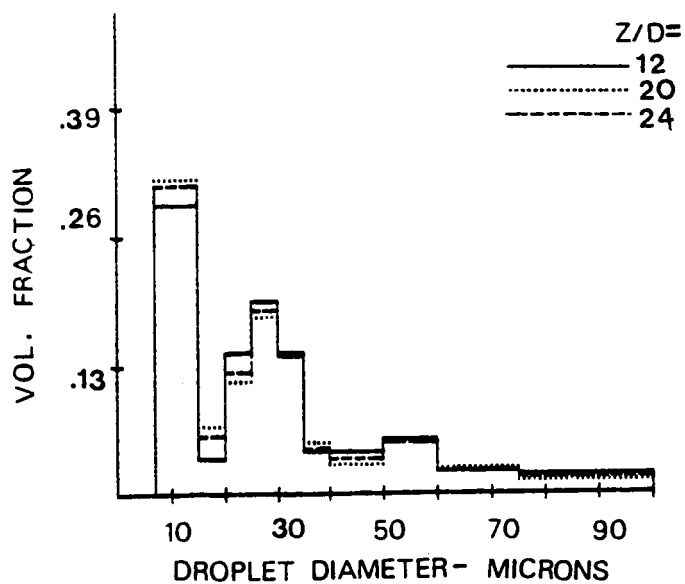


FIGURE 29

DISTRIBUTIONS AT VARIOUS z/d Water/Methanol; $\bar{q}=12$; $M_{\infty}=3$; 0.225 msec Exposure

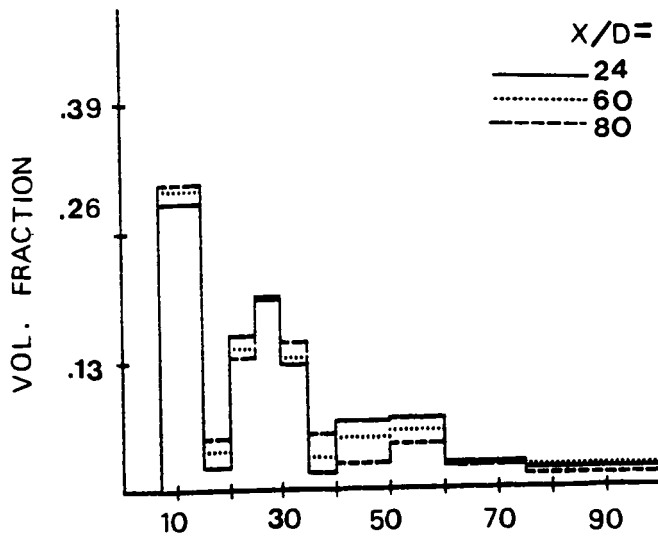


FIGURE 30

DISTRIBUTIONS AT VARIOUS x/d FOR HIGH \bar{q} JET
 Water/Methanol; $\bar{q}=12$; $M_{\infty}=3$; 0.3msec Exposure

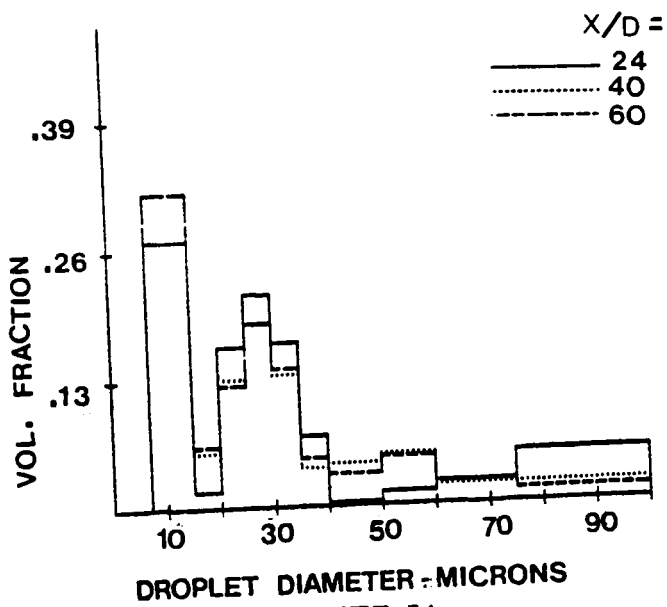


FIGURE 31

DISTRIBUTIONS AT VARIOUS x/d FOR LOW \bar{q} JET
 Water/Methanol; $\bar{q}=4$; $M_{\infty}=3$; 0.3 msec Exposure

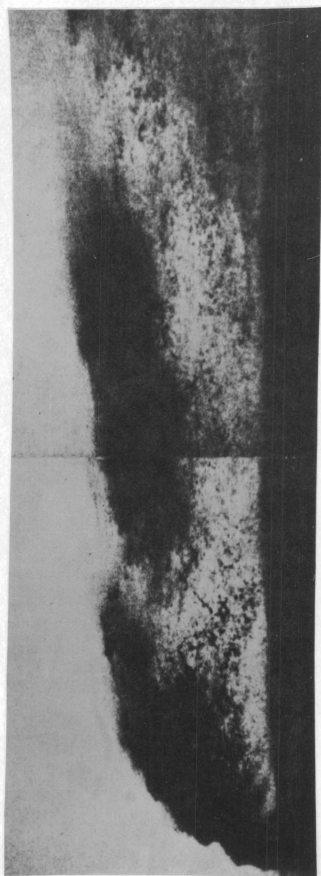
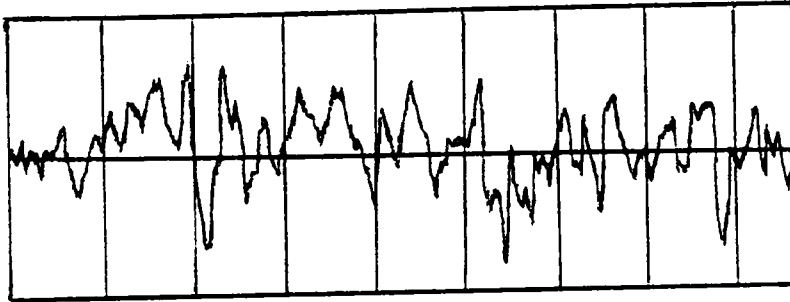
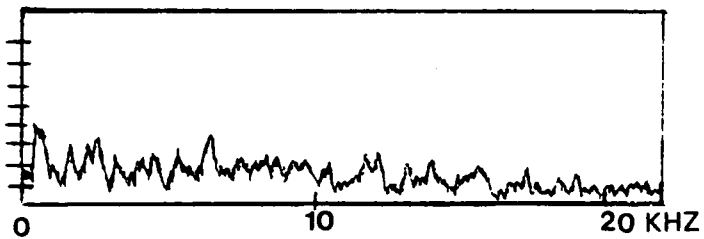


FIGURE 32

STOP-ACTION VIEW OF A LOW \bar{q} JET
Water; $\bar{q}=3.8$; $M_\infty=2.4$; 1 microsecond flash
(from Kush and Schetz Ref 46)



Extinction Time Trace 0.25 msec per division



Fast Fourier Transform of Time Trace

FIGURE 33

EXAMPLES OF EXTINCTION DATA FOR WATER/METHANOL JET
 Water/Methanol; $\bar{q}=12$; $M_p=3$; $x/d=24$, $z/d=12$

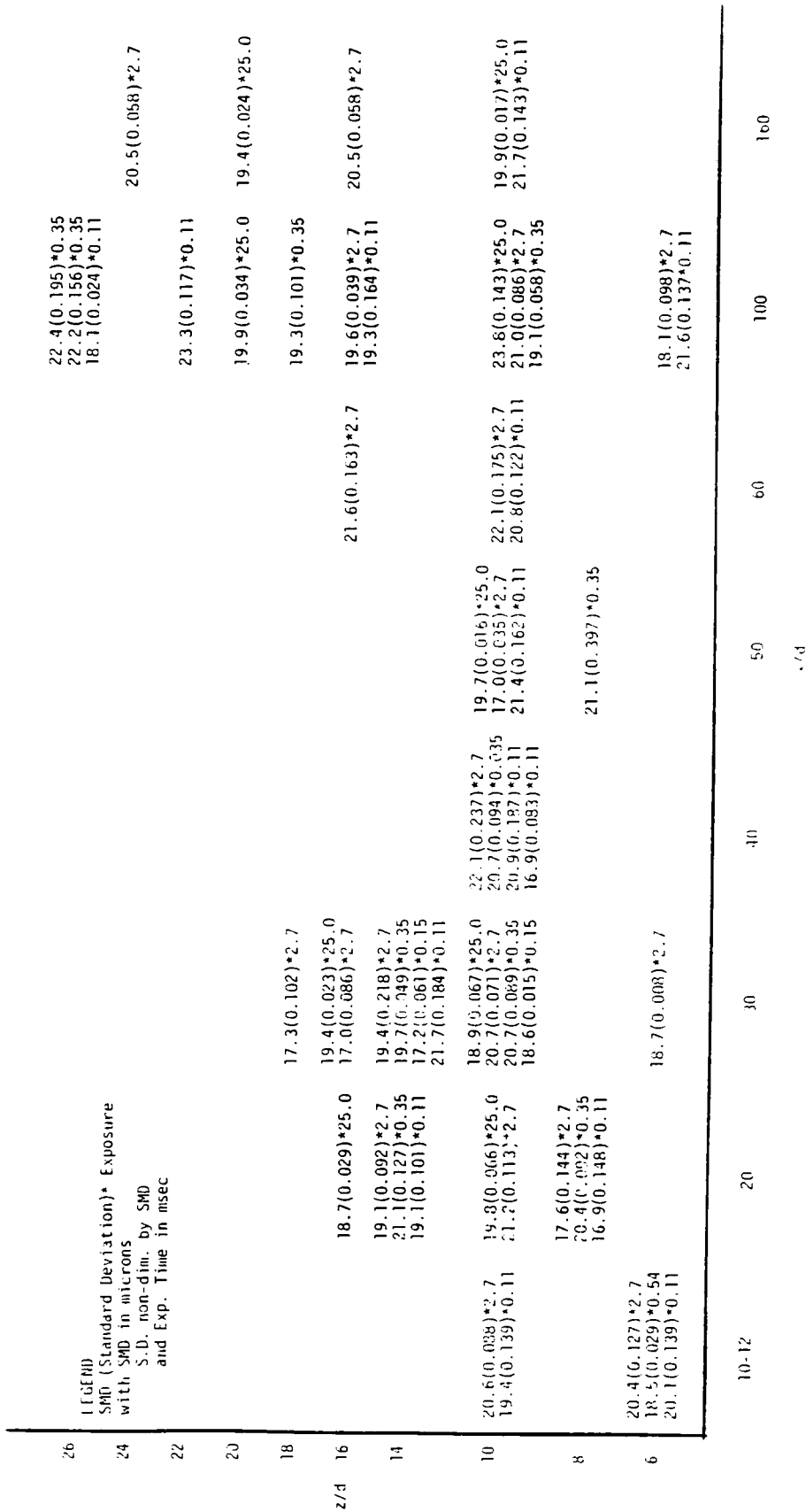
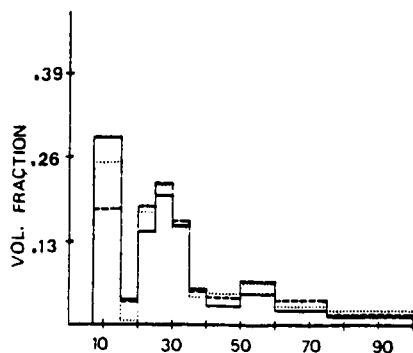


FIGURE 34

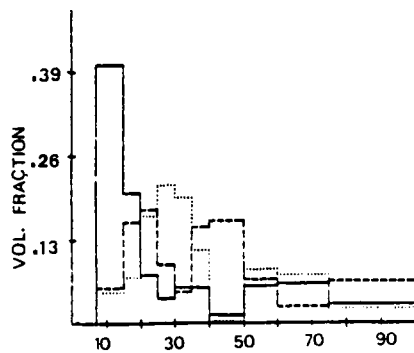
PLOT OF SMD FOR HIGH \bar{q} WATER JET IN SUPERSONIC FLOWWater; $\bar{q}=10$; $M_\infty=3$



DROPLET DIAMETER - MICRONS

 $x/d=30$

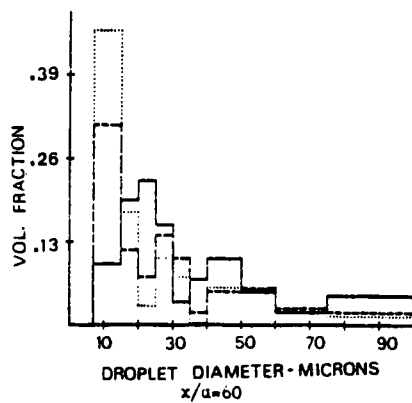
Figure 35a



DROPLET DIAMETER - MICRONS

 $x/d=40$

Figure 35b

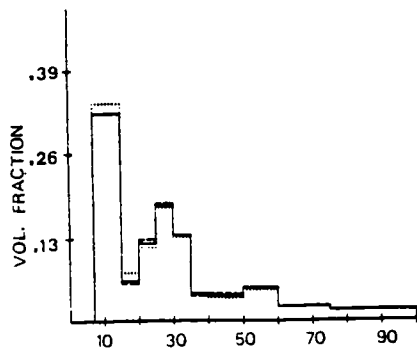


DROPLET DIAMETER - MICRONS

 $x/d=60$

Figure 35c

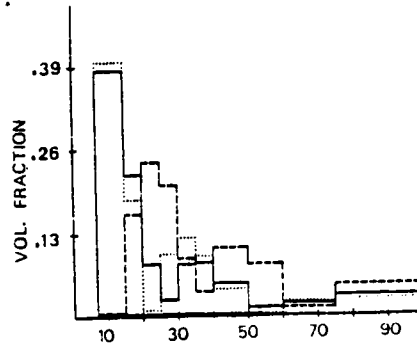
FIGURE 35
DISTRIBUTIONS AT VARIOUS x/d
Water; $\bar{q}=10$; $M_{\infty}=3$; 2.7 msec Exposure



DROPLET DIAMETER - MICRONS

 $z/d=6$

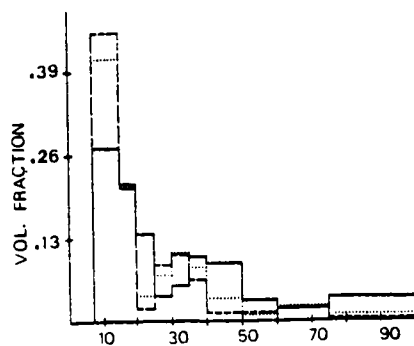
Figure 36a



DROPLET DIAMETER - MICRONS

 $z/d=14$

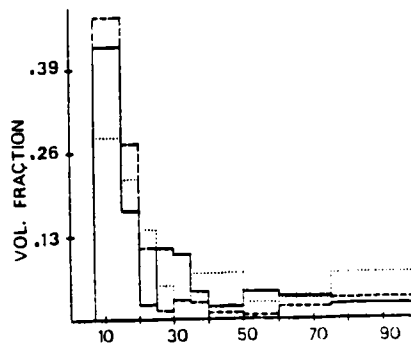
Figure 36b



DROPLET DIAMETER - MICRONS

 $z/d=16$

Figure 36c



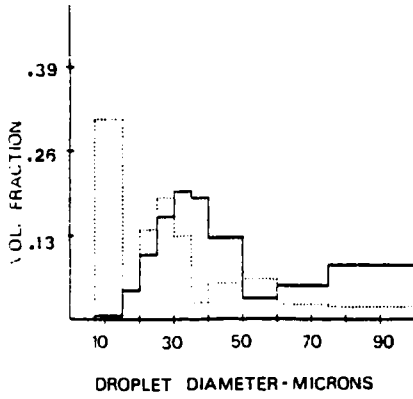
DROPLET DIAMETER - MICRONS

 $z/d=18$

Figure 36d

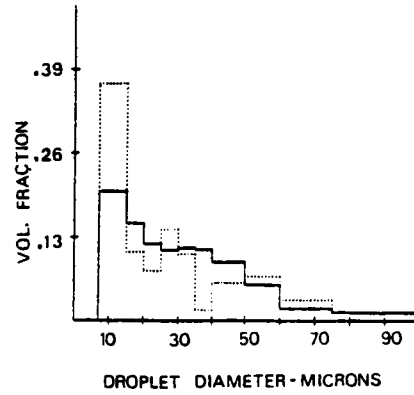
FIGURE 36

DISTRIBUTIONS AT VARIOUS z/d Water; $\bar{q}=10$; $M_w=3$; 2.7 msec Exposure



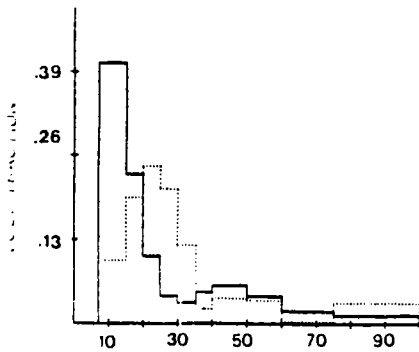
$x/d=30, z/d=14$

Figure 37a



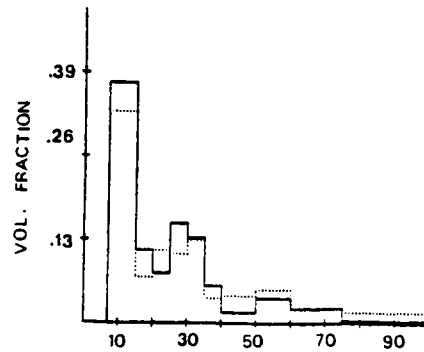
$x/d=50, z/d=10$

Figure 37b



$x/d=100, z/d=6$

Figure 37c



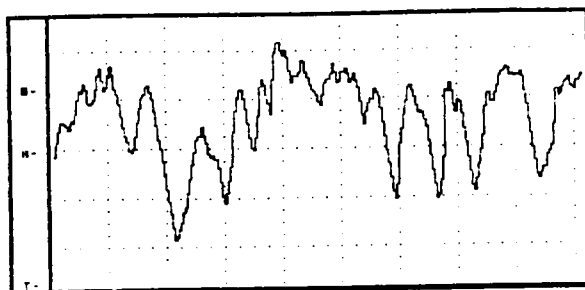
$x/d=100, z/d=26$

Figure 37d

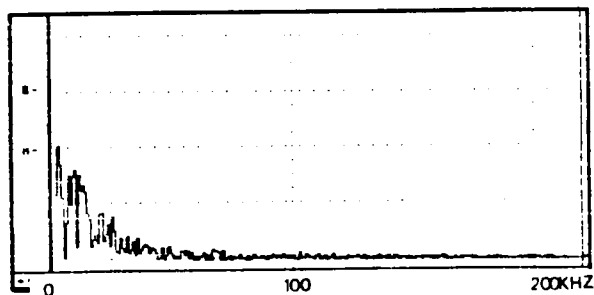
FIGURE 37

VARIOUS DISTRIBUTIONS AT 0.11 MSEC EXPOSURE

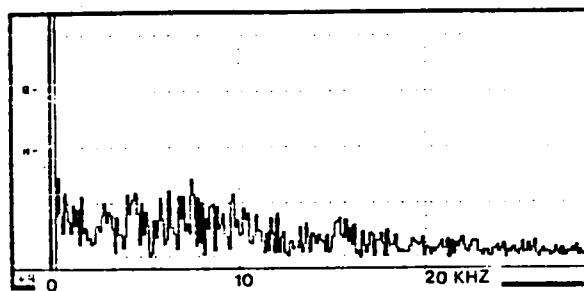
Water; $\bar{q}=10$; $M_{\infty}=3.0$



Extinction Time Trace
0.032 msec per division



Wide Range Fast Fourier Transform
Figure 38b

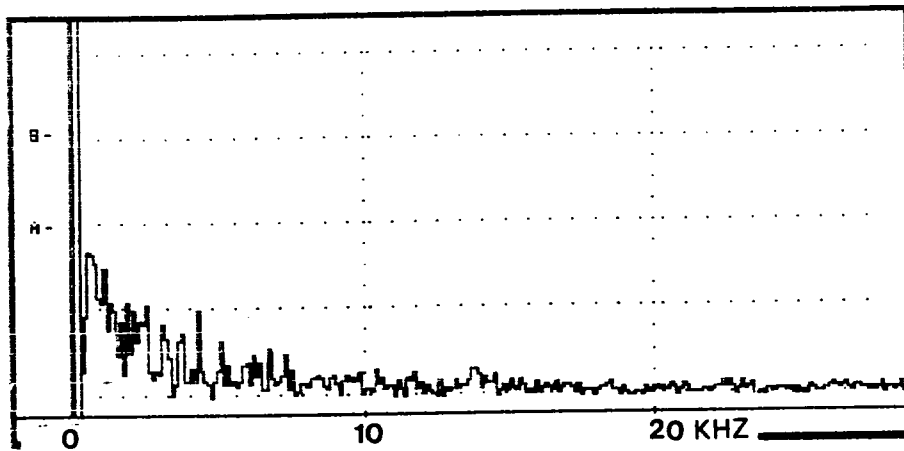


Regular Range Fast Fourier Transform
Figure 38c

FIGURE 38

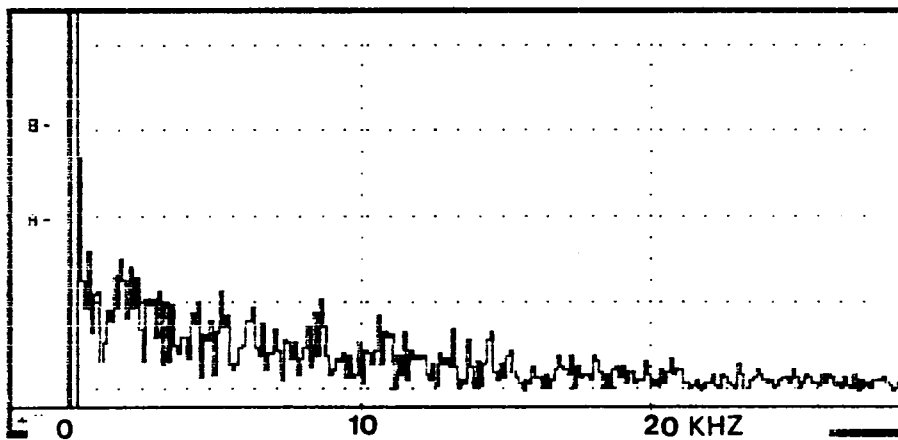
EXAMPLES OF EXTINCTION DATA

Water; $\bar{q}=10$; $M_{\infty}=3$; $x/d=40$, $z/d=10$



$x/d=5, z/d=5$

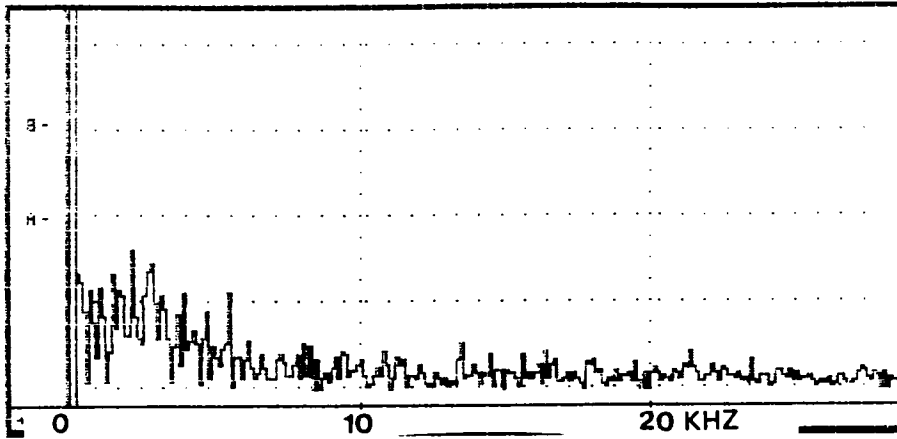
Figure 39a



$x/d=10, z/d=15$

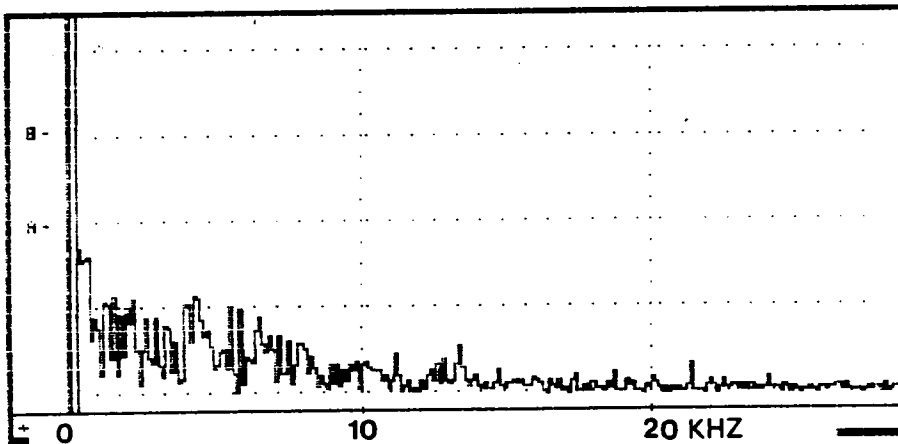
Figure 39b

FIGURE 39
FREQUENCY SPECTRUMS CLOSE TO INJECTOR
Water; $\bar{q}=10$; $M_{\infty}=3$



$x/d=100, z/d=10$

Figure 40a



$x/d=100, z/d=40$

Figure 40b

FIGURE 40
FREQUENCY SPECTRUM AT VARIOUS z/d
Water; $\bar{q}=10$; $M_\infty=3$

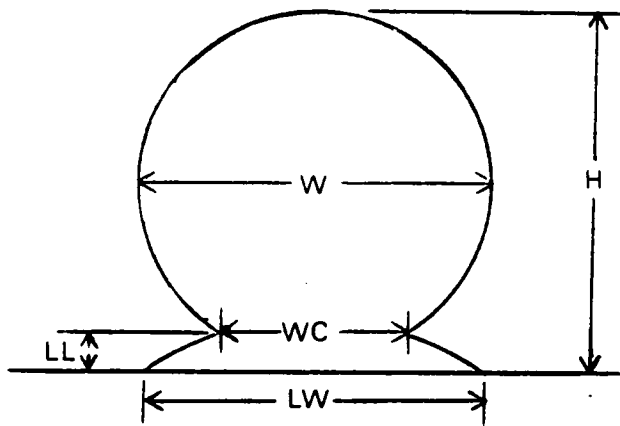


FIGURE 41
SCHEMATIC OF CROSS SECTION OF JET

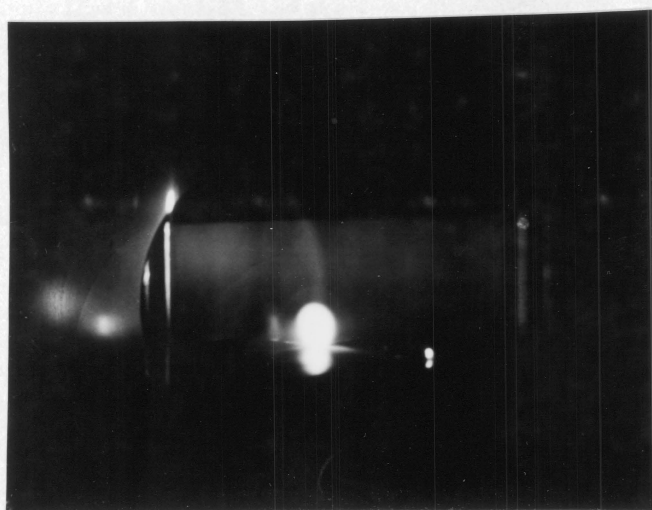


FIGURE 42

CROSS SECTION OF WATER JET AT $x/d=100$ Water; $\bar{q}=10$; $M_\phi=3$; 1 second shutter

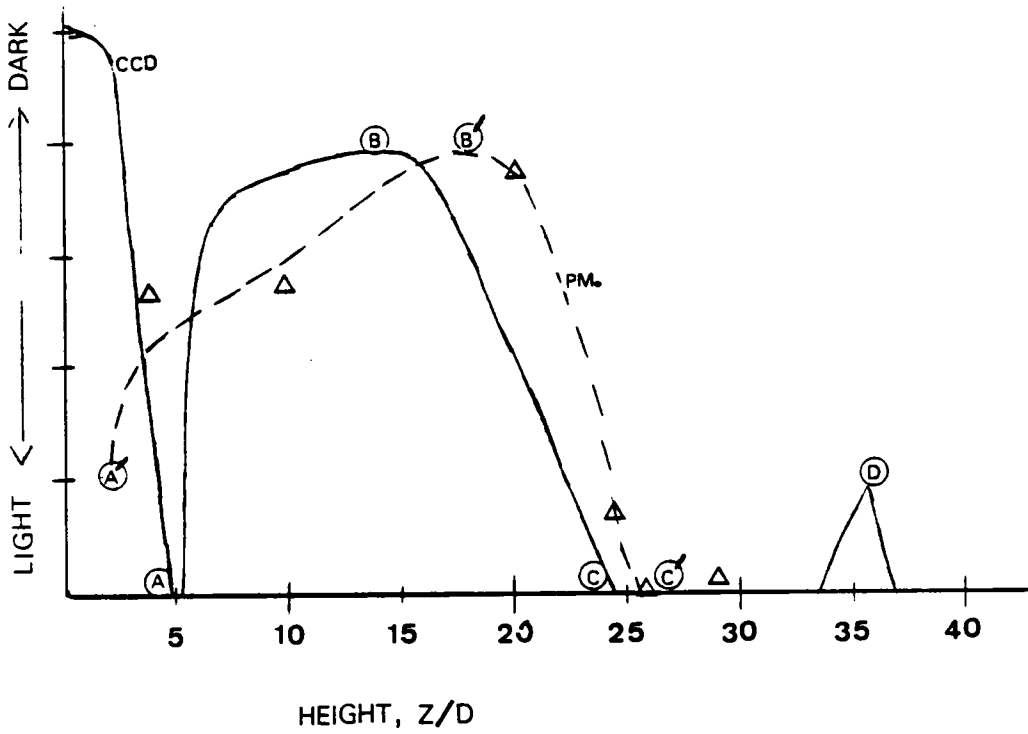


FIGURE 43

EXAMPLE OF CCD PENETRATION RESULT

Water; $\bar{q}=10$; $M_c=3$; 4.1 msec Exposure CCD; $x/d=40$

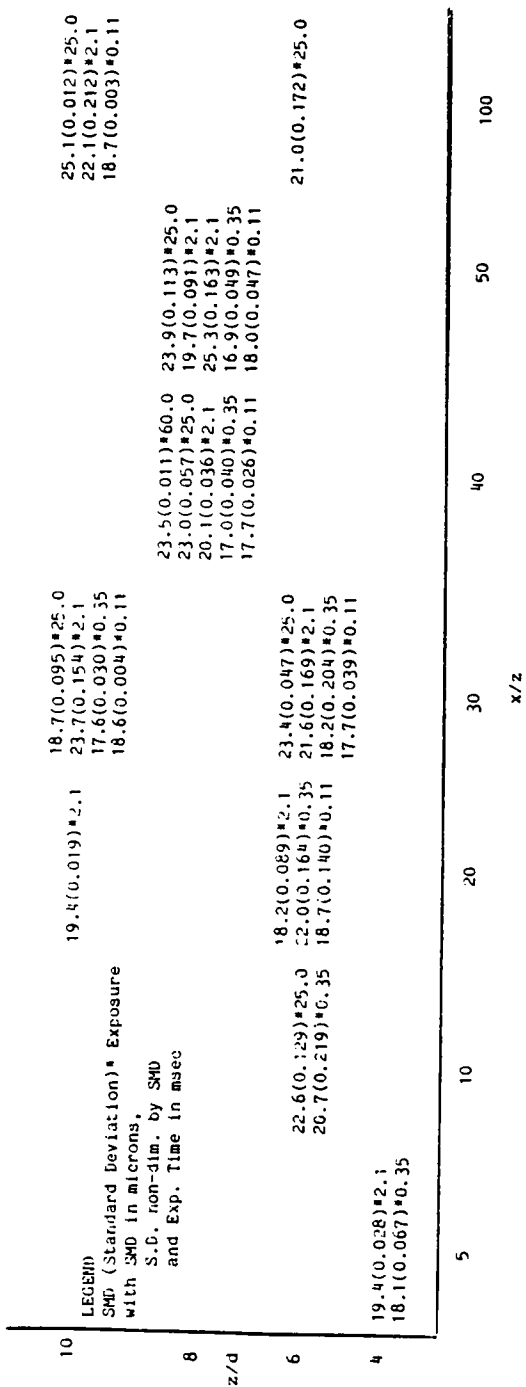


FIGURE 44

PLOT OF SMD FOR LOW \bar{q} WATER JET SUPERSONIC FLOW

Water; $\bar{q}=4$; $M_\infty=3$

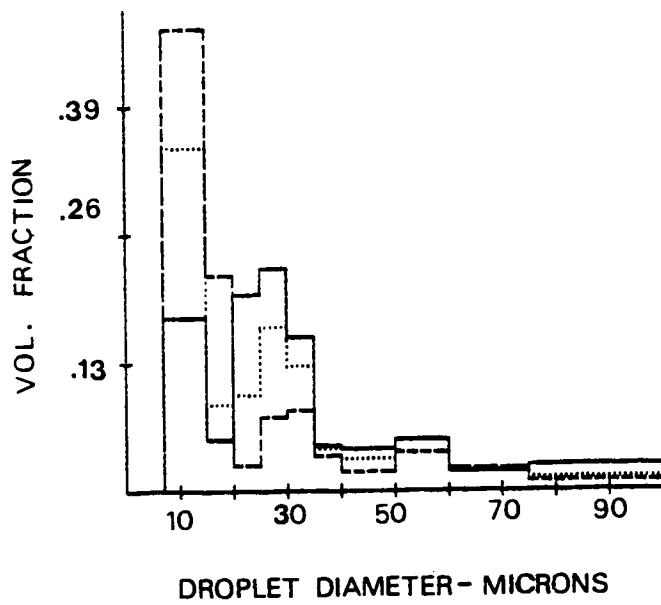


FIGURE 45
 VARIATIONS IN DISTRIBUTIONS AT $x/d=20$, $z/d=6$
 Water; $\bar{q}=4$; $M_{\infty}=3$; 0.11 msec Exposure

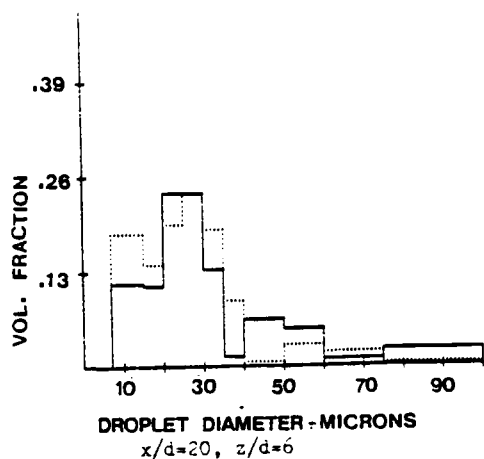


Figure 46a

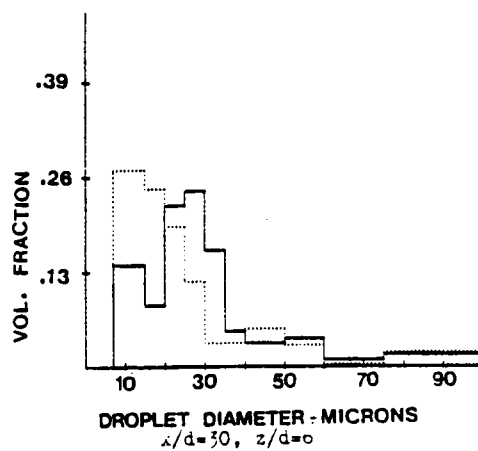


Figure 46b

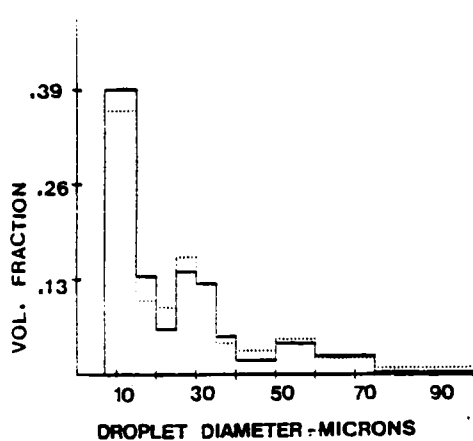


Figure 46c

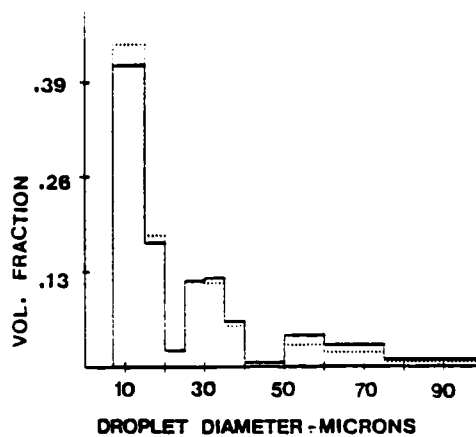
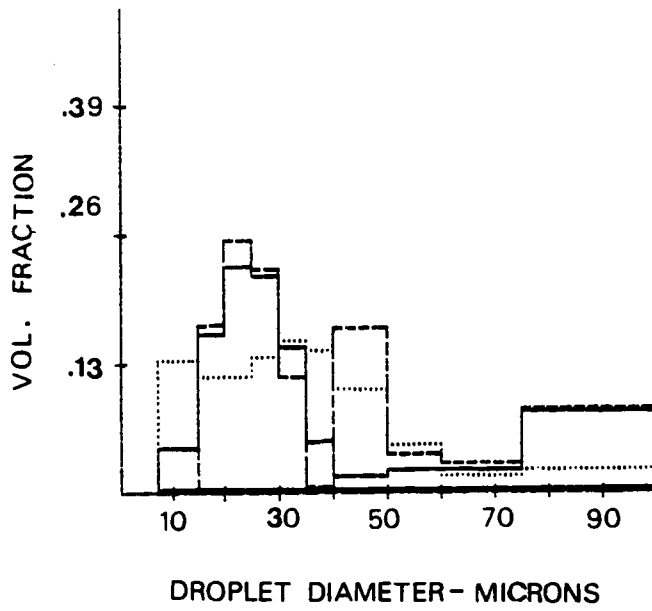


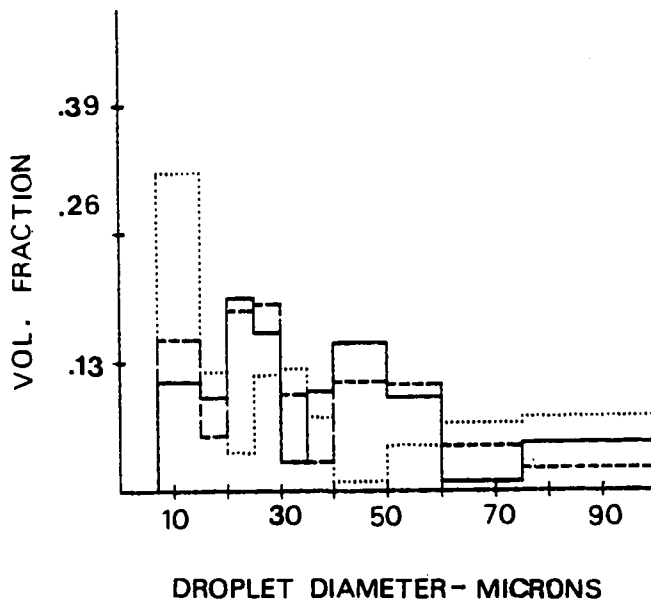
Figure 46d

FIGURE 46
DISTRIBUTIONS AT VARIOUS x/d
Water; $\bar{q}=4$; $M_a=3$; 0.35 msec Exposure



$x/d=30, z/d=6$

Figure 47a



$x/d=30, z/d=10$

Figure 47b

FIGURE 47

DISTRIBUTIONS AT VARIOUS z/d

Water; $\bar{q}=4$; $M_{\infty}=3$; 2.1 msec Exposure

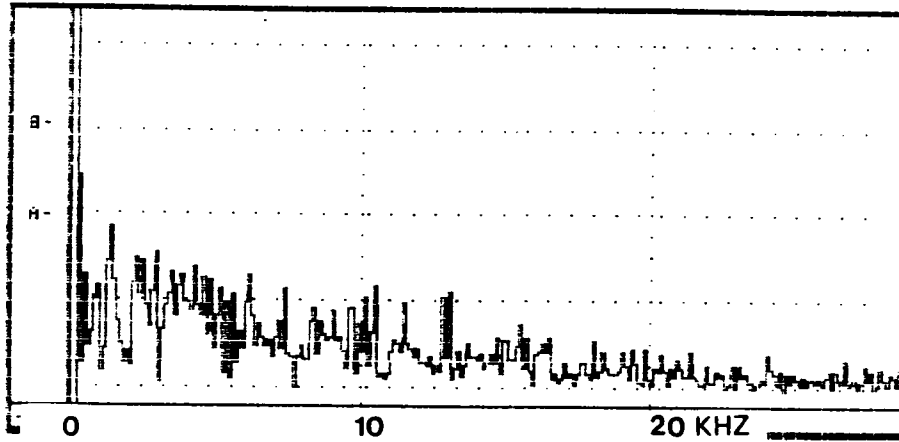


Figure 48a
 $x/\bar{d}=40$, $z/\bar{d}=10$

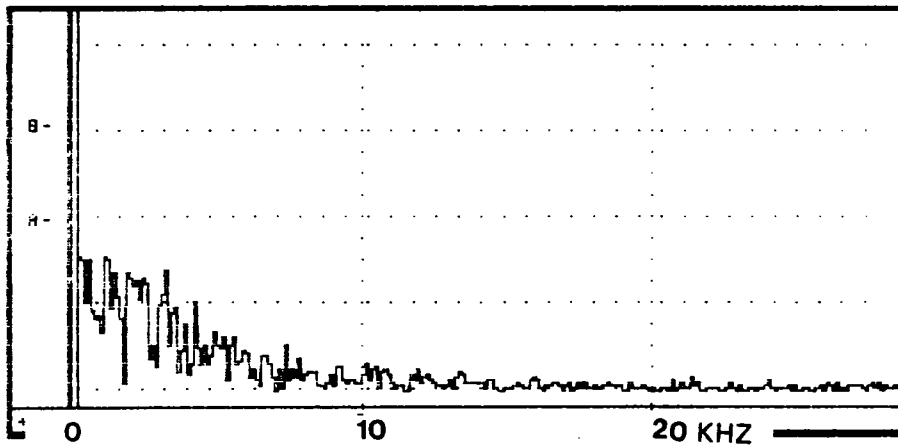


Figure 48b
 $x/\bar{d}=100$, $z/\bar{d}=10$

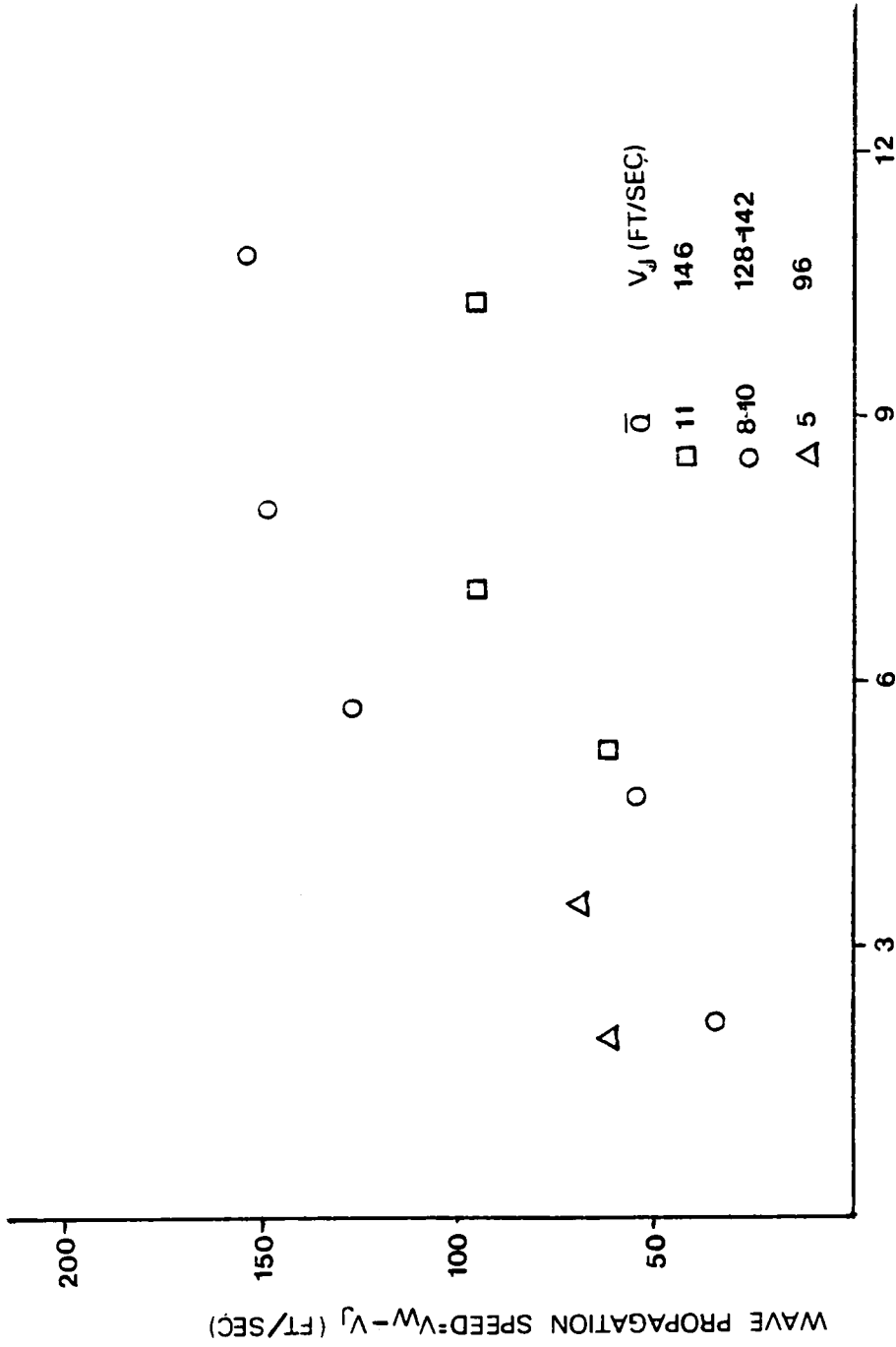
FIGURE 48
 EXAMPLES OF FREQUENCY SPECTRUMS
 Water; $\bar{q}=4$; $M_\infty=3$



FIGURE 49

CROSS SECTION OF WATER JET AT $x/d=200$ Water; $\bar{q}=4$; $M_\infty=3$; 1 second shutter

OLD COUNCIL TREE
BOND
100% COTTON FIBER



ARC LENGTH ALONG JET COLUMN IN JET DIAMETERS

FIGURE 50

JET COLUMN WAVE PROPAGATION SPEED

(from Kush and Schetz Ref 46)

Water; $M = 2.4$; 0.79 mm orifice

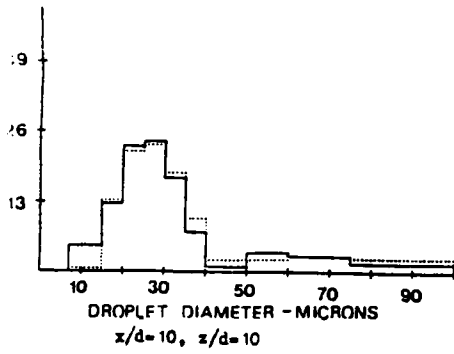


Figure 51a

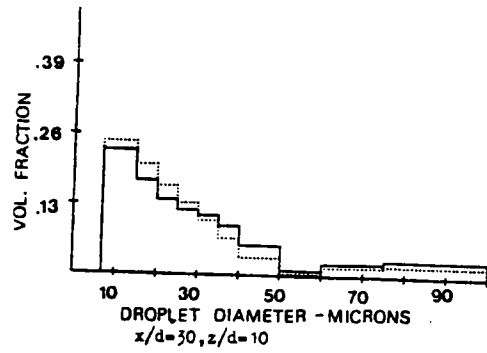


Figure 51b

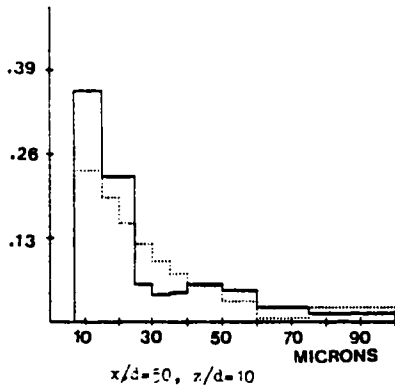


Figure 51c

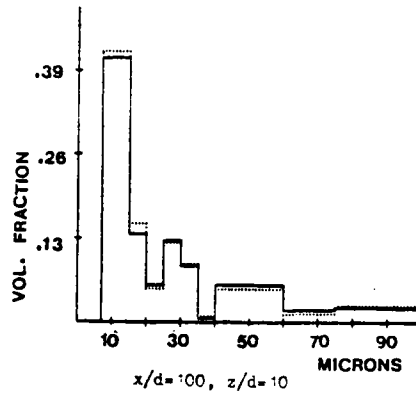
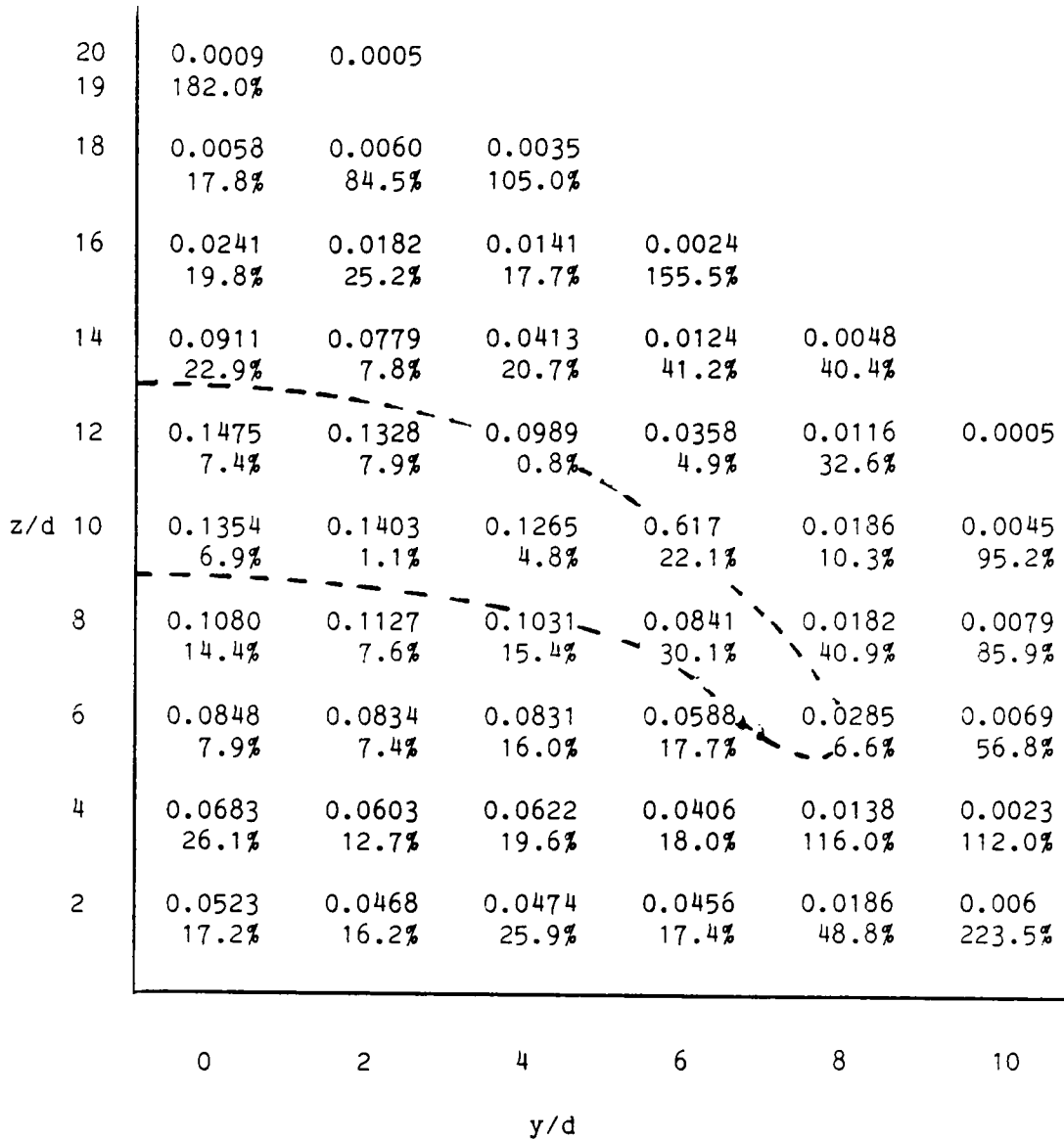


Figure 51d

FIGURE 51

ATOMIZATION OF WATER JET IN SUBSONIC CROSSFLOW

Water; $\bar{q}=10$; $M_\infty=0.48$; 0.35 msec Exposure



Liquid flow in gram/sec-mm²; percent spread in sampling data

FIGURE 52

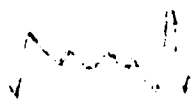



MASS SAMPLING SURVEY OF WATER JET

Water; $\bar{q}=6$; $M_{\infty}=3$; 5 second sampling time
(from Thomas, Ref. 39)

TABLE 1
TIME HISTORIES OF SMD FOR WATER JET
IN SUBSONIC FLOW

Exposure Time(msec)	x/d, z/d	Time History of SMD (microns)
0.35	10, 5	15.5, 16.1/ 18.9, 22.0/ 19.8, 17.8
0.35	10, 10	24.9, 26.8/ 23.6, 26.6/ 24.2, 21.3
0.35	30, 10	17.6, 16.5/ 18.5, 17.3/ 19.8, 18.8
0.35	50, 10	15.8, 17.7/ 17.0, 19.5/ 18.9, 17.0
0.35	100, 10	19.2, 25.2/ 19.4, 21.0/ 23.8, 20.9/ 22.7, 21.8/ 23.1, 18.3/ 20.2, 18.7/ 18.3, 16.9

TABLE 2
FREQUENCY OF THE EXTINCTION PATTERN

$x/d, z/d$	Frequency (kHz)	Pattern
40, 5	14.2	
100, 5	15.8	
100, 10	14.0	
100, 20	33.0	

Water; $\bar{q}=10$; $M_\infty=0.48$

TABLE 3
VERTICAL LOCATION OF MAXIMUM TRANSIENTS

x/d	z/d	h/d	y/h	Maximum Value of the Standard Deviation of SMD
10	5	18	0.28	0.13
30	10	24	0.33	0.07
50	10	28	0.36	0.12
50	25	28	0.89	0.13
50	30	28	1.07	0.19
100	10	34	0.29	0.13
100	20	34	0.59	0.11
100	30	34	0.89	0.14

x/d	z/d	h/d	y/h	Highest Observed Frequency (kHz)
20	5	22	0.23	25
50	5	28	0.18	140
50	20	28	0.71	110
100	5	34	0.15	90
100	25	34	0.74	125

Water; $\bar{q}=10$; $M_{\infty}=0.48$

TABLE 4
PLUME DIMENSIONS OF WATER JET IN SUBSONIC FLOW

x/d	H/d	W/d	HC/d	LL/d	LW/d
10	20	20	?	?	?
20	24	18	11	<1	18
	17*	13*	11*	<1*	18*
50	31	29	19	3	29
	23*	20*	19*	2*	27*
100	37	38	20	2	33
	26*	26*	20*	2*	32*

* Refers to region of maximum intensity on the photographs

Water; $\bar{q}=10$; $M_\infty=0.48$

TABLE 5

MEAN AND STANDARD DEVIATION OF SMD FOR VARIOUS EXPOSURE TIMES

Exposure Time(msec)	Set #	SMD (microns)	Standard Deviation of SMD
25.0	1	19.7	0.001
5.0	1	18.4	0.09
	2	18.5	0.09
	3	18.3	0.10
	average	18.4	0.09
2.5	1	18.7	0.06
	2	18.6	0.08
	3	22.8	0.17
	average	20.0	0.11
0.65	1	17.6	0.07
	2	23.4	0.12
	3	23.5	0.13
	average	21.5	0.11
0.375	1	19.1	0.01
	2	19.4	0.02
	3	19.4	0.002
	average	19.3	0.01
0.225	1	19.3	0.003
	2	19.2	0.006
	3	19.0	0.002
	average	19.2	0.004

Water/Methanol; $\bar{q}=12$; $M_{\alpha}=3$; $x/d=24$, $z/d=12$

TABLE 6
TIME HISTORIES OF SMD FOR WATER/ALCOHOL JET
IN SUPERSONIC FLOW

Exposure Time(msec)	x/d, z/d	\bar{q}	Time History of SMD (microns)
0.225	20, 6	3	18.6, 18.7/ 18.7, 18.6/ 19.2, 18.8
0.225	20, 6	12	20.9, 19.8/ 19.7, 19.2/ 19.3, 19.5
0.225	20, 10	12	18.9, 18.9/ 18.8, 19.1/ 18.8, 18.6
0.225	20, 12	12	19.9, 22.6/ 18.6, 19.1/ 18.8, 19.1
0.65	12, 6	18	16.0, 15.7/ 15.4, 15.4/ 15.5, 15.1/ 15.0, 14.9/ 26.0, 25.5/ 17.9, 16.4
2.5	12, 6	20	19.9, 17.7, 18.6/ 19.9, 18.9, 17.0/ 19.9, 21.2, 27.3
5.0	12, 6	10	19.9/ 19.9/ 19.9
25.0	12, 6	10	19.8/ 19.8/ 19.8/ 19.8/ 19.8/ 19.8

Water/Methanol; $M_\infty=3$

TABLE 7

MEAN AND STANDARD DEVIATION OF SMD FOR VARIOUS z/d

z/d	SMD (microns)	Standard Deviation of SMD
12	20	0.03
20	19	0.01
24	19	0.08

Water/Methanol; $\bar{q}=12$; $M_x=3$; $x/d=40$

TABLE 8

MEAN AND STANDARD DEVIATION OF SMD FOR VARIOUS x/d
FOR HIGH q WATER/ALCOHOL JET

x/d	SMD (microns)	Standard Deviation of SMD
12	19	0.01
30	18	0.03
40	20	0.03
60	19	0.02
80	19	0.01

Water/Methanol; $\bar{q}=12$; $M_{\infty}=3$; $z/d=10$

TABLE 9

MEAN AND STANDARD DEVIATION OF SMD FOR VARIOUS x/d
FOR LOW q WATER/ALCOHOL JET

x/d	SMD (microns)	Standard Deviation of SMD
24	20	0.04
30	17	0.02
40	19	0.01
60	19	0.02

Water/Methanol; $\bar{q}=4$; $M_x=3$; $z/d \leq 10$

TABLE 10

TIME HISTORIES OF SMD FOR HIGH \bar{q} WATER JET
IN SUPERSONIC FLOW

Exposure Time(msec)	x/d, z/d	Time History of SMD (microns)
0.11	10, 6	16.9, 16.0/ 23.4, 21.9/ 24.7, 23.1/ 18.7, 20.4/ 17.4, 17.9/ 18.8, 22.8
0.11	20, 8	17.6/ 18.5/ 14.6/ 14.4/ 20.1/ 16.1
0.11	20, 14	21.0, 18.3/ 19.2, 15.5/ 18.5, 22.6/ 26.4, 19.6/ 33.7, 19.3/ 17.2, 19.9
0.11	30, 14	18.5, 18.3/ 17.2, 15.7/ 16.7, 17.0
0.11	40, 10	19.9, 18.5/ 20.3, 27.3/ 16.3, 23.3
0.11	50, 10	23.6, 16.9/ 25.9, 22.9/ 21.3, 17.9/ 23.6, 17.9/ 24.7, 27.7/ 30.2, 25.5
0.11	100, 16	15.6, 18.1/ 16.1, 21.8/ 23.8, 20.1/ 22.1, 16.6/ 18.8, 30.8/ 24.7, 24.9
0.35	20, 14	17.6, 18.7, 17.6/ 18.5, 20.2, 17.6/ 19.5, 18.9, 23.2
0.35	30, 14	18.6, 16.7, 25.2/ 16.7, 17.0, 27.3/ 15.6, 16.5, 21.0
2.7	10, 6	17.8, 17.5, 20.9/ 18.5, 21.8, 19.9/ 18.5, 26.2, 22.4
2.7	20, 8	15.9, 19.6, 15.5/ 17.8, 15.3, 19.6/ 20.0, 14.0, 21.0
2.7	40, 10	15.1, 16.7, 20.2/ 16.8, 27.8, 27.3/ 20.5, 26.9, 27.1

(continued)

(continued)

TABLE 10

Exposure Time(msec)	x/d, z/d	Time History of SMD (microns)
2.7	60, 16	18.2, 19.1, 22.7/ 22.2, 25.9, 18.3/ 25.5, 25.4, 17.0
25.0	20, 16	19.3/ 18.7/ 18.2
25.0	30, 16	19.7/ 18.9/ 19.8
25.0	50, 10	19.4/ 19.6/ 20.0
25.0	100, 20	19.2/ 20.5/ 19.9

Water; $\bar{q}=10$; $M_{\infty}=3$

TABLE 11

VARIATIONS IN THE POPULATIONS OF THE THREE MAJOR SIZE GROUPS

Exposure Time(msec)	x/d, z/d	Populations in		
		7-20	20-60	60-100 microns
0.11	20, 14	0.698	0.261	0.041
		0.299	0.676	0.025
0.11	30, 14	0.640	0.342	0.018
		0.186	0.729	0.085
0.11	40, 10	0.671	0.302	0.027
		0.550	0.409	0.041
0.11	50, 10	0.572	0.385	0.043
		0.256	0.700	0.044
0.11	60, 16	0.530	0.407	0.063
		0.482	0.447	0.071
0.11	100, 16	0.714	0.192	0.094
		0.420	0.518	0.062
0.35	100, 26	0.424	0.541	0.035
		0.134	0.722	0.144
2.7	10, 6	0.520	0.432	0.048
		0.206	0.736	0.059
2.7	20, 8	0.821	0.167	0.012
		0.439	0.506	0.055
2.7	30, 10	0.356	0.605	0.039
		0.297	0.628	0.075
2.7	40, 10	0.695	0.259	0.046
		0.188	0.677	0.135
2.7	60, 16	0.622	0.312	0.066
		0.295	0.632	0.073
2.7	100, 10	0.335	0.630	0.035
		0.151	0.764	0.085

(continued)

(continued)

TABLE 11

Exposure Time(msec)	x/d, z/d	Populations in		
		7-20	20-60	60-100 microns
25.0	20, 10	0.336	0.627	0.037
25.0	30, 16	0.347	0.612	0.041
25.0	50, 10	0.324	0.637	0.039

Water; $\bar{q}=10$; $M_{\alpha}=3$

TABLE 12

VERTICAL LOCATIONS OF HIGHEST FREQUENCY TRANSIENTS

x/d	z/d	h/d	y/h	Highest Observed Frequency (kHz)
10	15	20	0.75	15
20	18	24	0.83	16
40	20	27	0.74	10
100	40	46	0.87	9

Water; $\bar{q}=10$; $M_\infty=3$

TABLE 13

VERTICAL LOCATION OF MAXIMUM VARIATIONS IN SMD

x/d	z/d	h/d	y/h	Maximum Value of the Standard Deviation of SMD
10	10	20	0.50	0.14
20	8	24	0.33	0.15
30	14	26	0.54	0.22
100	16	46	0.35	0.22

Water; $\bar{q}=10$; $M_x=3$

TABLE 14
MEAN TRANSMISSION VALUES

x/d	z/d	Rms Transmission As % of Laser Intensity
5	5	11%
10	15	15%
20	10	26%
20	18	52%
30	10	49%
40	5	71%
40	10	71%
40	20	59%
40	24	92%
40	26	100%
40	28	98%
100	10	74%
100	20	86%
100	30	90%
100	40	99%
100	50	100%

Water; $\bar{q}=10$; $M_{\infty}=3$

TABLE 15
 PLUME DIMENSIONS OF HIGH \bar{q} WATER JET
 IN SUPERSONIC FLOW

x/d	H/d	w/d	wC/d	LL/d	Lw/d
10	20	18	12	2	26
30	26	25	14	2	38
60	28	24	16	2	39
100	46	54	30	3	106
200	86	76	31	8*	80

* Refers to upper half of liquid layer

Water; $\bar{q}=10$; $M_\infty=3.0$

TABLE 16

TIME HISTORIES OF SMD FOR LOW \bar{q} WATER JET
IN SUPERSONIC FLOW

Exposure Time(msec)	x/d, z/d	Time History of SMD (microns)
0.11	10, 6	16.8, 19.2/ 18.6, 18.4/ 18.2, 18.6
0.11	20, 6	22.2, 21.1/ 15.4, 16.5/ 18.7, 18.1
0.11	30, 6	17.0, 17.7/ 19.0, 17.9/ 17.3, 17.3
0.11	50, 8	17.3, 16.7/ 18.5, 18.4/ 18.6, 18.7
0.35	10, 6	15.9, 22.2/ 16.1, 18.4/ 24.8, 26.5
0.35	20, 6	23.0, 21.8/ 23.6, 23.6/ 25.2, 15.0
0.35	30, 6	14.8, 14.8/ 22.4, 23.1/ 16.0, 17.4
2.1	20, 6	17.2, 17.0, 18.5/ 19.3, 17.7, 18.9/ 21.7, 16.2, 17.4
2.1	20, 10	19.3, 19.6, 19.1/ 19.9, 19.1, 19.8/ 19.9, 19.3, 18.9
2.1	50, 8	27.2, 25.5/ 17.6, 26.7/ 25.2, 29.8/ 24.5, 19.0/ 18.8, 19.3/ 19.1, 19.3
2.1	100, 10	15.8, 22.8/ 27.0, 17.5/ 27.0, 22.7
25.0	10, 6	19.6/ 25.4/ 22.7
25.0	30, 6	21.7/ 17.7/ 16.4
25.0	50, 8	24.3/ 21.0/ 26.4

Water; $\bar{q}=4$; $M=3$

TABLE 17

MAXIMUM AND MINIMUM SMD AT VARIOUS x/d

x/d	Minimum SMD (microns)	Maximum SMD (microns)
10	17	22
30	17	23
40	16	19.5
50	16.5	17.5
60	16	17.5

Water; $\bar{q}=4$; $M_x=3$; 0.11 msec Exposure Time

TABLE 18

VARIATIONS IN THE POPULATION OF THE THREE MAJOR SIZE GROUPS

Exposure Time(msec)	x/d, z/d	Populations in		
		7-20	20-60	60-100 microns
0.35	10, 6	0.656	0.322	0.022
		0.127	0.818	0.055
0.35	20, 6	0.729	0.245	0.026
		0.244	0.720	0.036
0.35	30, 6	0.747	0.240	0.013
		0.198	0.757	0.045
0.35	40, 8	0.664	0.307	0.029
		0.546	0.408	0.046
2.1	20, 8	0.391	0.574	0.035
		0.326	0.631	0.043
2.1	40, 8	0.406	0.555	0.039
		0.259	0.680	0.061
2.1	50, 8	0.596	0.273	0.131
		0.181	0.568	0.251
2.1	100, 10	0.697	0.200	0.103
		0.170	0.741	0.089

Water; $\bar{q}=4$; $M_w=3$

TABLE 19
MEAN TRANSMISSION VALUES

x/d	z/d	Rms Transmission as % of Laser Intensity
10	5	15%
20	5	59%
20	9	62%
40	6	75%
40	10	68%
40	14	71%
40	18	94%
40	20	99%
50	6	61%
100	5	81%
100	10	86%
100	20	90%
100	22	98%
100	24	98%
100	34	100%

Water; $\bar{q}=4$; $M_\infty=3$

TABLE 20

VERTICAL LOCATIONS OF HIGHEST FREQUENCY TRANSIENTS

x/d	z/d	h/d	y/h	Highest Observed Frequency (kHz)
20	9	14	0.64	20
40	10	20	0.50	19
40	14	20	0.70	19
100	22	30	0.73	13

Water; $\bar{q}=4$; $M_{\infty}=3$

TABLE 21

VERTICAL LOCATIONS OF MAXIMUM VARIATIONS IN SMD

x/d	z/d	h/d	y/h	Maximum Value of the Standard Deviation of SMD
20	6	14	0.43	0.16
30	6	16	0.37	0.20
100	10	30	0.33	0.21

Water; $\bar{q}=4$; $M_{\infty}=3$

TABLE 22
 PLUME DIMENSIONS OF LOW \bar{q} WATER JET
 IN SUPERSONIC FLOW

x/d	H/d	W/d	WC/d	LL/d	LW/d
10	11	14	12	2	28
30	16	20	14	2	36
60	20	24	17	2-3	39
100	30	42	32	3-4	88
200	68	66	38	14*	122

* Refers to upper half of liquid layer

Water; $\bar{q}=4$; $M_\infty=3$

TABLE 23

FREQUENCIES OF JET COLUMN WAVES

Liquid	M_∞	D_j cm	N_w kHz	Eq. 1 kHz	Eq. 2 kHz	Eq. 3 kHz	U_1 cm/sec	\bar{q}	σ dyne/cm	μ poise	V_j cm/sec	ρ_l gm/cm ³	P_{∞} dyne/cm ²
Water ¹	2.4	0.079	92	42	114	106	16400	11	73.5	0.01	4450	1.00	345000
Water ¹	2.4	0.079	86	42	114	104	16400	9	73.5	0.01	4115	1.00	345000
Water ¹	2.4	0.079	86	42	114	97	16400	5	73.5	0.01	2926	1.00	345000
Water ¹	2.4	0.159	61	21	57	49	16400	4	73.5	0.01	2957	1.00	345000
Water ¹	2.4	0.159	56	21	57	46	16400	3	73.5	0.01	2134	1.00	345000
CS ₂ ¹	2.4	0.159	61	21	62	47	16400	4	32.9	0.004	2743	1.27	345000
Water ¹	4.0	0.159	65	17	46	53	13800	2	73.5	0.01	1829	1.00	966000
Water ²	3.0	0.096	78	31	84	82	14900	10	73.5	0.01	3900	1.00	414000
Water/Alc. ²	3.0	0.096	69	31	65	63	14900	10	33.5	0.01	3900	0.96	414000
Water/Gly. ²	3.0	0.096	46	31	39	36	14900	10	73.5	0.105	3900	1.15	414000
Water ⁴	0.48	0.091	61	33	90	52	15100	10	73.5	0.01	1907	1.00	135000
Water ³	3.0	0.096	23	31	84	77	14900	5	73.5	0.01	2800	1.00	414000
Water ³	3.0	0.096	72	31	84	82	14900	10	73.5	0.01	3900	1.00	414000
Water ³	3.0	0.096	127	31	84	87	14900	17	73.5	0.01	5100	1.00	414000
Water/Alc. ³	3.0	0.096	40	31	65	52	14900	1.5	33.5	0.01	1500	0.96	414000
Water/Alc. ³	3.0	0.096	61	31	65	59	14900	5	33.5	0.01	2800	0.96	414000
Water/Alc. ³	3.0	0.096	61	31	65	59	14900	5	33.5	0.01	2800	0.96	414000
Water/Alc. ³	3.0	0.096	93	31	65	63	14900	10	33.5	0.01	4000	0.96	414000
Water/Alc. ³	3.0	0.096	99	31	65	66	14900	16	33.5	0.01	5100	0.96	414000
Fluorinert ³	3.0	0.096	30	31	94	66	14900	5	15.0	0.015	2100	1.78	414000
Fluorinert ³	3.0	0.096	47	31	94	70	14900	10	15.0	0.015	2900	1.78	414000
Fluorinert ³	3.0	0.096	91	31	94	75	14900	17	15.0	0.015	3800	1.78	414000
Water/Gly. ³	3.0	0.096	79	31	28	21	14900	1.5	73.5	0.276	1400	1.18	414000
Water/Gly. ³	3.0	0.096	89	31	28	24	14900	5	73.5	0.276	2500	1.18	414000
Water/Gly. ³	3.0	0.096	138	31	28	26	14900	11	73.5	0.276	3700	1.18	414000
Water/Gly. ²	3.0	0.096	37	31	32	30	14900	10	73.5	0.184	3900	1.17	414000

Superscripts: 1) From Ref. 46
 2) From Ref. 48
 3) From Ref. 49
 4) From present study

Due to the scatter of data for frequencies calculated from Ref. 48-49, the data was averaged over a range of \bar{q} ; listed \bar{q} and jet velocity values are mean values

U was calculated from free stream Mach number and pressure values; U is the velocity following a normal shock and is meant to represent the velocity of air striking the initial jet column; for the subsonic case, $U = U_\infty$

Frequency data: N_w = experimental frequency as calculated from wave speed and wavelength measurements (Ref. 46, 48, and 49) or as measured from extinction traces (present study)

Eq. 1 : $N_w = 0.2 \cdot (U_1/d_j)$ Strouhal equation

Eq. 2 : $N_w = 0.028 \cdot (U_1/d_j)^{3/2} \sqrt{\frac{\rho_l}{\mu}}$ Eqn. 5.1
 Units of constant are (sec/cm)^{3/2}

Eq. 3 : $N_w = 0.00007 \cdot V_j^{1/2} \cdot (U_1/d_j) \cdot \sqrt{\frac{\rho_l}{\mu}} \cdot \frac{P_{\infty}}{\rho_l}$ Eq. 5.2
 Units of constant are (sec/cm)^{1/2}

TABLE 24
INITIAL WAVELENGTH OF JET COLUMN WAVES

Liquid	M_{js}	d_j cm	N_w kHz	V_j cm/sec	Initial λ cm	V_j/N_w cm
Water ¹	2.4	0.079	92	4450	0.038-0.076	0.048
Water ¹	2.4	0.079	86	4115	0.030-0.096	0.048
Water ¹	2.4	0.079	86	2926	0.038-0.051	0.034
Water ¹	2.4	0.159	61	2957	0.060-0.130	0.048
Water ¹	2.4	0.159	56	2134	0.130-0.190	0.038
CS ₂ ¹	2.4	0.159	61	2743	0.094	0.045
Water ¹	4.0	0.159	65	1829	0.025-0.041	0.028
Water ²	3.0	0.096	127	5100	<0.080	0.040
Water/Alc. ²	3.0	0.096	93	4000	<0.080	0.043
Fluorinert ²	3.0	0.096	30	2100	<0.170	0.070
Water/Gly. ²	3.0	0.096	138	3700	<0.110	0.027
Water ³	0.48	0.091	61	1907	0.030	0.031

Superscripts: 1) From Ref. 46.

2) From Ref. 49. Wavelengths tabulated above are not initial wavelengths, but were recorded at various distances along the jet column.

3) From present study. Initial wavelengths were measured from stop-action photographs.

TABLE 25
FRACTURE FREQUENCIES

Liquid	d_j cm	M	\bar{q}	N_F kHz	N_w kHz	V_w m/sec	V_j m/sec	$N_w V_j / N_F V_w$
Water ¹	0.079	2.4	10.7	5.2	92	220	44.2	3.6
Water ¹	0.159	4.0	1.2	6.5	41*	157	12.2	0.5
Water ¹	0.318	2.4	0.2	4.4	29*	220	6.1	0.2
Water ²	0.079	4.0	14.0	7	92	157	44.5	3.7
Water ³	0.051	3.0	4.0	1-2	74*	192	24.7	4.5-9
Water ³	0.051	3.0	10.0	4.0	78*	192	39.0	4.0
Water/Alc. ³	0.051	3.0	12.0	0.5-1	72*	192	39.0	14-29
Water/Gly. ⁴	0.318	2.1	4.9	0.9	25*	234	17.7	2.1-2.5 ⁶
Water ⁵	0.091	0.48	10.0	15	60	—	19.0	4.0

Superscripts: 1) From motion pictures taken by Kush and Schetz in Ref. 46. Runs #9, 16 and 13, respectively.

2) From Ref. 46, Fig. 29a.

3) From present study. Fracture frequencies from FFTs and other transient data; wave speeds were calculated.

4) From Ref. 34, $\mu=2.4$ cpoise.

5) From present study. Fracture and wave frequency data taken from data. The number in the last column was obtained from pattern in extinction data.

6) Second figure takes into account the viscous "slowing" of waves as estimated from data in Ref. 48.

7) Wave velocity at breakup was represented by the velocity at the sonic point on bow shock.

*) Frequency calculated using Eqn. 5.2. No experimental data available.

TABLE 26

SMD FOR VARIOUS JETS AND FREE STREAM MACH NUMBERS

Liquid	Mach Number	\bar{q}	D_j cm	SMD microns	D_{max} microns	We·Re	Eq 5.3 SMD microns	Eq 5.4 D_{max} microns	Eq 5.8 SMD microns
Water ¹	0.48	10	0.091	17-18	44	4.481E7	52(31)	122(67)	23(20)
Water ²	3.0	10- 12	0.045- 0.096	13-14	38	5.298E7- 2.4114E8	25-36	58-79	13
Water ²	3.0	4	0.045- 0.150	15-16	44	5.298E7- 5.8871E8	25-45	58-96	15
Water/Alc. ²	3.0	12	0.045- 0.096	10-12	32	1.116E8- 5.079E8	20-30	47-64	12
Water/Alc. ²	3.0	4	0.045- 0.150	14-18	45	1.116E8- 1.240E9	20-37	47-77	15
Water/Gly. ³	3.0	12	0.096	19-20	—	3.075E7	60	144	18
Fluorinert ³	3.0	4	0.096	7	—	1.402E9	23	48	6
Fluorinert ³	3.0	12	0.096	5	—	1.402E9	23	48	5
Water/Gly. ³	3.0	4	0.096	18-36	—	3.075E7	60	144	22

Subscripts: 1) From present study. For the calculated diameters contained within the parenthesis was obtained using V_{max} = double the free stream velocity.

2) From Ref. 48, 49 and present study. The SMD values come from all three studies; the D_{max} value comes from the present investigation.

3) From Ref. 48 and 49.

Note: Equations 5.3 and 5.4 were developed by Ingebo and Foster(23). Equation 5.8 was developed during the present investigation.

TABLE 27
PLUME DIMENSIONS FOR WATER JETS

Water Injection Into A Mach 3 Crossflow

\bar{q}	x/d	h/d	Eq 5.11 h/d	Eq 5.9 h/d	Eq 5.13 h/d
4	10	11	12	13	11
4	30	16	15	17	17
4	60	20	18	19	23
4	100	30	20	21	28
10	10	20	17	21	17
10	30	26	22	27	27
10	60	28	26	31	36
10	100	46	29	34	44

Water Injection Into A Mach 0.48 Crossflow at $\bar{q}=10$

x/d	h/d	Eq. 5.14
10	20	20
20	24	24
50	31	31
100	37	37

Notes: Equation 5.11 was developed in Ref. 37

Equation 5.9 was developed in Ref. 64 and has been multiplied by a compensation factor.

Equations 5.13 and 5.14 were developed during the present investigation

**The vita has been removed from
the scanned document**